

Optics at the Nanoscale: Light Emission in Plasmonic Nanocavities

Thesis by
Carrie Elizabeth Hofmann

In Partial Fulfillment of the Requirements
for the Degree of
Doctor of Philosophy



California Institute of Technology
Pasadena, California

2010

(Defended May 20, 2010)

© 2010

Carrie Elizabeth Hofmann

All Rights Reserved

For my parents, David and Judy Ross,
who taught me to embrace the pursuit of knowledge,
in memory of my grandmother, Patricia Ross,
whose laughter and smile have always been an inspiration,
and with love and gratitude to Doug
for his encouragement along the way.

Acknowledgements

The completion of this thesis would not have been possible without the assistance of a number of people. First and foremost, I'd like to thank my advisor, Professor Harry Atwater, for his support over the past six years. In choosing a graduate school and research group, I was interested in finding an advisor with exciting research and, more importantly, a genuine concern for and interest in his students. Harry has been an amazing mentor, constantly challenging me and simultaneously providing a nurturing environment to grow as a scientist. I will be forever grateful for what I have learned from him.

I have also been fortunate to have several additional mentors. Professor Albert Polman of the FOM Institute AMOLF hosted me as a visitor in his group twice, during the summers of 2005 and 2007. This collaboration has been very fruitful and is the basis of the cathodoluminescence work in Chapters 2 and 3. Albert has always provided excellent scientific insight, and I'm very thankful for the opportunity to work with his group. Professor Javier García de Abajo of the Institute of Optics, CSIC, has also been an invaluable resource. He is a wizard with electromagnetic theory, and I used his BEM code to perform calculations that are presented throughout this thesis. I am incredibly grateful for his advice. Dr. Henri Lezec was a visitor in the Atwater group during my first few years as a graduate student, and he was an excellent source of ideas. Henri was a master on the FIB, and he fabricated the structures presented in Chapter 3. A number of other Caltech faculty have been helpful during my graduate career. I would like to specifically thank my candidacy and thesis committee members, Professors Brent Fultz, Bill Johnson, and Axel Scherer. Their input helped me significantly in the early stages of my thesis research. My decision to pursue a graduate education was a result of a fabulous research experience at UF, and I would like to thank my undergraduate advisor Professor Kevin Jones for his guidance.

I have learned a ton from the graduate students and postdocs I've worked with while at Caltech. In particular, I'd like to acknowledge those who have joined me as

co-authors. I was fortunate to have Luke Sweatlock as an officemate, and he was an incredible teacher of EM theory when he saw me scratching my head in confusion. His work contributed to the theory presented in Chapter 3. In her two years as a postdoc in our group, Deirdre O’Carroll was an amazing help in the optics lab. She taught me everything I know about single nanostructure optical measurements such as those presented in Chapter 5, and was also a great sounding board for discussions about enhancing spontaneous emission, always with her great Irish wit. During my first trip to Amsterdam to work at AMOLF, I was introduced to CL by Timon van Wijngaarden. The results from experiments we performed together can be found in Chapter 2, and Ewold Verhagen performed some of the theoretical analysis. Ernst Jan Vesseur, also from AMOLF, performed CL measurements that are presented alongside my own in Chapter 3. I’m thankful for their contributions to this thesis, as well as for our insightful conversations at conferences over the years.

I’ve been honored to mentor two fantastic Caltech undergraduates. Stanley Burgos was a SURF student the summer of 2006, working incredibly independently on dispersion theory that became the source of his senior thesis. His work also laid the groundwork for fabrication techniques I continued after he joined the Atwater group as a graduate student. Anna Hiszpanski started as a SURF student in the summer of 2007, and continued research throughout the following two years. I was immediately impressed with her work ethic and attitude, and it was a pleasure to see her grow as a scientist. Her dedication produced the structures fabricated in Chapter 5.

The subset of students and postdocs in Harry’s group working on plasmonics have served as an excellent resource over the years. I’d like to specifically thank Jennifer Dionne (both roommate extraordinaire and plasmonics superstar), Eyal Feigenbaum (mode volume expert), Vivian Ferry (ladies’ night buddy and plasmon PV master), and Domenico Pacifici. Team spontaneous emission, formed at the 2009 Atwater group retreat, provided incredible insight into my own project. For this, I would like to thank Gerald Miller, Tim Taminiau, and Dennis Callahan. The group members working on Si nanowire growth both provided samples and trained me to grow my own. I’m amazed at what they have accomplished in pursuing Si nanowires for pho-

tovoltaics, and acknowledge Brendan Kayes, Mike Filler, Mike Kelzenberg, Morgan Putnam, Dan Turner-Evans, and Shannon Boettcher for their help. I've had a lot of assistance in the optics lab from Robb Walters with the PL setup and from Greg Kimball and Jim Fakonas with the lifetime system, and I'm very grateful for that. Several people have also worked with me on the Nanoprobe, and I thank Rene de Waele from AMOLF and Marine Leite for their patience with that system, and Eric Ostby for his assistance with fiber cleaving. I'm appreciative for help with the fabrication reported in Chapter 5 from Scherer group members David Henry, Mike Shearn, and Sameer Walavalkar. I also thank Professor Anna Fontcuberta i Morral and Carlo Colombo from EPFL for providing the GaAs nanowires included in Chapter 7.

My 244 officemates have been amazing in my time at Caltech. When I first joined the group, Julie Biteen, Christine Richardson, and Luke Sweatlock immediately made me feel welcome and were always available for a friendly chat or research advice. Kory Aydin (e-beaming buddy and powerpoint-drawing master), Ryan Briggs (hardest worker I know), and Imogen Pryce (fellow wine aficionado and early morning workout buddy) have made working on this thesis as enjoyable a process as possible, and I'm very thankful for their friendship and support.

I'd like to thank the other graduate students of the Atwater group for their support during my time at Caltech, including Melissa Archer, Jeff Bosco, Chris Chen, Naomi Coronel, Davis Darvish (always up for a good debate about SEC versus Pac10 football), Michael Deceglie, Matthew Dicken, Hal Emmer, Tao Feng, Seokmin Jeon (my 249 buddy), Emily Kosten, Krista Langeland (a great cat-sitter), Andrew Leenheer, Manav Malhotra, Keisuke Nakayama, Jennifer Ruglovsky, Katsu Tanabe, Emily Warmann (happy to drive you to the train station anyday!), and Samantha Wilson. The group postdocs have also been extremely helpful, and I would like to acknowledge Jonathan Grandidier, Sungjee Kim (quantum dot fab expert), Lise Lahourcade, Jeremy Munday, Young-Bae Park, and Adele Tamboli (always makes me laugh!).

A number of administrators have helped me over the past six years, including Pam Albertson, Lyra Haas, Irene Loera, Cierina Marks, Connie Rodriguez, Rosalie Rowe, Mary Sikora, and Eleonora Vorobieff. April Neidholdt was much more than

an assistant, she was the group “mom,” always lending an ear or offering advice, and most importantly a good laugh to cheer me up when I needed it most. The KNI and micro-nano lab staff have provided a lot of scientific support, including Nils Asplund, Bophan Chhim, Guy deRose, Carol Garland, Ali Ghaffari, and Melissa Melendes. I’m thankful for all of their support. I’d like to acknowledge funding sources that made my thesis research possible, including fellowship support from the National Science Foundation and the National Defense Science and Engineering Graduate Fellowship.

My first two years as a graduate student were dominated by coursework, and Mike Winterrose, Ken Diest, Jessie Rosenberg, Eve Stenson, and Glenn Garrett spent many late nights working through homework sets with me, with plenty of laughs along the way. “Girl time” with fellow graduate students Kakani Young and Emily McDowell was very important to me, and we always had a great time together. Outside of Caltech, I’d like to thank my church family for their encouragement and prayers during these last months, in particular my amazing couples’ small group and D-group girls.

Finally, and most importantly, I’d like to thank my family. Words cannot express my gratitude to them for their unconditional love and support. My parents, David and Judy, are both teachers and have encouraged my academic pursuits from day one. My sister and brother, Rachel and Joel, have always been there when I needed to talk. Here in California, I’m grateful to my in-laws Beth, Terry, Christy, Jen, and Nancy for all of the ways they have supported me over the past six years. Lastly, I’d like to thank my husband, Doug. Fate brought us to Caltech together, and our relationship blossomed over late nights of quantum homework and lab reports – I’m thankful to Caltech for their role in granting my ‘Mrs. degree.’ Doug, I’m so proud to be your wife, I love you, and I can’t wait to see what the future has in store. This thesis is dedicated, with love, to my family.

Carrie E. Hofmann

May 2010

Pasadena, CA

Abstract

Nanophotonics has greatly benefited from the unique ability of surface plasmons to confine optical modes to volumes well below the diffraction limit of light. Plasmonics is an emerging area of research that opens the path for controlling light–matter interactions on the subwavelength scale, enabling truly nanophotonic technologies that are unattainable with conventional diffraction-limited optical components. Novel surface plasmon devices exploit electromagnetic waves confined to the interface between a metal and a dielectric, and permit the researcher to shrink light to dimensions previously inaccessible with optics. The extremely high and localized fields in plasmonic nanocavities are finding applications in research areas such as single-molecule sensing, nano-lasers, and photothermal tumor ablation, among others.

This thesis explores, both experimentally and theoretically, light emission in a number of plasmonic nanostructures. We present cathodoluminescence imaging spectroscopy as a new method of characterizing surface plasmons on metal films and localized in nanocavity resonators, with experimental observations supported by analytical calculations and electromagnetic simulation. This technique enables extremely localized surface plasmon excitation, a feature we exploit in both planar metal geometries and plasmonic nanocavities. We also study a specific nanocavity geometry, the plasmonic core-shell nanowire resonator, investigating both passive and active semiconductor core materials. This geometry allows precise control of the local density of optical states (LDOS), exhibiting the highest LDOS and smallest mode volumes in structures with dimensions as small as $\lambda/50$. Moreover, we discuss the Purcell effect as it applies to plasmonic nanocavities, and calculate enhancements in the radiative decay rate of more than $3000\times$ in the smallest structures. These results demonstrate the promise of plasmonics to enable truly nanophotonic technologies and to manipulate light at the nanoscale.

Contents

List of Figures	xii
List of Tables	xv
List of Publications	xvi
1 Introduction	1
1.1 Optics at the Nanoscale	1
1.2 What are Surface Plasmons?	2
1.3 Single-Interface Surface Plasmons	4
1.4 Exciting Surface Plasmons	9
1.5 Scope of This Thesis	11
2 Cathodoluminescence Imaging Spectroscopy: A Tool for Investigating Metallic Films and Nanostructures	14
2.1 Introduction	14
2.2 Cathodoluminescence Imaging Spectroscopy	15
2.3 Measuring SPP Propagation Length Near Resonance	16
2.3.1 Grating Fabrication	20
2.3.2 CL Measurements	20
2.3.3 Comparison with Theory	22
2.4 Investigating Semiconductor-Metal Nanostructures Using Cathodoluminescence	24
2.4.1 Sample Fabrication	24

2.4.2	CL Spectroscopy and Imaging	26
2.5	Chapter Summary	30
3	Plasmonic Modes of Annular Nanoresonators Imaged by Spectrally Resolved Cathodoluminescence	32
3.1	Applications of Annular Nanoresonators	32
3.2	Fabrication and Experiment Setup	33
3.3	Determining Modes of Annular Nanoresonators	36
3.3.1	Finite Difference Time Domain (FDTD)	36
3.3.2	Boundary Element Method (BEM)	39
3.3.3	Resonant Modes	39
3.4	Imaging Modes Using Cathodoluminescence	43
3.4.1	Panchromatic CL Imaging	43
3.4.2	Imaging Modes of an Ag Nanoresonator	43
3.4.3	Imaging Modes of an Au Nanoresonator	45
3.5	Chapter Summary	48
4	Ultra-small mode volume Si-Ag core-shell nanowire resonators	50
4.1	Introduction	50
4.2	Resonant Modes of Si-Ag Core-Shell Nanowire Resonators	51
4.2.1	The Boundary Element Method	53
4.2.2	Longitudinal Modes of Core-Shell Nanowire Resonators	54
4.3	A Case Study: 3 Resonators, 3 Size Regimes	57
4.4	Enhancing Radiative Decay	63
4.5	Core-Shell Nanowire Resonators as Sensors	67
4.6	Chapter Summary	70
5	Fabrication and Characterization of Si-Ag Core-Shell Nanowire Resonators	72
5.1	Introduction	72
5.2	Fabrication of Si-Ag Core-Shell Nanowires	72

5.2.1	Bottom-Up Approach	72
5.2.2	Top-Down Approach	77
5.3	Optical Characterization	81
5.3.1	Dark-Field Spectroscopy of Bottom-Up Fabricated Si-Ag Core-Shell Nanowires	82
5.3.2	Dark-Field Spectroscopy of Top-Down Fabricated Si-Ag Core-Shell Nanowires	83
5.4	Chapter Summary	87
6	Enhancing the Rate of Spontaneous Emission in Active Core-Shell Nanowire Resonators	88
6.1	Introduction	88
6.2	Theoretical Methods	89
6.3	Modes of Active Core-Shell Nanowire Resonators	91
6.3.1	GaAs-In _{0.51} Ga _{0.49} P-Ag Resonator	92
6.3.2	Al _{0.42} Ga _{0.58} As-Al _{0.70} Ga _{0.30} As-Ag Resonator	95
6.3.3	In _{0.15} Ga _{0.85} N-GaN-Ag Resonator	98
6.4	Enhanced Radiative Decay	101
6.5	Chapter Summary	103
7	Summary and Outlook	105
A	Boundary Element Method Calculations of LDOS and Decay Rates	110
A.1	Decay Rates in Atomic Units	110
A.2	Example BEM Input File	112
A.3	Example BEM Material Data File	114
B	Optical Characterization in the Nanoprobe	116
	Bibliography	117

List of Figures

1.1	Lycurgus cup and Rose Window	2
1.2	Surface plasmons in nanoparticles and on planar films	3
1.3	Single-interface SPP dispersion	7
1.4	Metal-insular-metal waveguide	9
1.5	Methods of exciting surface plasmons	10
2.1	Schematic of cathodoluminescence imaging spectroscopy	17
2.2	Schematic of CL excitation and outcoupling of SPPs on metal gratings	18
2.3	Calculated propagation lengths of SPPs	19
2.4	CL intensity decay from Ag and Au gratings at several wavelengths .	21
2.5	Propagation lengths on Ag and Au films measured with cathodolumi- nescence	23
2.6	Schematic and SEM of a ZnO nanowire sandwiched between Ag films	25
2.7	Monte Carlo simulation of electron trajectories in Ag/ZnO/Ag/Si . .	26
2.8	CL spectra of Ag-coated ZnO nanowires at several incident beam energies	27
2.9	CL imaging of an Ag-coated ZnO nanowire	29
3.1	Schematic of a sensing device consisting of an annular nanoresonator	34
3.2	Monte Carlo simulation of electron trajectories in a thick Ag film . .	35
3.3	Method of determining resonant modes with FDTD	37
3.4	Schematic of modes of annular nanoresonators	40
3.5	Simulated spectral response from FDTD	41
3.6	Simulated CL of an Ag nanoresonator calculated by BEM	42

3.7	Panchromatic CL imaging of Ag nanoresonators	44
3.8	Imaging modes in an Ag nanoresonator with cathodoluminescence . .	46
3.9	Comparing CL experiment and theory	47
3.10	CL Imaging of an Au nanoresonator	49
4.1	Si-Ag core-shell nanowire resonator schematic	52
4.2	Longitudinal modes of nanowire resonators	55
4.3	LDOS of Si-Ag core-shell nanoresonators as a function of core length and diameter	56
4.4	Modes of a Si-Ag core-shell nanowire resonator with $a = 50$ nm, $L =$ 500 nm, and $T = 100$ nm	58
4.5	Modes of a Si-Ag core-shell nanowire resonator with $a = 50$ nm, $L =$ 500 nm, and $T = 100$ nm	59
4.6	Modes of a Si-Ag core-shell nanowire resonator with $a = 25$ nm, $L =$ 150 nm, and $T = 100$ nm	61
4.7	LDOS and NF $ \mathbf{E} ^2$ cross sections for an Si-Ag resonator with $a =$ 25 nm and $L = 150$ nm	62
4.8	Modes of a Si-Ag core-shell nanowire resonator with $a = 5$ nm and $L = 25$ nm	64
4.9	Illustration of Purcell enhancement in a cavity resonator	66
4.10	Spontaneous emission enhancements and quantum efficiency in Si-Ag core-shell nanowire resonators	68
4.11	Si-Ag core-shell nanowire resonators as sensors	69
5.1	Si-Ag core-shell nanowire resonator schematic	73
5.2	Bottom-up fabrication procedure for Si-Ag core-shell nanowires . . .	74
5.3	Oxidizing and etching CVD-grown Si NWs to achieve desired diameter	75
5.4	SEM Micrographs of Ag-coated Si NWs	76
5.5	Top-down fabrication method for Si-Ag core-shell nanowire resonators	78
5.6	Si nanowires and Ag-coated Si nanowires fabricated by electron beam lithography, reactive ion etching, and Ag sputtering	79

5.7	SEM images of fully fabricated Si-Ag core-shell nanowire resonators .	80
5.8	Schematic of DF imaging and spectroscopy setup	81
5.9	SEM image of an Ag-coated Si NW and corresponding trenches used for normalization	82
5.10	Polarization dependent dark field scattering spectra from a FIB-cut Si-Ag NW	84
5.11	DF scattering image of Si-Ag core-shell NWs fabricated by EBL and RIE	85
5.12	DF scattering spectra of Si-Ag core-shell NWs fabricated by EBL and RIE	86
6.1	Schematic of an active plasmonic core-shell nanowire resonator	90
6.2	Modes of a GaAs-InGaP-Ag core-shell nanowire resonator	93
6.3	2D LDOS and NF $ \mathbf{E} ^2$ cross sections of a GaAs-InGaP-Ag core-shell nanowire resonator	94
6.4	Modes of an $\text{Al}_{0.42}\text{Ga}_{0.58}\text{As-Al}_{0.70}\text{Ga}_{0.30}\text{As}$ -Ag core-shell nanowire res- onator	96
6.5	2D LDOS and NF $ \mathbf{E} ^2$ cross sections of an $\text{Al}_{0.42}\text{Ga}_{0.58}\text{As-Al}_{0.70}\text{Ga}_{0.30}\text{As}$ - Ag core-shell nanowire resonator	97
6.6	Modes of an $\text{In}_{0.15}\text{Ga}_{0.85}\text{N-GaN}$ -Ag core-shell nanowire resonator . . .	99
6.7	2D LDOS and NF $ \mathbf{E} ^2$ cross sections of an $\text{In}_{0.15}\text{Ga}_{0.85}\text{N-GaN}$ -Ag core- shell nanowire resonator	100
6.8	Decay rate enhancement for III-V core-shell nanowire resonators . . .	102
6.9	Far-field radiation polarization for III-V core-shell nanowire resonators	103
7.1	Schematic of single nanostructure PL and lifetime decay experimental setup	107
7.2	PL intensity and decay-rate enhancements in GaAs NWs on Ag films	108
B.1	Omicron Nanoprobe stage	117
B.2	Fiber-based CL of YAG:Ce in the nanoprobe	118

List of Tables

4.1	Summary of Q/V and decay rate enhancements in Si-Ag core-shell nanowire resonators	71
6.1	Summary of Q/V and decay rate enhancements in III-V semiconductor plasmonic core-shell nanowire resonators	104

List of Publications

Portions of this thesis have been drawn from the following publications:

“Enhancing the rate of spontaneous emission in III-V semiconductor plasmonic core-shell nanowire resonators.” C. E. Hofmann, F. J. García de Abajo, and H. A. Atwater, submitted.

“Conjugated polymer/metal nanowire heterostructure plasmonic antennas.” D. M. O’Carroll, C. E. Hofmann, and H. A. Atwater, *Advanced Materials* **22**, 1223-1227 (2010).

“A plasmonic ‘bull’s-eye’ nanoresonator.” C. E. Hofmann and H. A. Atwater, *SPIE Newsroom* 1088-2008-03-04 (2008).

“Plasmonic modes of annular nanoresonators imaged by spectrally resolved cathodoluminescence.” C. E. Hofmann, E. J. R. Vesseur, L. A. Sweatlock, H. J. Lezec, F. J. García de Abajo, A. Polman, and H. A. Atwater, *Nano Letters* **7**, 3612-3617 (2007).

“Direct imaging of propagation and damping of near-resonance surface plasmon polaritons using cathodoluminescence spectroscopy.” J. T. van Wijngaarden, E. Verhagen, A. Polman, C. E. Ross, H. J. Lezec, and H. A. Atwater, *Applied Physics Letters* **88**, 221111 (2006).

Chapter 1

Introduction

1.1 Optics at the Nanoscale

The interaction of light with matter is one of the most significant processes on the planet, forming the basis of some of the most famous scientific discoveries to date. However, since its inception more than four hundred years ago, any advances in the field of optics have been limited by diffraction. This restricts the size of all optical components to dimensions greater than half the wavelength of light it supports [1]. It has only been in the past decade that researchers have finally developed a technology that beats the diffraction limit, instigating a revolution in optics. Plasmonics is an emerging area of research that opens the path for controlling light-matter interactions on the subwavelength scale, enabling truly nanophotonic technologies that are unattainable with conventional diffraction-limited optical components. Novel surface plasmon devices exploit electromagnetic waves confined to the interface between a metal and a dielectric and permit the researcher to “shrink” light to dimensions previously inaccessible with optics.

Although scientists take credit for revolutionizing this field fairly recently, in truth nanophotonics, and specifically plasmonics, has been in practical applications since the 4th century. Figure 1.1a shows a photograph of the Lycurgus cup from 4th century Rome, which consists of metallic nanoparticles suspended within a glass matrix. Because of plasmonic excitation of electrons in the metallic particles, the cup absorbs and scatters the short wavelengths of the visible spectrum, blue and green light. Therefore, when viewed in reflection, the plasmonic scattering gives the cup a greenish hue. If instead a white light source is placed within the goblet, the metal

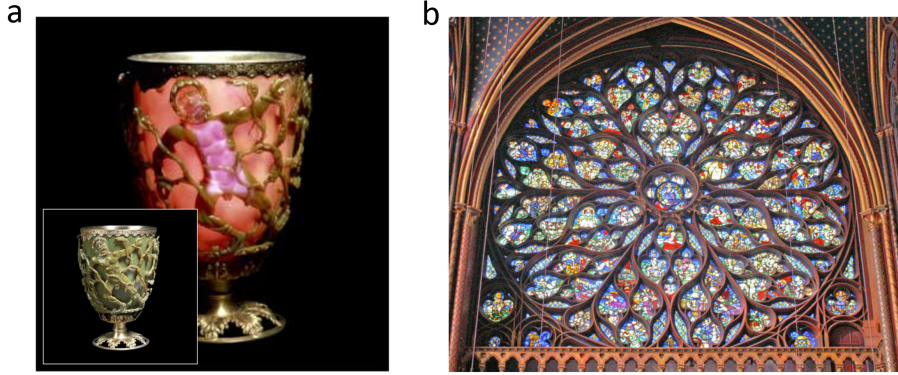


Figure 1.1. (a) The Lycurgus cup from 4th century Rome consists of small metal nanoparticles suspended within the glass matrix. Because of plasmonic excitation of electrons in the metallic particles, the plasmonic scattering in reflection gives the cup a greenish hue (inset). If a white light source is placed within the goblet, the glass appears red because it transmits only the longer wavelengths of the visible spectrum and absorbs the shorter ones (image from [2]). (b) The famous Rose window in Sainte Chapelle (12th century Paris) has its brilliant colors because of a similar phenomenon (image by B. Didier).

nanoparticles in the glass transmit the longer wavelengths of the visible spectrum and absorb the shorter ones, and the cup appears red. The brilliant colors in the famous stained-glass Rose window of Sainte Chapelle in 12th century Paris (Figure 1.1b) are created using this same technique, as the scattering and transmissive properties of metal nanoparticles are strongly shape and size dependent.

1.2 What are Surface Plasmons?

Surface plasmons are longitudinal charge-density fluctuations at the interface between a metal and a dielectric [3]. They resemble photons, but are nonradiative in nature and generally exhibit much shorter wavelengths than photons in free space. Surface plasmons essentially exist in two forms, as *localized* surface plasmons (SPs) and as

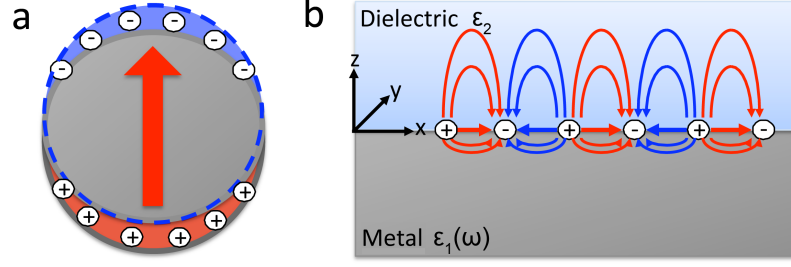


Figure 1.2. (a) Example of a particle plasmon. An incident electromagnetic field causes a disturbance of the electron cloud in the particle (negative charges), leaving behind a positively charged portion of the particle. The electron cloud then oscillates at the dipole plasmon resonance frequency. (b) Surface plasmons are also supported at the planar interface between a dielectric (ϵ_2) and a metal ($\epsilon_1(\omega)$). Here, an incident field excites a charge-compression wave that propagates along the metal/dielectric interface.

propagating surface plasmon polaritons (SPPs). An example of localized SPs are those supported by metal nanoparticles, illustrated schematically in Figure 1.2a. In this case, an incident electromagnetic field causes the electron cloud in the nanoparticle to oscillate coherently, resulting in positive and negative charge polarization. A restoring force arises from the Coulomb attraction between the displaced electrons and the positively charged nuclei, and the electron cloud oscillates at the dipolar plasmon resonance frequency [4]. These nanoparticles find applications in surface enhanced Raman spectroscopy [5, 6, 7], photothermal tumor ablation [8], and enhanced absorption in solar cells (see [9] and references therein), among others. In planar geometries, surface plasmons propagate as a longitudinal charge-compression wave at the interface of a metal and dielectric. As illustrated in Figure 1.2b, the field penetrates more significantly into the dielectric half-space than the metal, although both of these distances can be subwavelength.

1.3 Single-Interface Surface Plasmons

In this section, we will derive the single-interface surface plasmon dispersion relation [10]. We start with Maxwell's equations, which describe macroscopic electromagnetism:

$$\nabla \cdot \mathbf{D} = \rho_{\text{ext}} \quad (1.1a)$$

$$\nabla \cdot \mathbf{B} = 0 \quad (1.1b)$$

$$\nabla \times \mathbf{E} = -\frac{\partial \mathbf{B}}{\partial t} \quad (1.1c)$$

$$\nabla \times \mathbf{H} = \mathbf{J}_{\text{ext}} + \frac{\partial \mathbf{D}}{\partial t}. \quad (1.1d)$$

These equations relate the fields \mathbf{D} (dielectric displacement), \mathbf{E} (electric field), \mathbf{B} (magnetic induction), and \mathbf{H} (magnetic field) to ρ_{ext} (external charge density) and \mathbf{J}_{ext} (external current density). Limiting ourselves to isotropic, linear, nonmagnetic media, we also have

$$\mathbf{D} = \varepsilon_0 \varepsilon \mathbf{E} \quad (1.2a)$$

$$\mathbf{B} = \mu_0 \mu \mathbf{H}, \quad (1.2b)$$

where ε_0 and μ_0 are the electric permittivity and magnetic permeability, respectively, ε is the dielectric constant (relative permittivity), and $\mu = 1$ defines the relative permeability of nonmagnetic media.

Combining (1.1c) and (1.1d), we can derive the wave equation,

$$\nabla \times \nabla \times \mathbf{E} = -\mu_0 \frac{\partial^2 \mathbf{D}}{\partial t^2}, \quad (1.3)$$

the basis of electromagnetic wave theory. If we assume harmonic time dependence $\mathbf{E}(\mathbf{r}, t) = \mathbf{E}(\mathbf{r})e^{-i\omega t}$, (1.3) simplifies to its more familiar form as the Helmholtz equation,

$$\nabla^2 \mathbf{E} + k_0^2 \varepsilon \mathbf{E} = 0, \quad (1.4)$$

where $k_0 = \omega/c$ is the wave vector of the propagating wave in vacuum, ω is frequency, and c is the speed of light in vacuum.

To find a solution to the Helmholtz equation, we assume a one-dimensional geometry with propagation in the $+x$ direction along the interface $z = 0$, as seen in Figure 1.2b. Thus, the functional form of our solution is

$$\mathbf{E}(x, y, z, t) = \mathbf{E}(z)e^{i\beta x}e^{-i\omega t}, \quad (1.5)$$

where $\beta = k_x$ is the propagation constant. Plugging this into (1.4) gives the desired form of the wave equation,

$$\frac{\partial^2 \mathbf{E}(z)}{\partial z^2} + (k_0^2 \varepsilon - \beta^2) \mathbf{E} = 0, \quad (1.6)$$

with a similar expression for the magnetic field \mathbf{H} . To solve for the spatial field profile and dispersion relation of propagating waves, we seek specific expressions for \mathbf{E} and \mathbf{H} . These waves propagate at the interface between a conducting half-space ($z < 0$) with complex dielectric function $\varepsilon_1(\omega)$, and a non-absorbing half-space ($z > 0$) of dielectric material with real dielectric constant ε_2 (Figure 1.2b). For metals, this implies $\text{Re}[\varepsilon_1] < 0$, which is satisfied at frequencies below the plasma frequency ω_p . We also expect this propagating wave at the metal-dielectric interface to decay evanescently into both media.

Plugging (1.5) into Maxwell's equations, we find two sets of solutions with differing polarizations. The first are transverse magnetic (TM) solutions where the only non-zero field components are E_x , E_z , and H_y . In this case, we find for $z > 0$ (in the dielectric),

$$H_y(z) = A_2 e^{i\beta x} e^{-k_2 z} \quad (1.7a)$$

$$E_x(z) = iA_2 \frac{1}{\omega \varepsilon_0 \varepsilon_2} k_2 e^{i\beta x} e^{-k_2 z} \quad (1.7b)$$

$$E_z(z) = -A_1 \frac{\beta}{\omega \varepsilon_0 \varepsilon_2} e^{i\beta x} e^{-k_2 z} \quad (1.7c)$$

and for $z < 0$ (in the metal),

$$H_y(z) = A_1 e^{\imath\beta x} e^{k_1 z} \quad (1.8a)$$

$$E_x(z) = -\imath A_1 \frac{1}{\omega \varepsilon_0 \varepsilon_1} k_1 e^{\imath\beta x} e^{k_1 z} \quad (1.8b)$$

$$E_z(z) = -A_1 \frac{\beta}{\omega \varepsilon_0 \varepsilon_1} e^{\imath\beta x} e^{k_1 z}, \quad (1.8c)$$

where $k_i \equiv k_{z,i}$, is the z component of the wave vector in media $i = 1$ (metal) and $i = 2$ (dielectric). Applying boundary conditions requiring continuity of H_y and $\varepsilon_i E_z$ at the interface, we find that $A_1 = A_2$ and $k_2/k_1 = -\varepsilon_2/\varepsilon_1$. Also solving the wave equation for H_y gives

$$k_1^2 = \beta^2 - k_0^2 \varepsilon_1 \quad (1.9a)$$

$$k_2^2 = \beta^2 - k_0^2 \varepsilon_2. \quad (1.9b)$$

Finally, this gives us the dispersion relation:

$$\beta = k_0 \sqrt{\frac{\varepsilon_1 \varepsilon_2}{\varepsilon_1 + \varepsilon_2}}. \quad (1.10)$$

If we also seek transverse electric (TE) modes, where H_x , H_z , and E_y are the only non-zero field components, we find that no surface modes confined to the interface can exist with this polarization. Thus, SPPs only exist for TM polarization.

Reexamining the dispersion relation of (1.10), we see that there is a resonant condition when $\varepsilon_1(\omega) = -\varepsilon_2$, satisfied at the surface plasmon resonance,

$$\omega_{\text{sp}} = \frac{\omega_p}{\sqrt{1 + \varepsilon_2}}, \quad (1.11)$$

where ω_{sp} is the surface plasmon resonance frequency and ω_p is the bulk plasma frequency of the metal. The surface plasmon dispersion relation for Ag/air is plotted in Figure 1.3 as energy ($\hbar\omega$) versus k_x . The light line (LL) in air is plotted in gray ($E = \hbar\omega = \hbar ck_x$). For energies below the surface plasmon resonance, the

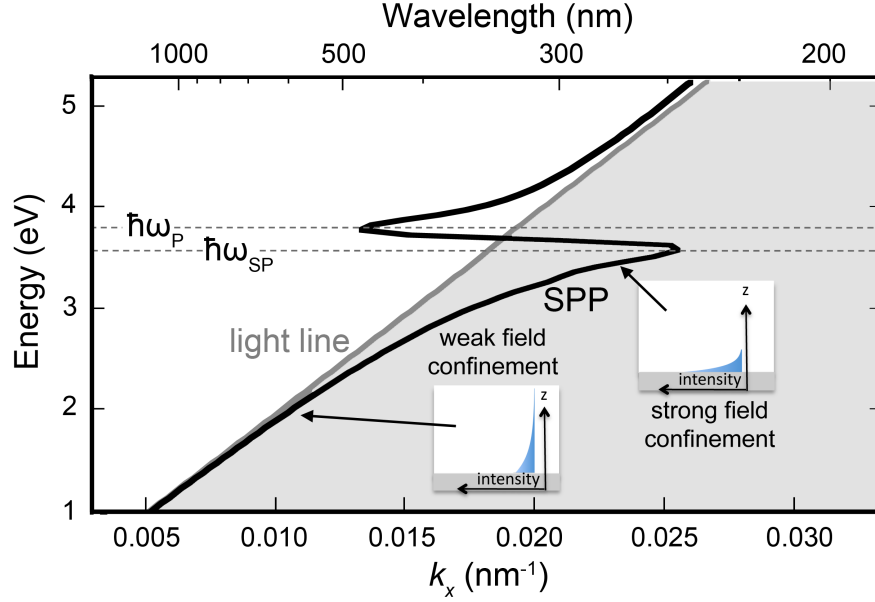


Figure 1.3. Dispersion relation for a single-interface (Ag/air) SPP, as in (1.10). The light line (LL) is plotted in gray, and the SPP dispersion in black. The light gray shaded region to the right of the LL indicates bound surface modes ($E < \hbar\omega_{sp}$), while the region to the left of the LL holds radiative modes ($E > \hbar\omega_p$). The inset images show that near the surface plasmon resonance ($\hbar\omega_{sp}$), fields are highly localized at the metal/dielectric interface in the z direction (strong field confinement). At lower energies when the SPP dispersion lies closer to the LL, fields penetrate more significantly into the dielectric environment (weak field confinement).

SPP dispersion lies to the right of the LL. Thus, at a given free-space energy, the SPP accesses larger k -vectors, or shorter wavelengths $\lambda = 2\pi/k_x$, than its free-space counterpart. This effect becomes more pronounced nearer to the surface plasmon resonance. Because of this so-called momentum mismatch, photons in free space cannot directly excite SPPs. Several strategies have been developed to overcome this, such as those mentioned in Section 1.4. Also shown in Figure 1.3 are schematics of the field penetration into the dielectric (air) for different regions of the dispersion diagram. At low energies when the SPP dispersion lies very close to the light line, there is weak field confinement in the z direction. Approaching resonance, the fields are more tightly confined to the Ag/air interface with higher field intensity as well.

Above the bulk plasma frequency ($E > \hbar\omega_p$), when the metal becomes transparent, modes are no longer bound to the interface and are instead radiative modes, and between the bulk plasma resonance and the surface plasmon resonance are the quasi-bound modes [11]. We can also calculate the propagation length of the SPPs along the metal/dielectric interface. The fields depend on x as $e^{i\beta x}$, so we define the propagation distance L_{SPP} as

$$L_{\text{SPP}} = \frac{2}{\text{Re}[i\beta]} = \frac{2}{\text{Im}[\beta]}. \quad (1.12)$$

If we consider a planar multilayer system consisting of not just a single metal-lodielectric interface, but two, we create the metal-insulator-metal (MIM) waveguide shown schematically in Figure 1.4. The MIM geometry more significantly confines the electromagnetic fields in the dielectric region than a single metallodielectric surface [12]. As illustrated in Figure 1.4, an Ag/SiO₂/Ag waveguide with SiO₂ thicknesses of 30 nm “shrinks” light that in free space has a wavelength $\lambda_{\text{air}} = 620$ nm down to a SP wavelength of $\lambda_{\text{sp}} = 200$ nm. Thinner insulator thicknesses allow accessing even larger k -vectors or shorter wavelengths, $\lambda_{\text{sp}} < \lambda_{\text{air}}/10$. This was experimentally demonstrated in an Au/SiO₂/Au geometry by Miyazaki and Kurokawa [13].

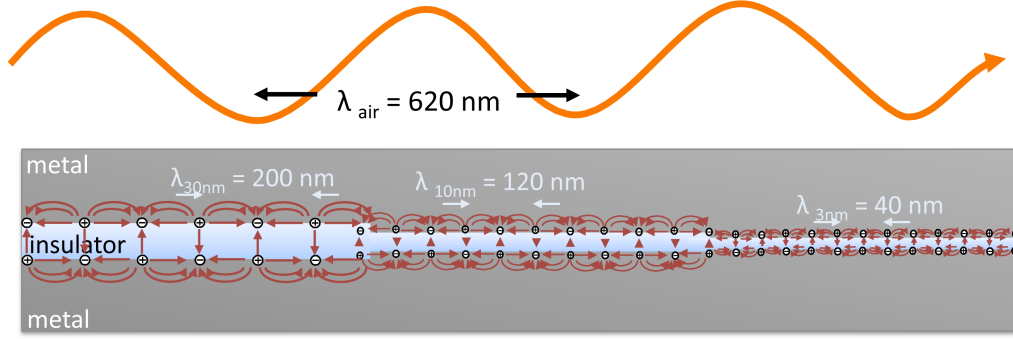


Figure 1.4. Top: a photon in free space at a wavelength of $\lambda_{\text{air}} = 620 \text{ nm}$, or an energy of 2 eV. Bottom: Inside a planar Ag-SiO₂-Ag metal-insulator-metal (MIM) waveguide, light of this same energy is sustained as surface plasmons with a much shorter wavelength λ_{sp} . For a 30 nm thick insulator, $\lambda_{\text{sp}} = 200 \text{ nm}$; 10 nm thick, $\lambda_{\text{sp}} = 120 \text{ nm}$; 3 nm thick, $\lambda_{\text{sp}} = 40 \text{ nm}$ —less than 1/10 of the free-space wavelength.

1.4 Exciting Surface Plasmons

As illustrated by the dispersion diagram in Figure 1.3, there is a mismatch in the momentum between the surface plasmon and free-space photons at a given energy. Because of this, clever strategies must be devised to efficiently excite SPs with light. A number of geometries have been developed to achieve this, several of which are shown in Figure 1.5. First, a grating can be defined in the metal film with a periodic spacing Λ that matches the appropriate in-plane momentum of the SP, $k_x = k \sin \theta$, as shown in Figure 1.5b [10]. In this case, phase-matching is satisfied when $\beta = k \sin \theta + 2\pi m / \Lambda$, where m is an integer. The reverse process can also take place: surface plasmons propagating along a metal/dielectric interface with a grating can radiate into free space.

More generally, any subwavelength scatterer on the metal film, such as random surface roughness with dimension a_i , can be used to somewhat less efficiently couple free-space photons at a number of different k -vectors (Figure 1.5c). In this case, the phase-matching condition is $\beta = k \sin \theta + \Delta k$, where $\Delta k = 2\pi m / a_i$. Again, roughness

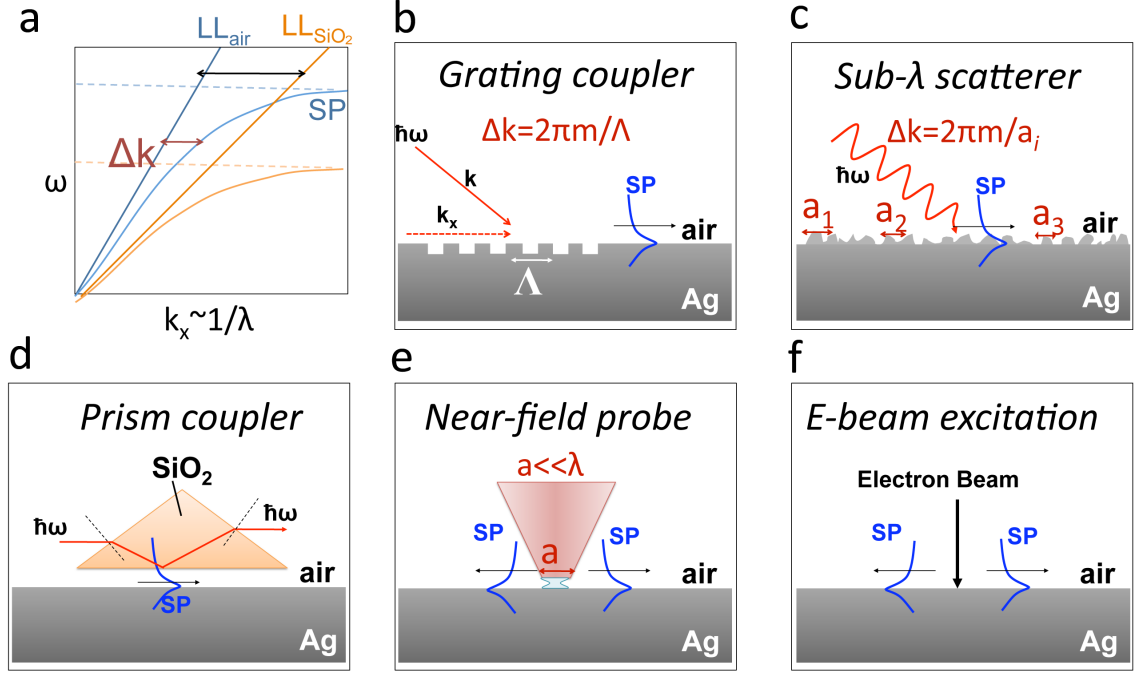


Figure 1.5. Methods of exciting surface plasmons at an Ag/air interface. (a) SP dispersion diagram (SP), showing the light line in air (LL_{air} , $\omega = ck$), the light line in SiO_2 (LL_{SiO_2} , $\omega = ck/n_{\text{SiO}_2}$), and the momentum mismatch Δk . A number of techniques have been developed to couple free-space photons into SPs at the Ag/air interface, such as (b) grating couplers, (c) subwavelength scatterers, (d) prism couplers, (e) near-field probes, and (f) electron-beam excitation. See text for details.

or designed localized scatterers can also be used to outcouple bound surface plasmons into free space.

Additionally, we can take advantage of total internal reflection inside a prism of refractive index n that differs from air, such as SiO_2 . As indicated in Figure 1.5a, the light inside the prism has a wavevector that overlaps with a portion of the Ag/air SP dispersion relation. As shown in Figure 1.5d, total internal reflection occurs at the prism/air interface, exciting surface plasmons by tunneling below to the Ag/air interface. This is known as the Otto configuration [14], and a similar geometry as the Kretschmann configuration [15].

A near-field probe with an aperture that is much much smaller than the wavelength of light can also be used to excite surface plasmons at much smaller length scales [16], as seen in Figure 1.5e. The subwavelength aperture $a \ll \lambda$ allows a number of wave vectors near the desired β , allowing phase-matched excitation of surface plasmons.

Alternatively, we desire methods of exciting surface plasmons that do not require incident photons. In Figure 1.5f, we consider a high-energy electron beam impinging on a metal surface that disturbs the equilibrium electron plasma in the metal, directly and locally exciting surface plasmons as the electrons at the surface of the metal oscillate (see [17] and references therein). This is the basis of cathodoluminescence spectroscopy as it applies to plasmonics, a technique utilized in Chapter 2 and Chapter 3 of this thesis.

1.5 Scope of This Thesis

This thesis is devoted to the investigation, both experimental and theoretical, of light emission in a number of plasmonic nanostructures. The first two chapters of this thesis present cathodoluminescence imaging spectroscopy as a new technique for characterizing surface plasmons on metal films and localized in nanocavity resonators, with experimental observations supported by analytical calculations and electromagnetic simulation.

In Chapter 2, we develop CL imaging spectroscopy as a tool for investigating

metallic films and nanostructures. This technique enables extremely localized surface plasmon excitation, a feature we exploit in both planar metal geometries and plasmonic nanocavities. We use CL to excite SPPs that propagate along an Ag or Au film, ultimately outcoupling via nanofabricated gratings, and from the emitted CL intensity determine the near-resonance SPP propagation distances. We also find good agreement between measured values and those expected from analytical calculations. Moreover, we demonstrate that CL can be used to excite localized SPs in a nanocavity geometry consisting of a semiconductor nanowire encapsulated in an Ag film. The incident electron beam excites both band-edge luminescence in the ZnO, as well as SP resonances of the Ag film.

We apply this same technique to excite and image modes in more complex resonator geometries in Chapter 3. The specific structure chosen is an annular nanoresonator, consisting of concentric grooves in a metal film that surround a flat plateau. Scanning the electron beam across the surface of the resonator yields cathodoluminescence emission that, when correlated with the excitation position, enables mapping the spatial variation of specific plasmonic modes. This analysis is performed in both Ag and Au resonators, and the experimental observations are supported by simulations of the electric field profiles of the modes, as well as calculations of the predicted CL emission.

The latter portion of this thesis is devoted to a specific plasmonic nanocavity geometry, the core-shell nanowire resonator. In Chapter 4, we embark on a theoretical investigation of the modes supported by the Si-Ag core-shell nanowire resonator. We find that this geometry sustains modes in structures with dimensions as small as $\lambda/50$. We also discuss the Purcell effect as it applies to plasmonic nanocavities, and demonstrate that the core-shell nanowire resonator can enhance the rate of spontaneous emission. Chapter 5 explains two routes to fabricating these structures, as well as methods we use to characterize their optical properties.

Chapter 6 considers active core-shell nanowire resonators that contain bright III-V semiconductor core materials. We design these structures such that the resonator mode dramatically enhances the rate of spontaneous emission at the emitting wave-

length of the active material, and calculate total decay rate enhancements above $8000\times$ the emission rate in free space. Furthermore, theory predicts that this geometry reorients the direction of far-field radiation, a feature crucial for designing on-chip, directional light-emitting diodes. Finally, Chapter 7 provides a thesis summary and outlook.

Chapter 2

Cathodoluminescence Imaging Spectroscopy: A Tool for Investigating Metallic Films and Nanostructures

2.1 Introduction

Understanding nanoscale optical phenomena is critical for the future miniaturization of photonic components. Traditional optical probes are limited in resolution by diffraction to dimensions greater than $\lambda/2$. This so-called diffraction limit has been pushed to tens of nanometers using near-field excitation or detection techniques. Unlike photons, electrons are not subject to the diffraction limit of light and can be focused to extremely small spot sizes (<5 nm in a scanning electron microscope, <1 Å in a transmission electron microscope). Thus, electron microscopes are the best tools for obtaining high spatial resolution in excitation. Furthermore, electrons can penetrate through optically thick layers, simultaneously providing information about surface and bulk optical properties [18, 19].

In this chapter, we will show that a combination of scanning electron microscopy (SEM) and cathodoluminescence (CL) imaging spectroscopy can be used to generate propagating surface plasmon polaritons (SPPs) and localized surface plasmons (SPs) on a nanometer scale. We use CL emission from planar metal films fabricated with gratings to determine the propagation distance of near-resonance SPPs. Also, semiconductor nanowires sandwiched between two metal layers illustrate that this technique can be used to excite and image localized surface plasmon resonances.

2.2 Cathodoluminescence Imaging Spectroscopy

As we mentioned in Section 1.4, focused electron beam excitation can be used as a tool for investigating plasmonic structures with extremely high spatial resolution and without the requirement of generating and incoupling incident photons. In a transmission electron microscope (TEM), electron energy-loss spectroscopy (EELS) measures the energy loss of inelastically scattered electrons that penetrate through a thin sample, allowing identification of the plasmon resonance. This method has been used to map out SPP dispersion in thin metal films [20, 21] and to determine modes of a number of plasmonic nanostructures such as spheres [22], nanotriangles [23], and nanoholes [24], among others. While the spatial and energy resolution of this technique surpasses many other methods, EELS requires samples to be electron transparent, or to have thickness of <100 nm, impractical for a number of applications.

In contrast, cathodoluminescence spectroscopy measures the emitted *photons* that result from electron beam excitation. The high-energy electrons in a SEM or a TEM impinge on a sample, and the resulting light emission is collected by a mirror located above the sample and sent to detectors. In semiconductors, CL emission is dominated by electron-hole pair excitation and recombination [25]. When the incident beam is scanned across the sample and the resulting light emission is correlated with excitation position, the spatial position of microstructural defects can be determined [26]. We have chosen to use this technique to investigate plasmonic structures in a SEM, which eliminates the constraint on sample thickness. Previously, CL in a TEM was used to image dipole and quadrupole modes of metal nanoparticles [27] and nanoholes [28], and more recently in a SEM to map modes of nanowires [29] and annular nanoresonators [30], whispering-gallery modes in annular grooves [31], and SPP Fabry-Perot resonators [32].

To investigate metallic films and nanostructures using CL here, a 30 keV electron beam from a FEI XL-30 SFEG SEM with a beam diameter of approximately 5 nm irradiates the sample. This beam passes through an aperture in a paraboloidal mirror and scans across the surface of the sample. The outcoupled light is collected by

the mirror with an acceptance angle of $\pm 80^\circ$ from the surface normal, and through software is correlated with the excitation position. An aluminium waveguide attached to the mirror sends the collected light through a monochromator (set to a central wavelength) and into a photomultiplier tube (PMT) or charge-coupled device (CCD) detector. This is shown schematically in Figure 2.1a.

To measure SPP propagation distance, we excite SPPs at a well-known distance from a nanoscale grating in the metal film. The grating couples the SPPs to free-space photon modes detected in the far field, and the SPP damping is probed by varying the distance between excitation spot and grating (see schematic in Figure 2.2a and 2.2b). Experiments were performed on both Ag and Au films, at frequencies ranging from close to resonance to the near-infrared. The experimentally determined propagation lengths were compared with the values expected for perfectly smooth films, calculated using the optical constants measured on the samples under study.

To perform spectrally resolved CL imaging, such as the results presented in Section 2.4, the position of the scanning electron beam is correlated with the collected light emission. The result is a hyperspectral image of CL emission that varies spatially with excitation position and spectrally with wavelength. Slices in wavelength through this image reveal the regions of most efficient excitation and outcoupling of CL intensity. This, along with CL spectroscopy, is used to characterize Ag-coated ZnO nanowires.

2.3 Measuring SPP Propagation Length Near Resonance

As the dielectric constants of plasmonic metals are dispersive, the propagation length of SPPs is strongly frequency dependent, as seen in Figure 2.3 [11]. In the visible and near-infrared, propagation distances as long as 100 μm have been measured for Ag and Au films [33]. Near the surface plasmon resonance frequency, in the UV/visible for Ag and Au, the propagation lengths are much shorter, and it becomes increas-

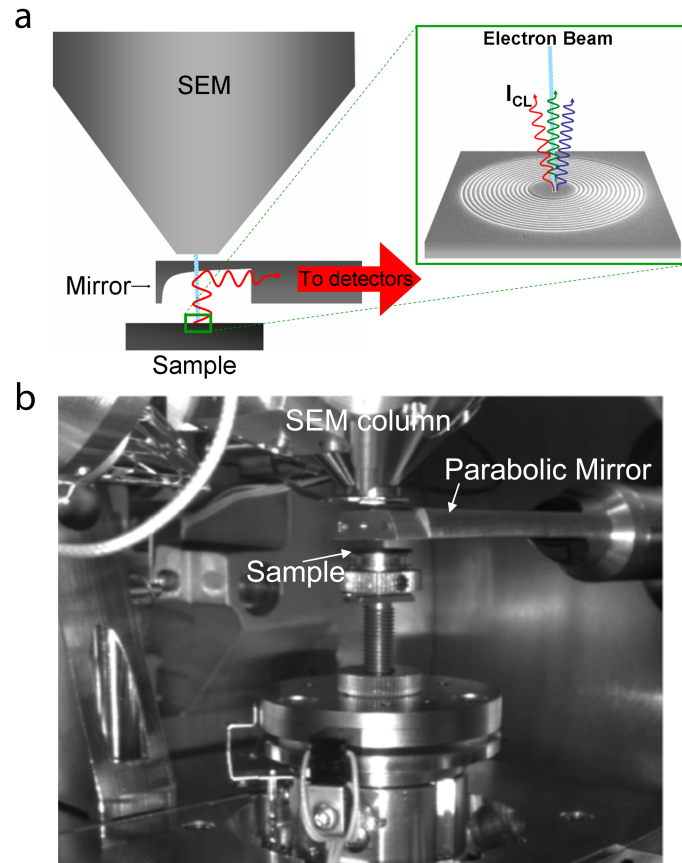


Figure 2.1. (a) Schematic illustration and (b) camera image of cathodoluminescence experimental setup. The electron beam passes through an aperture in a paraboloidal mirror and scans across the surface of the sample. The emitted light is captured by the paraboloidal mirror, sent through a lightguide and into detection optics (grating monochromator, PMT detector, and CCD detector).

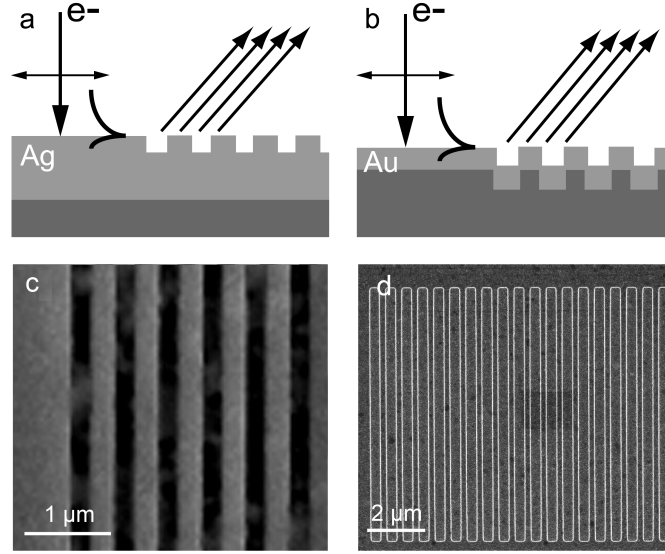


Figure 2.2. Schematic of excitation and outcoupling of surface plasmon polaritons on samples made by (a) FIB milling (Ag) and (b) electron beam lithography (Au). The electron beam is incident normal to the surface of the metal film with varying distance from the grating edge. Far-field radiation from the grating is then collected and analyzed. SEM images of the Ag and Au gratings are shown in (c) and (d), respectively.

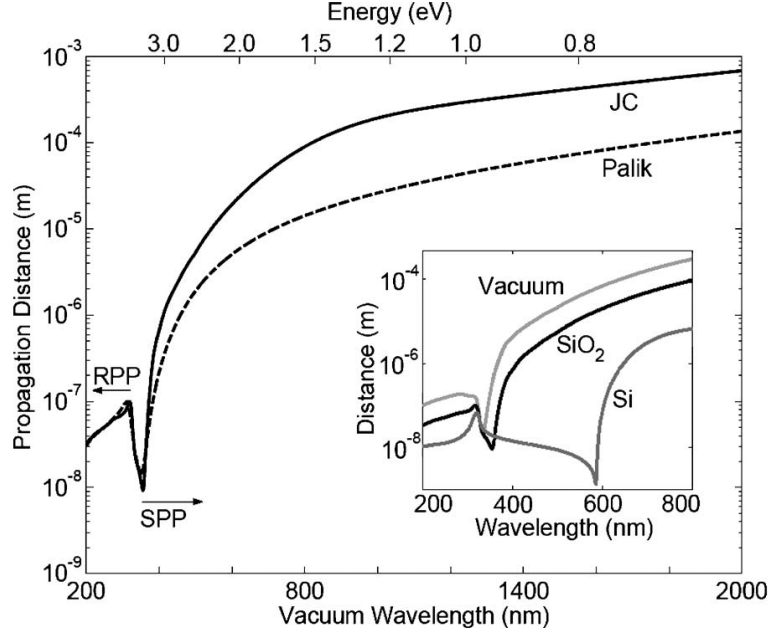


Figure 2.3. SPP propagation length for the Ag/SiO₂ geometry calculated using the optical constants of Johnson and Christy [34] (solid) and Palik [35, 36] (dotted). A vanishing propagation length occurs at the surface plasmon resonance, located at $\lambda = 355$ nm (358 nm) for Palik (JC). The local maximum at 320 nm coincides with the transition between quasi-bound (QB) and radiative (RPP) modes. Inset: Comparison of SP propagation for Ag/Air, Ag/SiO₂, and Ag/Si geometries plotted about the SP resonance. From [11].

ingly difficult to experimentally determine these distances with conventional optical techniques. Interestingly, it is this frequency range just below the surface plasmon resonance that holds the greatest potential for photonics because the wavelength of the SPPs in this region is much shorter than its free-space counterpart, the group velocity is reduced, and the electric fields are highly concentrated. The near-resonance SPPs therefore have the potential to enable the miniaturization of optoelectronic devices, to control the propagation of optical pulses, and to concentrate light in nanoscale volumes. In light of these applications, it is important to understand the propagation lengths of near-resonance SPPs.

2.3.1 Grating Fabrication

Ag and Au films patterned with gratings were fabricated by two different methods. First, a 400 nm thick Ag layer was evaporated onto a quartz substrate. With a focused ion beam (FIB) using a liquid Ga^+ source, gratings with 500 nm pitch and a depth of 50 nm were milled in the silver, as illustrated in Figure 2.2a. A second sample was fabricated using electron beam lithography (EBL) to pattern grating structures with a pitch of 500 nm in a poly(methyl methacrylate) (PMMA) layer, spun on a Si wafer. By developing the exposed PMMA and etching the Si in a SF_6 plasma, grating structures with an approximate depth of 70 nm were transferred to the Si substrate. An Au film with a thickness of 70 nm was then deposited on the Si by thermal evaporation, shown schematically in Figure 2.2b. Figures 2.2c and 2.2d show top-view SEM images of gratings fabricated with FIB milling and EBL, respectively.

2.3.2 CL Measurements

When focusing the electron beam at the edge of a grating, a broad spectrum was observed with a maximum in emitted CL intensity at the surface plasmon resonance. The monochromator was set to several wavelengths above this resonance to compare the CL emission intensity with varying beam position for different photon energies. CL intensity line profiles were either collected by the analysis of two-dimensional images, or using a single line scan.

Figure 2.4a shows the CL intensity collected from the Ag film as a function of distance between the exciting electron beam and the edge of the grating. Data was collected at wavelengths of $\lambda = 400, 500,$ and 600 nm. An exponential decay in intensity is observed as the electron beam moves away from the grating. This intensity decay is slower for longer wavelengths, implying longer SPP propagation lengths at longer wavelengths. CL intensity profiles were also collected on Au films, and are plotted in Figure 2.4b for $\lambda = 550$ and 600 nm. Signal-to-noise ratios proved to be smaller due to lower signal levels in this case, but similar intensity decays can be discerned at longer wavelengths than for Ag.

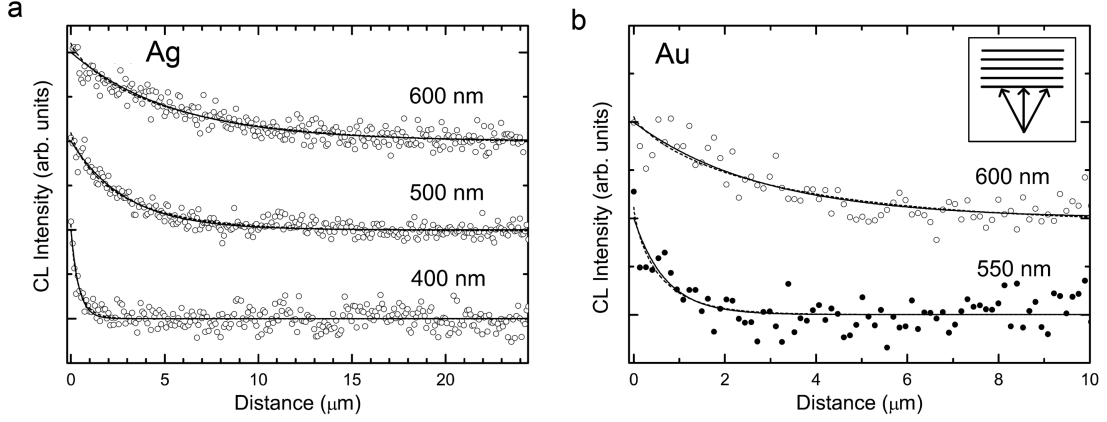


Figure 2.4. Cathodoluminescence intensity (open and closed circles) as a function of distance between the electron beam and grating edge for (a) an Ag film, with profiles collected at $\lambda=400$, 500, and 600 nm, and (b) an Au film, with profiles collected at $\lambda=550$ and 600 nm. A constant background is subtracted from all curves that are then normalized and shifted vertically along the CL intensity axis for clarity. Fits of (2.1) to the data using the angle-dependent grating coupling efficiencies $\alpha(\theta) = \delta(\theta)$ and $\alpha(\theta) = 1/\pi$ are shown as solid and dashed curves, respectively. The two models overlap in these plots in most cases. The inset in (b) schematically demonstrates that the electron beam acts as a point source of SPPs that propagate toward the grating over a broad angular range.

We note that all CL data curves exhibit a significant background intensity that is constant far away from the grating. This may be attributed to radiation from SPPs that couple out from random surface roughness. In order to compare the CL intensity decays for different wavelengths, normalized intensity is plotted in Figure 2.4 after the subtraction of these background values, determined using the fit procedure described below, and the curves are each shifted vertically for clarity.

2.3.3 Comparison with Theory

To correlate the CL intensity decays with the exponential decay of SPPs, we note that the electron beam generates SPPs in a point source. After excitation, the SPPs propagate over a large angular range toward the grating (see inset in Figure 2.4b). The measured CL intensity as a function of distance between the excitation spot and the grating edge x is therefore described by

$$I(x) = I_b + I_0 \int_{-\pi/2}^{\pi/2} \alpha(\theta) e^{\frac{-x}{L_{\text{SPP}} \cos \theta}} d\theta, \quad (2.1)$$

where I_b is the background intensity, I_0 is the SPP intensity scattered at the grating edge, L_{SPP} is the SPP propagation length, and $\alpha(\theta)$ is the angle-dependent grating coupling efficiency. The latter is unknown, but assuming that it is a monotonically decreasing function of θ , we can obtain upper and lower estimated limits to L_{SPP} from the measured CL intensity profiles using $\alpha(\theta) = 1/\pi$ and $\alpha(\theta) = \delta(\theta)$, respectively, where δ denotes the Dirac delta function. Both models were fitted to the CL data using nonlinear regression, yielding estimations of L_{SPP} and the background intensity I_b . The latter amounted to typically one to three times I_0 . The fits to the data displayed in Figure 2.4 are plotted through the data as solid and dashed curves for $\alpha(\theta) = \delta(\theta)$ and $\alpha(\theta) = 1/\pi$, respectively.

Measurements were also performed at other wavelengths, and the fitted upper and lower bounds to L_{SPP} are shown versus collection wavelength in Figure 2.5. For both Ag (closed symbols) and Au (open symbols), a clear increasing trend is observed as the wavelength increases above resonance. Figure 2.5 also shows the calculated

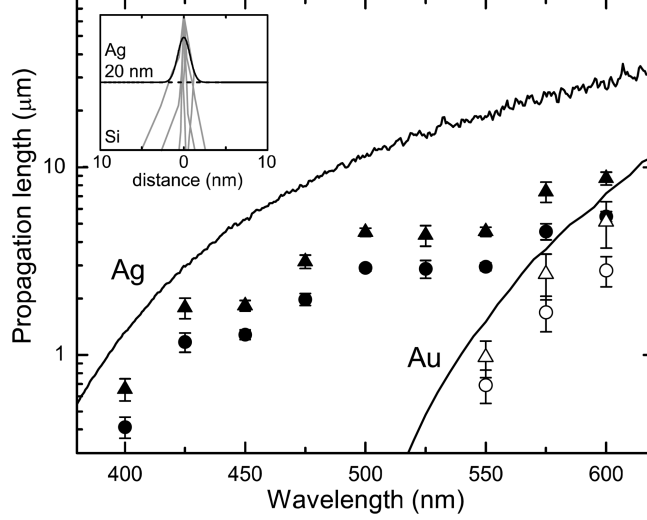


Figure 2.5. SPP propagation lengths L_{SPP} fitted from CL intensity data as in Figure 2.4 versus wavelength for Ag (closed symbols) and Au (open symbols). The values obtained using $\alpha(\theta) = 1/\pi$ are represented by triangles, and those using $\alpha(\theta) = \delta(\theta)$ by circles. The solid lines are the calculation of SPP propagation lengths for Ag and Au using experimental data for the dielectric constant considering bulk absorption in the film and leakage radiation. The inset shows several 30 keV electron trajectories in a plane at a depth of 20 nm.

propagation lengths as a function of wavelength on perfectly smooth films. For the optically thick Ag film, this value is obtained by considering only bulk absorption losses [3]:

$$L_{\text{SPP}} = (2k_x'')^{-1} = \frac{c}{2\omega} \left[\text{Im} \left(\frac{\varepsilon_m}{1 + \varepsilon_m} \right) \right], \quad (2.2)$$

where k_x'' is the imaginary part of the SPP wavevector, ε_m is the complex dielectric function of the metal, c is the speed of light in vacuum, and w is the frequency.

For the 70 nm Au film, in addition to absorption losses, the SPPs propagating at the vacuum/metal interface lose energy due to leakage radiation into the Si substrate. The propagation length including this radiation loss was obtained from the imaginary part of the SPP wave vector calculated by solving the dispersion relation for the vacuum/Au/Si system [37]. For both samples, the propagation lengths are calculated

using experimental values for ε_m determined from ellipsometry measurements on the metal films used. The surface plasmon resonance wavelengths predicted from these complex dielectric constants are 340 nm for silver and 540 nm for gold.

Irrespective of the functional form of $\alpha(\theta)$, a difference between measured and calculated dampings is observed that may be due to several additional loss processes. One of them is surface roughness of the films [38], which causes in-plane scattering of SPPs and coupling of SPPs to far-field radiation [39]. Additionally, grain boundaries and surface impurities could have a detrimental effect on SPP propagation. The fact that the observed propagation lengths on the Ag sample appear to deviate further from the calculated values than those on the Au sample could arise from differences in surface morphologies and impurities.

2.4 Investigating Semiconductor-Metal Nanostructures Using Cathodoluminescence

Cathodoluminescence imaging spectroscopy has been used for quite some time to correlate microstructural defects in semiconductors with light emission intensity [26]. In this section, we investigate an Ag-coated ZnO nanowire shown schematically in Figure 2.6 using CL. One of the benefits of CL spectroscopy over conventional optical techniques is that an electron beam can penetrate through an optically thick film. We take advantage of this feature here by exciting through the top Ag layer and into the ZnO nanowire, and observing the resulting luminescence.

2.4.1 Sample Fabrication

ZnO nanowires approximately 100 nm diameter and 10 μm tall are grown by chemical vapor deposition on a sapphire substrate using Au as the catalyst [40, 41]. After sonication in isopropyl alcohol (IPA), nanowires are dropcast onto a Si substrate coated with 100 nm Ag. A second Ag layer 100 nm thick is evaporated, with the longitudinal cross section shown schematically in Figure 2.6a. To create shorter nanowires, the

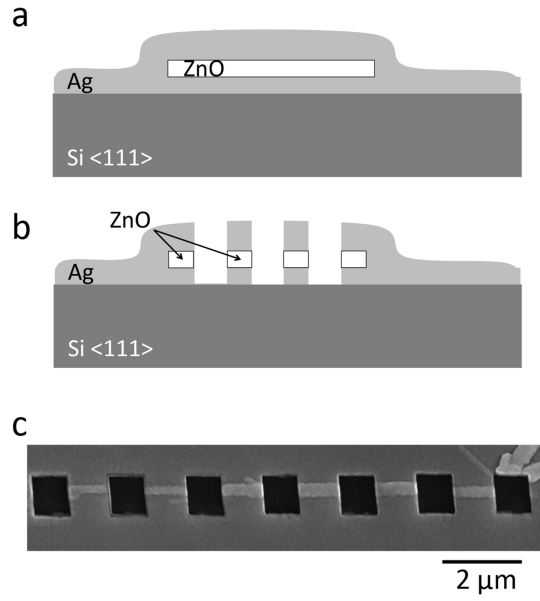


Figure 2.6. (a) Schematic cross section of a ZnO nanowire dropcast on an Ag film, and then overcoated with Ag. (b) Shorter resonators are created by cutting the wire into segments using a FIB. (c) Top-view SEM image of the Ag-coated ZnO nanowire after FIB cutting.

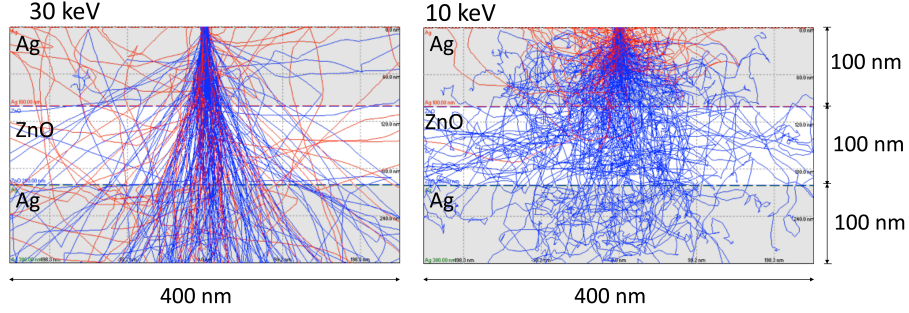


Figure 2.7. Monte Carlo simulation of electron trajectories [42] in a 4-layer system consisting of Ag/ZnO/Ag (each 100 nm thick) on Si for an incident electron beam with 5 nm diameter at (a) 10 keV and (b) 30 keV.

coated NW is cut with a FIB to segments approximately 1 μm long (Figures 2.6b and 2.6c). After measurements, an additional layer of 20 nm Cr is thermally evaporated over the sample to damp surface plasmons on the outer Ag/air interface, and CL measurements are repeated.

2.4.2 CL Spectroscopy and Imaging

Unlike for the grating structure studied in Section 2.3, the electron beam excitation conditions for the Ag-coated ZnO nanowires is optimized for maximum interaction volume in the semiconductor. As a result, the spatial resolution is degraded. This is illustrated in the Monte Carlo simulation of electron trajectories [42] in Figure 2.7. Here, we consider a 4-layer system of Ag/ZnO/Ag (each 100 nm thick) on a Si substrate. For excitation at 30 keV, the same condition used to investigate the metal gratings, the initial spotsize of 5 nm broadens to approximately 50 nm in the ZnO layer. If we instead consider a lower incident beam energy of 10 keV, the interaction volume is now confined mostly within the ZnO layer, although with a poorly defined spot size in the semiconductor of approximately 200 nm. This demonstrates that we can sacrifice spatial resolution in excitation to obtain more interaction of the incident electrons in the ZnO layer.

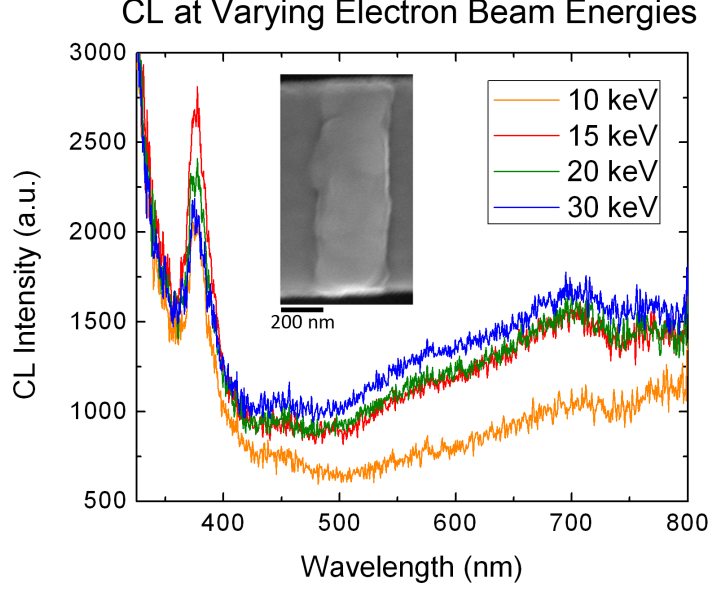


Figure 2.8. CL spectra of an Ag-coated ZnO nanowire for incident electron beam energies of 10, 15, 20, and 30 keV. Maximum emission intensity at the bandedge ($\lambda = 375$ nm) is seen for excitation at 15 keV. Inset: Top-view SEM image of the nanowire.

The excitation conditions are optimized for maximum CL intensity at the ZnO bandedge ($E_g = 3.3$ eV, or $\lambda = 375$ nm). CL spectra at incident beam energies of 10, 15, 20, and 30 keV are shown in Figure 2.8. These spectra are 20 s acquisitions with the CCD detector while the electron beam is scanned quickly over the area shown in the SEM inset. Brightest CL emission at the band-edge is seen for excitation at 15 keV. Other spectral features at shorter wavelengths are due to SPs outcoupling from the rough Ag film, and features at longer wavelengths are most likely due to cavity resonances inside the ZnO nanowire.

We also collect a series of images that map CL emission intensity spatially as a function of excitation position and spectrally versus wavelength. Figure 2.9a is an SEM image of an Ag-coated ZnO nanowire, showing the region scanned for the CL spectrum imaging. The CL images in Figure 2.9b are acquired by scanning the electron beam across the region in the SEM image to form an image of 80×26 pixels², with a per pixel dwell time of 1 s and spatial resolution of 15 nm/pixel. The CCD

acquires a spectrum at each pixel, and slices through this hyperspectral image reveal the images in Figure 2.9b at the indicated wavelengths ($\lambda = 350, 375, 500, 600$, and 700 nm), with a 20 nm spectral passband. This acquisition takes approximately 1 hr, during which time the program also corrects for spatial drift every 15 pixels. Bright yellow regions in the images correspond to positions where electron excitation results in bright CL emission. At $\lambda = 350$ nm, very near the SP resonance for Ag/air, bright emission occurs fairly uniformly for excitation along the wire. This is expected, as SPs excited near resonance will outcouple due to surface roughness after propagating only a very short distance.

At the ZnO bandedge ($\lambda = 375$ nm), bright emission is seen for excitation near the left end of the wire. Collection asymmetry by the mirror was eliminated as a contributing factor by rotating the sample 180° and seeing similar behavior. This asymmetry of emission from the ZnO could be due to several factors. Most likely, the FIB process resulted in the left end of the nanowire having less Ag coating, resulting in brighter emission. The emission at $\lambda = 500$ nm shows several peaks in intensity along the wire, which may be due to either a standing resonance of the ZnO core or of the outer Ag/air interface. Similar features are observed at $\lambda = 600$ nm. At $\lambda = 700$ nm, bright emission is only seen for excitation at the left end of the wire. Emission from ZnO in the band of $\lambda = 600\text{--}800$ nm can be attributed to defect luminescence.

After measurements were completed, the sample was coated with a 20 nm thick Cr layer to differentiate between emission from the outer Ag/air interface and modes of the ZnO nanowire. We then repeated CL measurements on the same nanowire. The resulting CL images are seen in Figure 2.9c. These images were acquired as 51×8 pixels² (spatial resolution 22 nm/pixel), with a 10 s dwell per pixel and no drift correction. Because the spatial area scanned was smaller than before coating with Cr, the unscanned area is shown in blue. Also, significant drift did occur during the collection that can be identified in the images.

As expected, at $\lambda = 350$ nm, near the SP resonance, emission from SPs at the Ag/air interface has been quenched. Band-edge emission at $\lambda = 375$ nm in the Cr-

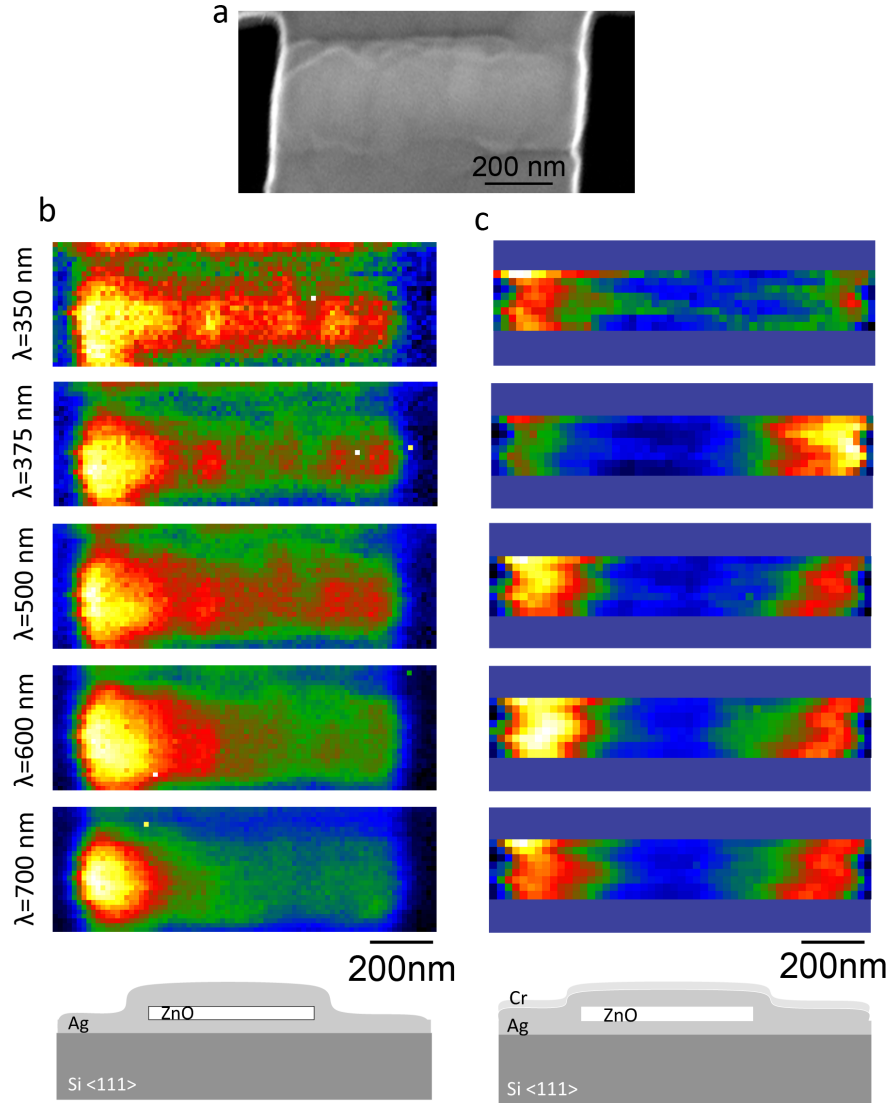


Figure 2.9. (a) SEM image of a FIB cut Ag-coated ZnO nanowire. (b) CL images at the indicated wavelengths of the nanowire shown in (a). (c) CL images at the indicated wavelengths of the nanowire coated with a thin layer of Cr, which damps SP propagation on the outer interface. Dark blue outline compensates for smaller scan region in Cr-coated images. In all images, yellow regions illustrate positions where electron beam excitation results in bright CL emission.

coated nanowire is now brightest for excitation at the right end of the nanowire. At the longer wavelengths ($\lambda = 500$ nm and $\lambda = 600$ nm), where previously bright regions were observed for excitation along the length of the wire, the Cr coating has also quenched this emission. Thus, we can conclude that the source of emission in the Ag-coated ZnO nanowire without Ag was due to a SP mode of the outer Ag/air interface, and not of the interior nanowire. Even in the Cr coated structure, emission in the defect luminescence band is concentrated at the left end of the nanowire.

2.5 Chapter Summary

These results show that CL imaging spectroscopy is a useful tool for high-resolution characterization of plasmonic nanostructures. It can be applied to study the propagation and damping in a wide array of geometries, including plasmonic waveguides, tapers and cavities. The ultimate resolution of this CL imaging technique is determined by the excitation volume in the metal film: thinner metal films will yield higher resolution. As an example, the inset in Figure 2.5 shows trajectories of 30 keV incident electrons on a 20 nm thick Ag film on Si calculated using a Monte Carlo simulation program [42]. It shows the angular spread of the electron beam in a 20 nm thick film is only a few nanometers, and thus in such a geometry the lateral resolution is mostly determined by the incident beam diameter. More detailed calculations of the generation of SPP surface waves by the electron cascade inside the film are required to study the ultimate resolution that can be achieved.

We have determined the propagation length of surface plasmons near the surface plasmon resonance for both Ag and Au films. Propagation lengths as short as several hundred nanometers are determined, and the propagation length increases as the wavelength is increased above resonance. Comparing these results with calculations accounting for loss due to absorption in the film and to leakage radiation shows that other loss mechanisms appear to have a large contribution as well.

We also investigated Ag-coated ZnO nanowires using this technique and demonstrated that electron beam excitation can be localized in depth to most efficiently

excite luminescence from the ZnO NW core. Spectrally resolved CL images demonstrate that surface plasmons on the outer Ag/air interface emit brightly near the SP resonance and form standing resonances at longer wavelengths. Coating the wire with a thin layer of Cr quenches this luminescence, but not the band-edge or defect-band luminescence from the ZnO core. The ultimate imaging resolution of this technique will be determined by the excitation volume of SPPs by electrons, which may enable the characterization of SPPs and localized modes in a large array of plasmonic nanostructures.

Chapter 3

Plasmonic Modes of Annular Nanoresonators Imaged by Spectrally Resolved Cathodoluminescence

3.1 Applications of Annular Nanoresonators

Excitation and localization of surface plasmon polariton (SPP) modes in metallodielectric structures is currently a topic of intensive research motivated by the ability to achieve truly nanophotonic materials and devices with tunable optical dispersion [43]. In particular, nanoresonators are essential building blocks of future subwavelength-scale photonic systems as both active [44] and passive [45] device components. Nanos-structures consisting of annular grooves and gratings in metal films exhibit exciting properties such as photon-to-plasmon coupling [46], focusing [47, 48, 49], and intensity enhancement [48, 49, 50]—all of which are exciting for sensing [51] and surface enhanced Raman scattering (SERS) applications [6, 52]. In this chapter, we directly excite plasmonic modes in engineered annular nanoresonators on Ag and Au surfaces with a highly localized electron beam source, and use spectrally resolved cathodoluminescence imaging [26] to probe the plasmon field intensity as a function of excitation position.

Surface plasmon polaritons are generally excited optically at a metal/dielectric interface using a prism or grating to couple the incident light to the surface wave [3]. Previously, annular gratings have been investigated with near-field optical techniques capable of 20 nm optical probe sizes [47, 49]. Alternatively, a focused electron beam

can be used to directly and locally excite SPPs with higher spatial resolution, without the intermediate step of generating and coupling an incident photon. Electron energy loss spectroscopy (EELS) in the transmission electron microscope (TEM) has been used to visualize plasmonic modes in metal nanoparticles, nanorods, and nanotriangles with spatial resolution limited only by the electron beam diameter, which can be as small as 1 nm [23, 27, 53, 54]. Such investigations in the TEM require samples to be electron transparent, e.g., to have thicknesses less than 100 nm. However, cathodoluminescence (CL) excitation in the scanning electron microscope (SEM) does not impose such a constraint on sample thickness. In the SEM, electron beam excitation yields CL emission which we used in Chapter 2 to investigate the propagation of SPPs along planar metal surfaces and linear gratings [55] (see also [56] and [29]). In this chapter, we extend this technique to investigate modes in nanofabricated plasmonic annular nanoresonators.

One possible application of an annular nanoresonator is illustrated schematically in Figure 3.1 as an electrically excited sensing platform for SERS. As the electron beam in an SEM acts as a prototypical means of electrically exciting surface plasmons, we imagine a chip-based sensing device that combines an electrical source of SPPs that propagate along the metal surface and are focused strongly using an annular nanoresonator. The enhanced local electric fields in the center of the resonator could significantly enhance the SERS signal, enabling a new sensor technology.

3.2 Fabrication and Experiment Setup

Nanoresonators were fabricated on Ag and Au surfaces. The Ag structures were prepared by evaporating 400 nm of Ag on a quartz substrate and using focused ion beam (FIB) nanofabrication with a Ga^+ ion source operating at 30 keV. Each annular resonator is composed of a center plateau and five concentric rings separated by grooves 50 nm deep, with varying grating ring period and center diameter. Nanoresonators with 15 concentric grooves 100 nm deep were also patterned in the (111) surface of a polished single crystal Au substrate grown by the Czochralski process.

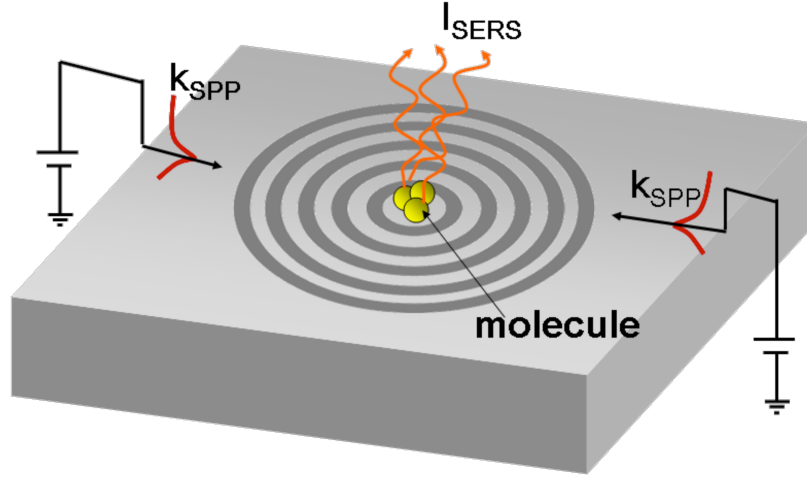


Figure 3.1. Schematic of a sensing device incorporating electrical excitation of surface plasmons that are focused to the center of an annular nanoresonator. Molecules located at the focal point will respond to the enhanced local fields, resulting in increased SERS intensity, I_{SERS} .

Spectrally resolved CL analysis was performed using a field emission SEM operating at 30 keV and equipped with a mirror-based cathodoluminescence detection system [26]. For this technique, the spatial resolution in excitation is limited only by the electron beam spot size of 5 nm. Monte Carlo simulations [42] of electron trajectories in a 400 nm thick Ag film on quartz are shown in Figure 3.2. As seen in the left image, although the electron trajectories extend entirely through the Ag film and beyond 4 μm into the SiO_2 substrate, any luminescence excited below several skin depths in the Ag film [11] is significantly attenuated before emission and detection are possible. Thus, any detected light arises only from interactions near the surface of the Ag film. Additionally, the enlargement of the interactions in the Ag film confirm that no significant beam broadening occurs within 20 nm of the Ag surface, one electric field skin depth. Therefore, this technique offers incredibly high spatial resolution in excitation.

When a metallic nanoresonator is excited with an electron beam, there are several phenomena that can result in light emission. High-energy electrons can directly

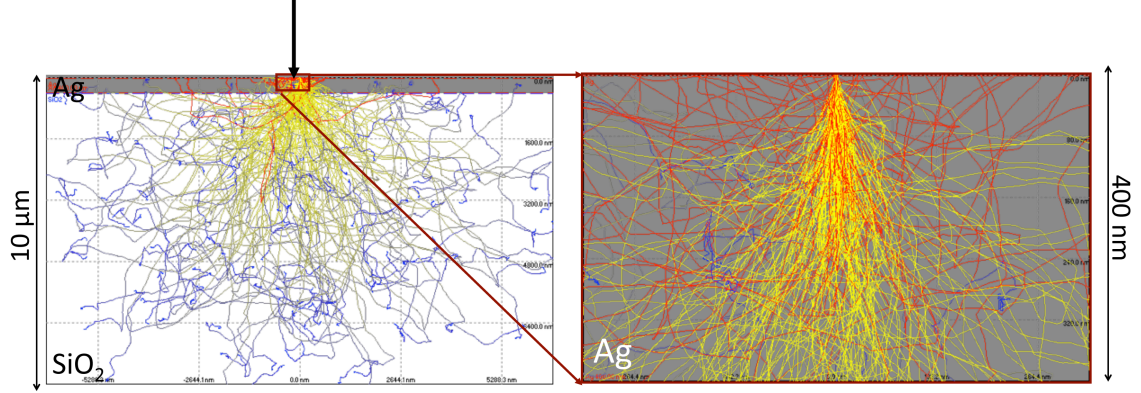


Figure 3.2. Left: Monte Carlo simulation [42] of 30 keV electron trajectories incident on a 400 nm thick Ag film on SiO₂. Right: Close-up of electron trajectories in Ag film, showing only slight beam broadening in the top 20 nm.

excite d-band transitions in the metal film, producing photons with energies of approximately 4 eV (310 nm) upon relaxation in Ag [57, 58]. The incident beam can also excite localized surface plasmons (SPs) and propagating SPPs. In the annular nanoresonator structures described here, the SPs can couple to resonant plasmonic modes. We show that such resonant modes are most efficiently excited by focusing the localized electron beam at positions corresponding to antinodes in the modal electric field intensity.

Light emitted from the sample is collected with a retractable paraboloidal mirror positioned above the sample (collection angle up to $\pm 80^\circ$ from the surface normal). For spectroscopy and spectrally resolved CL imaging of the Ag sample, emitted light is sent through a grating monochromator before being focused on the photomultiplier tube detector. For panchromatic imaging, the light emitted from the sample is focused directly onto the photomultiplier detector, detecting photons with wavelengths ranging from 300 to 900 nm. Spectrally resolved CL images are obtained by setting the grating monochromator to a specific wavelength and scanning the electron beam over a selected area of the sample with a per pixel dwell time of 10 ms and a passband of 27 nm. Secondary electron and CL images are obtained simultaneously. The images were postprocessed to correct for the drift in the scan direction by shifting each

row of pixels of the SEM image to recreate the true annular resonator topography, and applying this same correction to the corresponding CL image. Any drift in the vertical direction is not corrected, explaining the elongated center region in several of the images. The single crystal Au sample was imaged using spectral detection on a CCD array detector, sampling wavelengths from 387 to 947 nm. Spectrally resolved images are obtained by taking slices through the compiled image with 20 nm spectral resolution.

3.3 Determining Modes of Annular Nanoresonators

We employ two different simulation methods to investigate the plasmonic modes of annular nanoresonators. Finite difference time domain (FDTD) calculations allow us to determine resonant frequencies and electric field profiles of each mode. With the boundary element method (BEM), we are able to calculate the probability of CL emission in an annular nanoresonator. Ultimately, these results are compared with the experimental results in Section 3.4.

3.3.1 Finite Difference Time Domain (FDTD)

First, we perform three-dimensional full-field electromagnetic simulations that solve Maxwells equations using the finite difference time domain (FDTD) method [59]. We assume that the optical constants of Ag are described by the Drude model:

$$\varepsilon(\omega) = \varepsilon_h - \frac{(\varepsilon_s - \varepsilon_h)\omega_p^2}{\omega^2 + i\omega\nu_c}, \quad (3.1)$$

with relative permittivity in the static limit $\varepsilon_s = 6.18$, relative permittivity in the high-frequency limit $\varepsilon_h = 5.45$, plasma frequency $\omega_p = 1.72 \times 10^{16} \text{ rad}\cdot\text{s}^{-1}$, and the collision frequency $\nu_c = 8.35 \times 10^{13} \text{ rad}\cdot\text{s}^{-1}$. We simulate a structure with 600 nm center diameter and 300 nm grating period using a cylindrical slab of Ag (400 nm thick, 4 μm diameter) containing annular grooves (50 nm deep, 150 nm wide, spaced 150 nm apart) all enclosed in a matrix of air. A propagating plane wave incident

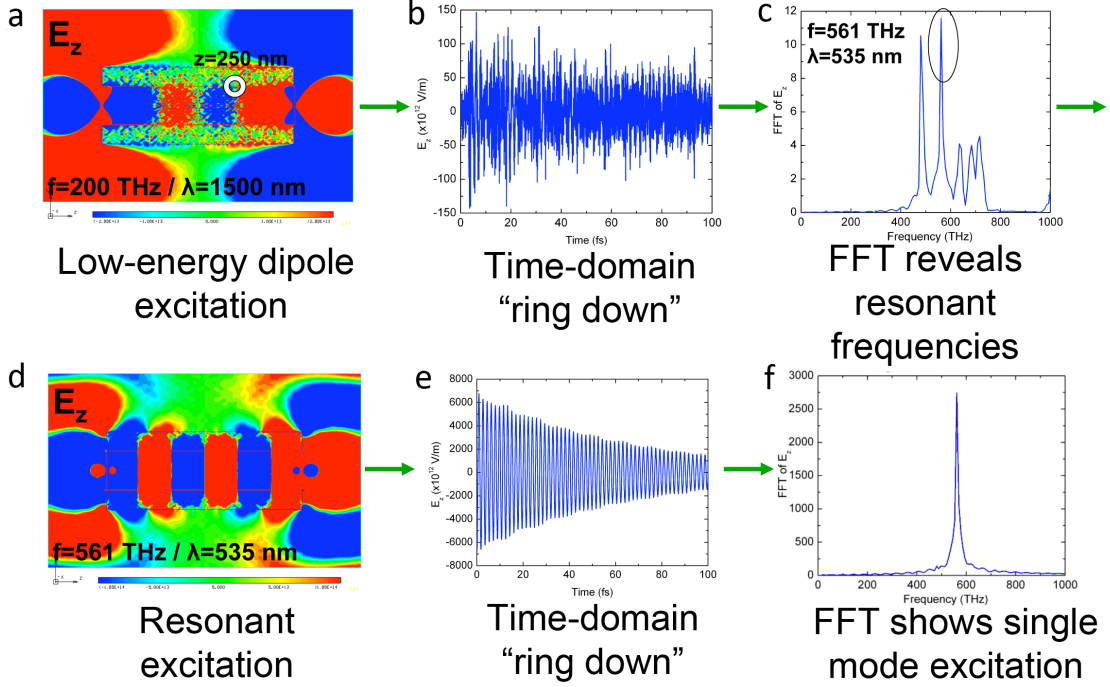


Figure 3.3. Method of determining resonant modes with FDTD, illustrated using a SiO₂/Ag core-shell nanowire resonator. (a) First, we excite with a low-frequency source, here dipoles at 200 THz or 1500 nm. (b) After 100 fs, the source is effectively turned off, and the fields in the resonator “ring down” for 100 fs. (c) A fast-Fourier transform (FFT) of the time-domain data reveals the resonant frequencies. (d) Exciting on resonance and (e) subsequent ring down demonstrates (f) single-mode excitation.

normal to the Ag surface is used as the source, polarized along an arbitrary direction in the plane of the surface. A two-step process is used to identify the resonant modes and their corresponding frequencies [60], illustrated in Figure 3.3. A SiO₂/Ag core-shell nanowire is used in this example. Here, the resonator is first excited with low-energy dipoles (frequency of 200 THz or $\lambda = 1500$ nm) at both ends of the wire, shown in Figure 3.3a. This distributes energy into all of the resonant modes. Then, after driving the structure at this frequency for 100 fs, the excitation source is turned off, leaving only the induced fields in the resonator. The structure is allowed to decay, or “ring down” for a period of 100 fs and the electric fields as a function of

time are monitored at specific locations in the resonator (marked with the white circle in Figure 3.3a). This time domain data is plotted in Figure 3.3b, a superposition of the decay from many modes. A fast-Fourier transform (FFT) of the time-domain data reveals clear peaks corresponding to the various resonant modes of the structure that are seen in Figure 3.3c. Selecting a specific mode, here the peak at the frequency $f = 561$ THz or $\lambda = 535$ nm, we then excite on-resonance with dipoles (Figure 3.3d) and again turn off the source to observe the time-domain decay. Figure 3.3e shows characteristic resonant decay, and a FFT of the time-domain data confirms single-mode excitation (Figure 3.3f). The time-domain ring down after resonant excitation also allows us to calculate the quality factor Q of the resonator. A single-exponential decay is fitted to the decay of $|E_x|^2$, and the decay constant τ is related to the quality factor by

$$Q = 2\pi f\tau. \quad (3.2)$$

For the Ag nanoresonators, the structure is first excited non-resonantly with a low-energy plane wave. The excitation is then turned off, and the induced electric fields ring down, allowing the resonator to select its natural frequencies in the absence of an external driving field. This method of illumination effectively contains a wide spectral intensity that is peaked around the frequency of the initial plane wave. Following the method of Figure 3.3, the time domain ring down data reveals the frequency response. Cathodoluminescence imaging spectroscopy is not a time-resolved technique, and a valid comparison between experimental results and simulations must include observables that are averaged over at least one optical cycle. The time-averaged electric field intensity was determined by squaring the magnitude of 25 three-dimensional electric field snapshots from a single time period at the end of the simulation, and averaging the result. Resonator modes with symmetries that are not supported by normal-incidence excitation were investigated with off-axis plane waves. The incident angle was chosen to impose the correct symmetry upon the center region of the nanoresonator.

3.3.2 Boundary Element Method (BEM)

Boundary element method (BEM) simulations [61, 62] allow us to calculate the probability of cathodoluminescence emission for various positions in the annular nanoresonators. Computations are performed in the frequency domain, where the electromagnetic field within each homogeneous region of space is expressed in terms of auxiliary boundary charges and currents. The customary boundary conditions are used to obtain a set of surface-integral equations involving those boundary sources, which are solved using linear-algebra techniques upon discretization of the boundaries via a set of representative surface points. Furthermore, the axial symmetry of the annular resonators is used to decompose the fields in uncoupled azimuthal components m with azimuthal-angle dependence as $e^{im\phi}$. This results effectively in a one-dimensional field calculation problem that is solved with great accuracy. Converged results for a nanoresonator of 600 nm center diameter and 300 nm period have been achieved using ~ 1000 discretization points. Calculated CL intensities are obtained using as an external source the field of a 30 keV electron, which is separated analytically in frequency components. The integral of the time-averaged Poynting vector over emission directions in the far field for each frequency component yields the CL intensity at that particular photon frequency. Tabulated optical data has been used as input for the dielectric function [34].

3.3.3 Resonant Modes

Full-field FDTD simulations are used to determine the plasmonic modes of an Ag annular nanoresonator with 600 nm center diameter and 300 nm grating ring period. We adopt a naming convention for the modes $M_{k,n}$, where the integer k refers to the symmetry of the mode ($k = 0$ for modes with nodes in electric field intensity in the center, and $k = 1$ for modes with intensity antinodes in the center) and the integer n denotes the number of intensity antinodes in the radial direction of the center plateau, extending outwards from the center of the structure and excluding peaks at the edges. These modes are shown schematically in Figure 3.4.

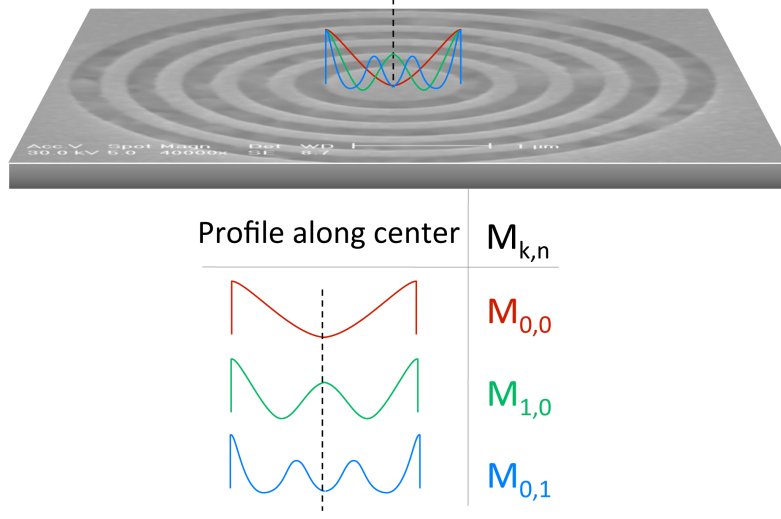


Figure 3.4. Schematic illustration of modes supported by annular nanoresonators. The naming convention $M_{k,n}$ is used to describe both the symmetry of the mode (k) and the number of antinodes along the center (n).

The FFT spectra for low-energy normal incidence plane-wave excitation at $\lambda = 1500$ nm in Figure 3.5a shows multiple features, including a peak at $\lambda = 330$ nm corresponding to the Ag surface plasmon resonance [11] and two broad peaks: one centered at $\lambda = 430$ nm and one in the 700–900 nm range.

Subsequent excitation in each of these two bands at $\lambda = 723$ nm (mode $M_{0,0}$, Figure 3.5b) and $\lambda = 430$ nm (mode $M_{0,1}$) leads to strong resonant response that we therefore attribute to plasmonic modes of the nanoresonator, with symmetry indicated in Figure 3.4. Off-axis plane wave excitation enables investigation of an additional spectral peak centered at $\lambda = 600$ nm (mode $M_{1,0}$), shown in the bottom figure of Figure 3.5b. Symmetry forbids excitation of this mode at normal incidence in our simulation, but off-normal incidence plane wave excitation breaks this symmetry constraint, and an antinode in electric field intensity is observed at the center. Characterizing the quality of these plasmonic nanoresonators is essential for development of future devices. We determine the quality factor [63] Q of the nanoresonator for each mode by (3.2) from the exponential decay time of the electric field intensity

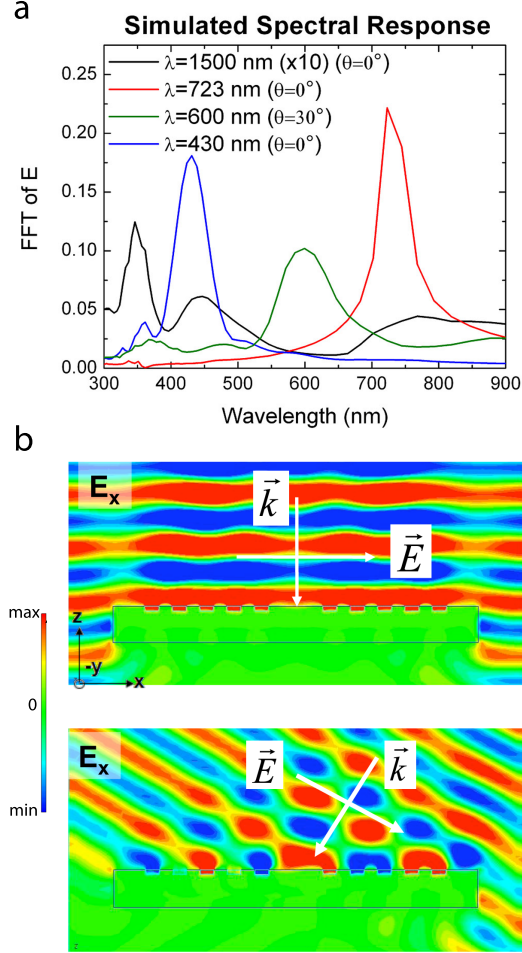


Figure 3.5. Determining modes with FDTD. (a) Simulated spectral-response for an Ag annular nanoresonator with 600 nm center diameter and 300 nm pitch for plane-wave excitation at the indicated wavelength and angle with respect to the normal. (b) Cross-sectional E_x profiles for plane wave excitation at normal incidence (top) and at $\theta = 30^\circ$ (bottom).

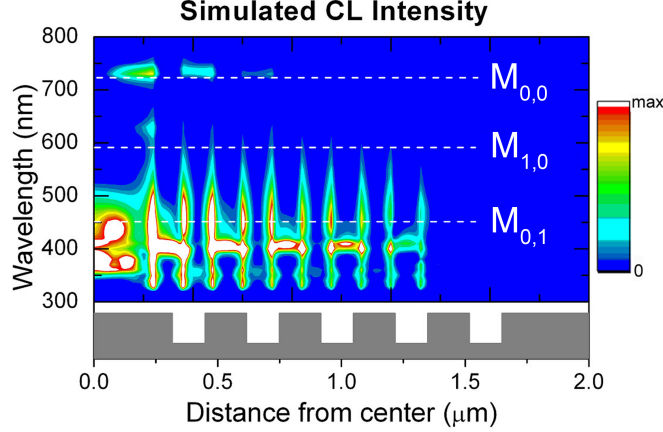


Figure 3.6. Boundary element method simulations of plasmonic modes of an Ag nanoresonator. Probability of cathodoluminescence emission is plotted as a function of excitation wavelength and position at a distance of 10 nm above the Ag topmost surface. Modes $M_{0,0}$, $M_{1,0}$, and $M_{0,1}$ are indicated at wavelengths of $\lambda = 720$ nm, $\lambda = 590$ nm, and $\lambda = 450$ nm, respectively.

during ring down, giving $Q_{0,0} = 36$, $Q_{1,0} = 18$, and $Q_{0,1} = 8$.

Using BEM simulations, we calculate the probability of cathodoluminescence emission as a function of electron beam position for this same structure. Figure 3.6 shows CL intensity as a function of both distance from the annular nanoresonator center and wavelength of emitted light. The CL probability is calculated by integrating the emission for directions from the grating normal up to 30° from the normal. At $\lambda = 720$ nm, bright CL intensity is concentrated only at the edge of the center plateau, characteristic of $M_{0,0}$. Mode $M_{1,0}$ is observed at $\lambda = 590$ nm, characterized by a small peak in emitted intensity at the center of the structure. At $\lambda = 450$ nm, a node in CL intensity in the center of the structure and one antinode along the radial direction distinguishes $M_{0,1}$. For this mode, bright CL emission is also localized at the edges of the center and concentric rings.

3.4 Imaging Modes Using Cathodoluminescence

We now investigate annular nanoresonators experimentally using CL imaging spectroscopy. The fabrication and experiment setup were described in Section 3.2.

3.4.1 Panchromatic CL Imaging

Figure 3.7 shows panchromatic CL images of nanoresonators in Ag with 315 nm grating period and three different center diameters. The CL images represent the radiation collected from the entire resonator as a function of the electron beam excitation position on the structure. Bright regions in the images correspond to greater emitted photon intensity. For all annular nanoresonators shown here, we see high intensity for excitation at the edges of the center as well as the concentric rings. The locally increased emission inside the grooves is attributed to scattering from roughness in the polycrystalline Ag film, formed because of the crystal orientation-dependent focused ion beam milling rate. The intensity line profiles in Figure 3.7e correspond to the dashed lines through the panchromatic CL image in Figure 3.7c and the correlated SEM image in Figure 3.7d. The CL profile clearly shows peaks in emission when the electron beam dwells near an edge. An overall decay in emission intensity is observed as the electron beam moves outward from the center. Thus, we see that a higher emitted photon intensity is obtained for electron beam excitation in the center of the structure, indicating that more efficient excitation and/or more efficient outcoupling occurs in this region.

3.4.2 Imaging Modes of an Ag Nanoresonator

Spectrally resolved CL imaging was used to experimentally reveal the plasmonic modes discussed in Section 3.3. Figure 3.8 shows SEM and spectrally resolved CL images of an annular resonator with a 620 nm center diameter and 315 nm grating period. At $\lambda = 350$ nm, very close to the Ag surface plasmon resonance, nearly uniform emission occurs for excitation anywhere in the structure. Near resonance, surface plasmon propagation lengths are very short, and thus no resonator modes can

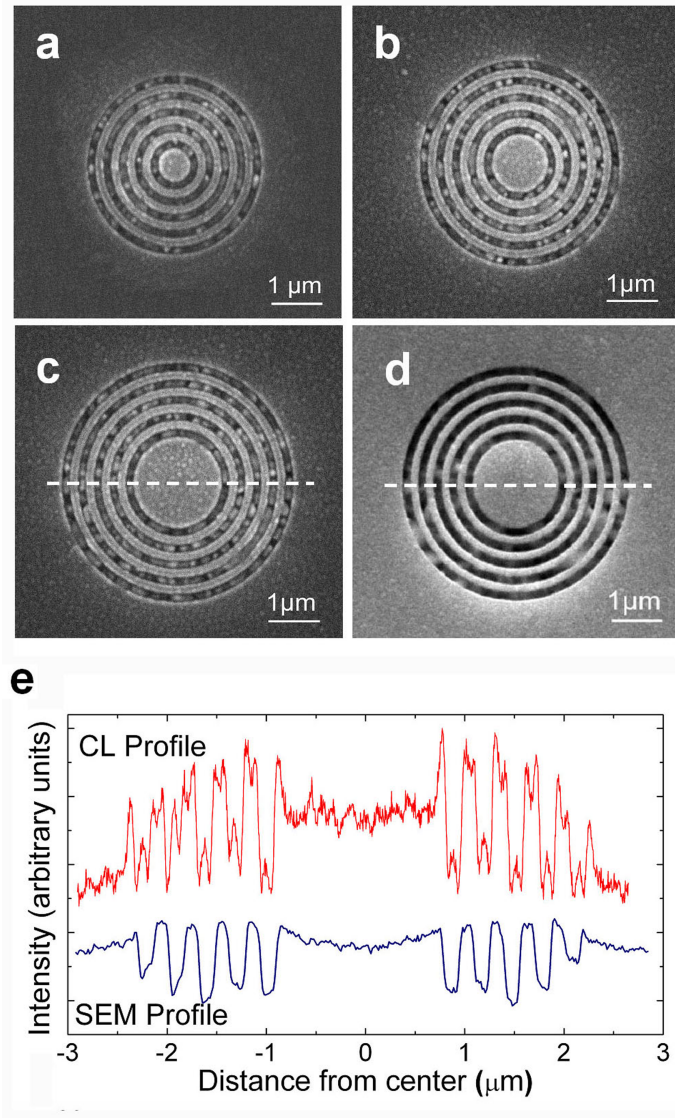


Figure 3.7. Panchromatic CL imaging of Ag annular nanoresonators with 315 nm period and center sizes of (a) 620 nm, (b) 1.07 μm , and (c) 1.70 μm . (d) SEM image taken concurrently with panchromatic CL image of structure in (c). (e) Line profiles from regions indicated by the dashed line in (c) and (d) illustrating strong emission when the electron beam is positioned at an edge and decreasing intensity as the beam moves outward from the center.

build up. Several different modes are observed at longer wavelengths, illustrated in Figure 3.8c. Line profiles of the simulated time-averaged electric field intensity from FDTD and the BEM-calculated probability of CL emission are plotted alongside experimental CL emission profiles for $\lambda = 500$ nm, $\lambda = 600$ nm, and $\lambda = 700$ nm. At $\lambda = 700$ nm, CL data show bright emission for excitation near the edges of the center plateau, but uniform emission from the rest of the structure. This is consistent with excitation of $M_{0,0}$, where high fields are localized at the edges of the center region and not in the surrounding rings. Mode $M_{1,0}$, imaged at $\lambda = 600$ nm, is characterized by an antinode in the resonator center that is captured in experimental and simulated line profiles. The onset of $M_{0,1}$ is observed at $\lambda = 500$ nm, with four peaks in the center region revealed in the CL linescan. These regions of enhanced emission in the center plateau correlate well with the simulated electric field intensity and CL profiles.

CL images and corresponding near-field $|\mathbf{E}|^2$ images from FDTD calculations are shown in Figure 3.9. Simulations require polarized excitation, whereas cathodoluminescence emission is unpolarized. Therefore, the images must be compared across the center (along the direction of polarization), indicated by the dashed white lines and plotted in Figure 3.8c. We also note that for modes $M_{0,0}$ and $M_{0,1}$, the best agreement between simulated and experimentally imaged modes is found for slightly different wavelengths. This can be attributed to uncertainty in parameterization of the effective dielectric function in the grooves of the fabricated Ag nanoresonators. The FIB milling of polycrystalline Ag leads to very rough surfaces in the grooves, preventing accurate representation of the groove depth and profile in simulations. The remaining spectrally resolved CL images in Figure 3.8a can be understood primarily as superpositions of $M_{0,0}$, $M_{1,0}$ and $M_{0,1}$.

3.4.3 Imaging Modes of an Au Nanoresonator

To further explore higher order modes in plasmonic nanoresonators, larger structures were fabricated in single crystal Au (Figure 3.10a). The absence of grain boundaries and hence longer propagation lengths enable clear observations of modes in larger

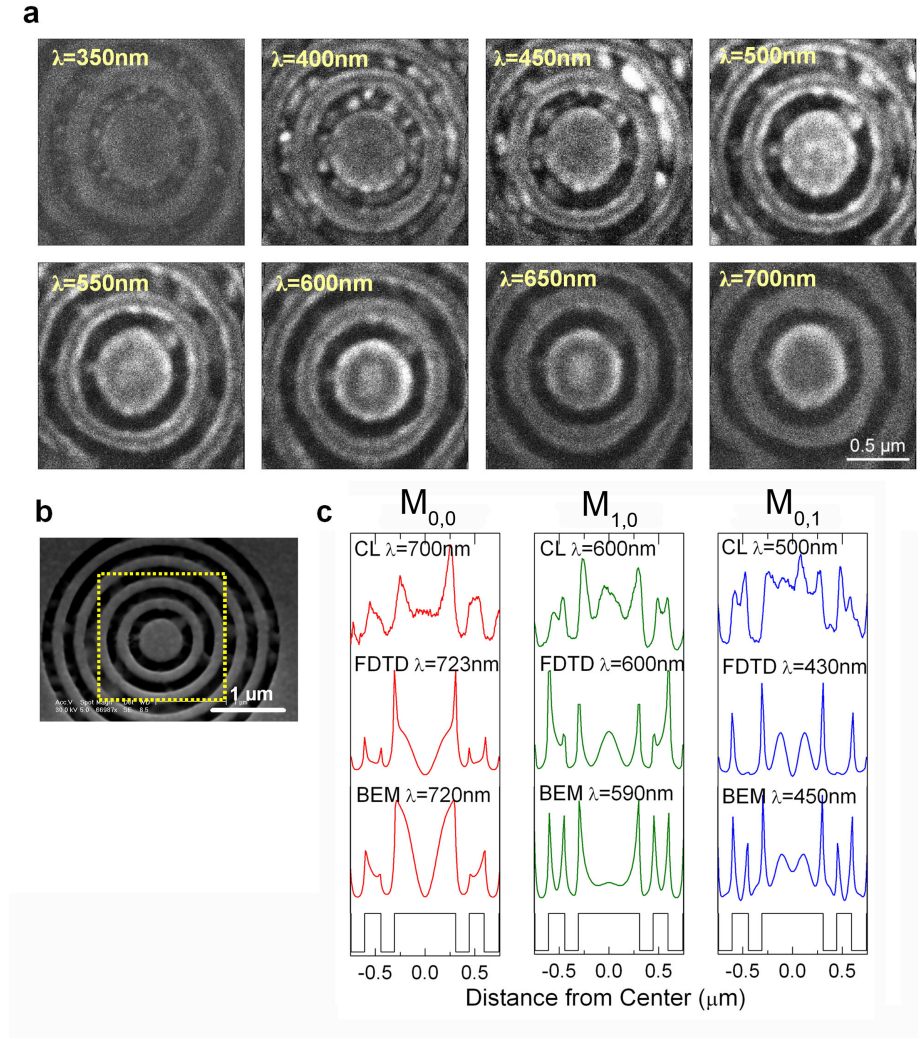


Figure 3.8. Spectrally resolved imaging of plasmonic modes in an Ag annular nanoresonator with 620 nm center diameter and 315 nm grating period. (a) Spectrally resolved CL images at the indicated wavelengths, each $350\times 350\text{ pixels}^2$ with a per pixel dwell time of 10 ms and 27 nm spectral passband. (b) SEM image of nanoresonator indicating the scan region for the CL images in (a). (c) Line profiles of modes $M_{0,0}$, $M_{1,0}$, and $M_{0,1}$ from FDTD simulated time-averaged electric field intensity, probability of CL emission from BEM simulations, and spectrally resolved CL images at the indicated wavelengths. The corresponding surface topography is shown in gray.

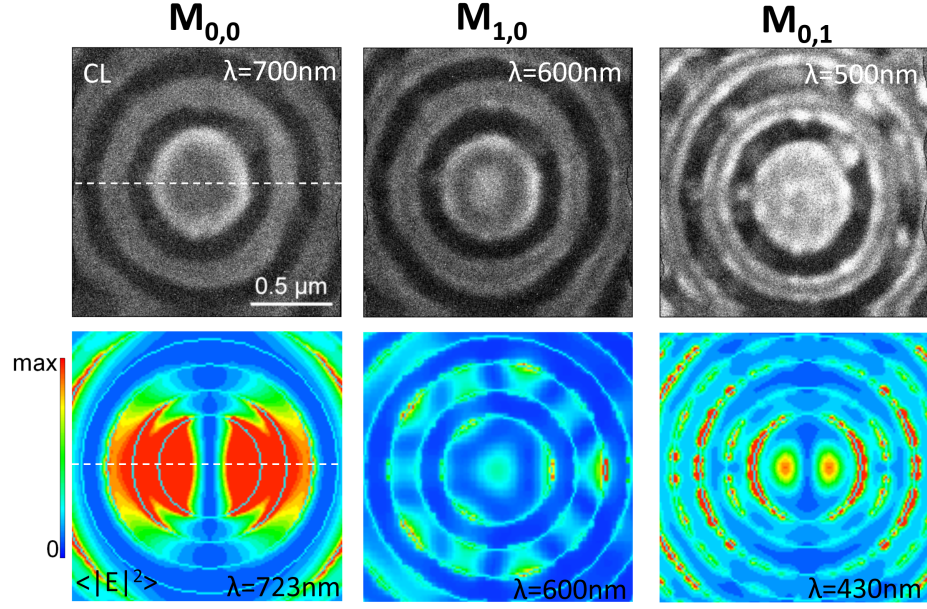


Figure 3.9. (top) CL images of modes $M_{0,0}$, $M_{1,0}$, and $M_{0,1}$ taken at the indicated wavelengths, and (bottom) time-average near-field electric field intensity maps from plane-wave excitation at the indicated wavelengths. Excellent agreement is found when comparing the intensities along the center of the images (indicated by the dashed white line).

resonators. Figure 3.10a shows spectrally resolved CL images of a resonator with a 2.6 μm center plateau surrounded by 15 concentric grooves with 250 nm grating period. The experimental line profiles in Figure 3.10b indicate that the CL emission along the center region varies with wavelength, showing modes with 5, 6, and 7 antinodes at wavelengths of $\lambda = 798$ nm ($M_{1,2}$), $\lambda = 720$ nm ($M_{0,3}$), and $\lambda = 661$ nm ($M_{1,3}$) respectively. The probability of CL emission is calculated from BEM simulations of this Au resonator, with the number of grooves truncated at five. Simulated CL intensity line profiles at wavelengths of $\lambda = 800$ nm, $\lambda = 730$ nm, and $\lambda = 660$ nm are also plotted in Figure 3.10b. Although the scan area of $5 \times 5 \mu\text{m}^2$ prevents experimentally resolving the simulated peaks in emission intensity at the edges of the grooves, excellent agreement is found between spatial variation of the experimental and calculated CL intensity along the center region for each mode.

3.5 Chapter Summary

In this chapter, we have demonstrated high-resolution spectrally resolved cathodoluminescence imaging as a powerful tool to reveal plasmonic modes in Ag and Au annular nanoresonators. Boundary element method calculations of the CL emission characteristics for each resonator mode agree very well with experimental results. Further, we have used full-field electromagnetic simulations to identify the plasmonic modes of Ag nanoresonators, and we have proposed a direct correlation between the luminescence emission intensity and electron beam excitation at antinodes of the electric field intensity corresponding to particular plasmonic modes.

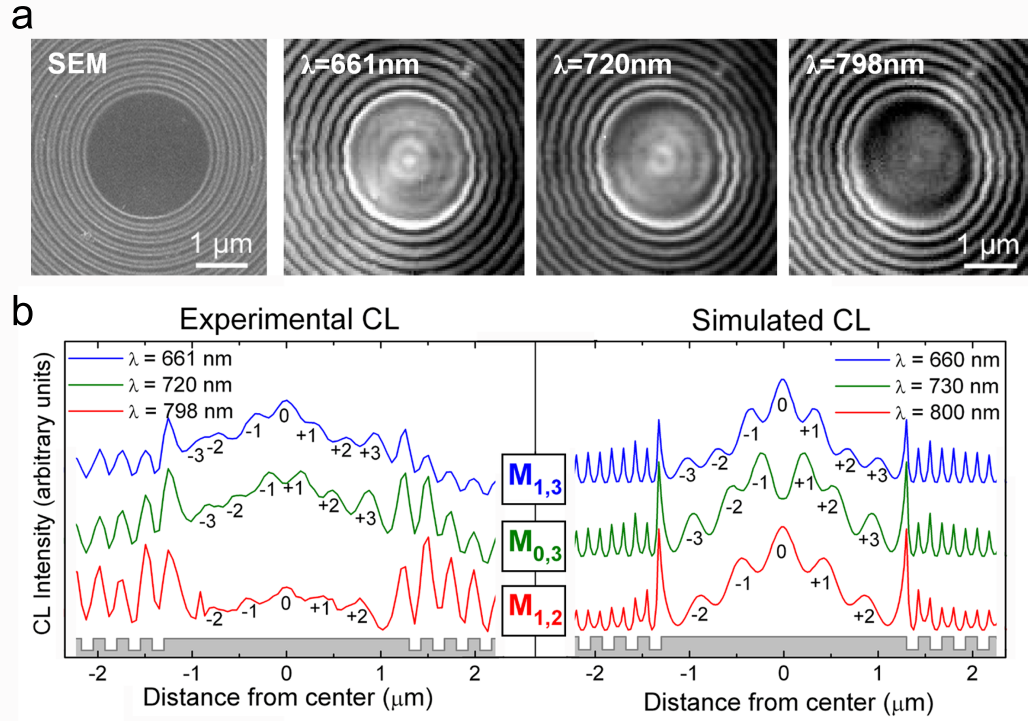


Figure 3.10. Imaging modes in a single-crystal Au nanoresonator with 2.6 μm diameter center plateau surrounded by 15 grooves with 250 nm grating ring period and 100 nm groove depth. (a) SEM image of nanoresonator and spectrally resolved CL images at the indicated wavelengths. (b) Line profiles of modes $M_{1,3}$, $M_{0,3}$, and $M_{1,2}$ from spectrally resolved CL images and simulated CL intensity along the center of the resonator in (a). Experimental line traces at the designated wavelengths are obtained by summation over 4 pixel lines in the horizontal direction, corresponding to a 193 nm line width. Simulated CL intensity is calculated from BEM simulations. The peaks in CL intensity along the center region are numbered for both experimental and simulated line profiles. Surface topography is shown in gray.

Chapter 4

Ultra-small mode volume Si-Ag core-shell nanowire resonators

4.1 Introduction

Until recently, any advances in the field of optics have been limited by diffraction. This restricts the size of all optical components to dimensions larger than half the wavelength of light it supports. The field of plasmonics has emerged with the unique ability to confine optical waveguide and resonator modes to volumes well below the diffraction limit. The extremely high and localized fields in these plasmonic nanocavities are finding applications in research areas such as single-molecule sensing, nanowire lasers, and fluorescence enhancement, among others. Plasmonic resonators, although they generally have low quality factors Q , are able to confine modes to subwavelength volumes V . Thus, when considering as a figure of merit the quantity Q/V , plasmonic structures become much more competitive with conventional optical resonators for applications where a resonance confined to a small volume is desirable.

Conventional dielectric resonators are renowned for their exceptionally high quality factors. For example, the silica toroid microcavity exhibits a Q of 4×10^8 , but with a large mode volume of $160(\lambda/n)^3$, where λ is the free space wavelength and n is the refractive index of the dielectric [64]. Taking advantage of the high confinement within plasmonic nanocavities, metallodielectric devices can be designed to support modes at subwavelength volumes. One of the most intensely studied plasmonic structures exhibiting high modal confinement over microns of propagation is the planar metal-insulator-metal (MIM) waveguide. An MIM cavity 107 nm wide

and 3 μm long with a 14 nm SiO_2 slot in Au has experimentally demonstrated mode volumes as small as $0.00383(\lambda/n)^3$ [13]. We have chosen to take advantage of the high confinement and low loss in MIM cavities in a cylindrical geometry as the core-shell nanowire resonator. These resonators are structures consisting of a cylindrical semiconductor or dielectric core and concentric metallic cladding (Figure 4.1). The core-shell resonator materials system explored here is a Si nanowire surrounded by an optically thick Ag cladding.

In this chapter, we demonstrate that plasmonic core-shell nanowire resonators confine modes to deeply subwavelength volumes while maintaining reasonable quality factors in extremely small structures. We use the boundary element method (BEM) to investigate Si-Ag core-shell nanowire resonators with a variety of dimensions, and for the resonant modes supported in each structure we determine the local density of states (LDOS), two-dimensional near-field intensity mode profiles, effective mode volume V , and quality factor Q . Additionally, we show that this geometry is well suited to obtain large Purcell factors and enhance the rate of spontaneous emission.

4.2 Resonant Modes of Si-Ag Core-Shell Nanowire Resonators

We investigate plasmonic core-shell nanowire resonators consisting of a Si nanowire core surrounded by an optically thick Ag cladding, shown schematically in Figure 4.1. These structures are defined by a core radius a , length L , and have a constant Ag coating thickness $T = 100$ nm. We use the boundary element method (BEM) to investigate resonators with a variety of dimensions, and for each mode we determine the LDOS, effective mode volume (V_{eff}), quality factor (Q), and enhancements in the total and radiative decay rates (Γ_{tot} and Γ_{rad} , respectively, normalized to decay in vacuum, Γ_0), and the corresponding quantum efficiency $\eta = \Gamma_{\text{rad}}/\Gamma_{\text{tot}}$.

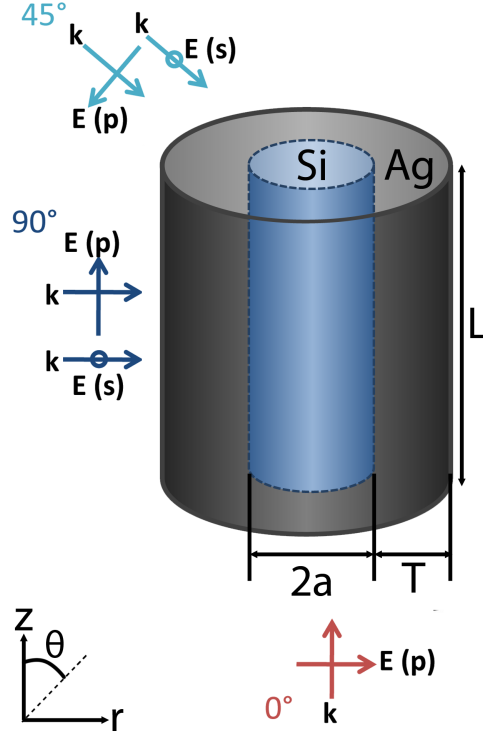


Figure 4.1. Si-Ag core-shell nanowire resonator, consisting of a Si core (radius a), Ag cladding (thickness T), and length L . Orientations for plane-wave excitation at $\theta = 0^\circ$, $\theta = 45^\circ$, and $\theta = 90^\circ$ (s - and p -polarized) are shown.

4.2.1 The Boundary Element Method

In BEM, calculations are performed in the frequency domain with the electromagnetic field in each homogeneous region expressed as a function of auxiliary boundary charges and currents. After applying boundary conditions, a set of linear integrals is obtained and solved by discretization. The axial symmetry of core-shell nanowire resonators allows decomposition of the fields into uncoupled azimuthal components m with azimuthal angular dependence $e^{im\phi}$. This results in an essentially a one-dimensional field calculation that is solved with great accuracy. The dielectric functions of Si and Ag are input using tabulated data. Converged results are found for $m_{\max} = 3$, using values of m defined by

$$m = -m_{\max}, -m_{\max} + 1, \dots, m_{\max} - 1, m_{\max}. \quad (4.1)$$

Resonant modes are determined by calculating the LDOS ρ for a dipole emitter oriented along the x direction using the relation

$$\rho = \frac{\omega^2 n}{3\pi^2 c^3} + \frac{1}{2\pi^2 \omega} \text{Im}[E_{\text{ind}}/D], \quad (4.2)$$

where ω is the resonance frequency, c is the speed of light in vacuum, n is the refractive index of Si, D is the dipole strength (unity in BEM), and E_{ind} is the contribution to the electric field due to scattering at the interfaces and projected along the direction of polarization. In contrast to the electronic density of states that describes the number of *electron* states at a given energy level that are available to be occupied, the LDOS counts the number of electromagnetic, or *photon*, states at a given frequency, location, and orientation of a dipole emitter. From (4.2), it is obvious that the LDOS depends on frequency, position, and orientation. The resonance quality factor, Q , is determined by fitting a Lorentzian lineshape to a plot of ρ versus ω , and

$$Q = \frac{\omega}{\Delta\omega}, \quad (4.3)$$

where $\Delta\omega$ is the full width at half maximum.

We use plane-wave excitation incident at $\theta = 0^\circ$, polarized along an arbitrary radial direction (see Figure 4.1), and determine the spatial near-field intensity profiles $|\mathbf{E}|^2$ of each mode. The effective mode volume, V_{eff} , is defined as a cylinder with length L_{eff} and radius a_{eff} determined by the $1/e$ decay distance of the peak field intensity inside the Si core.

4.2.2 Longitudinal Modes of Core-Shell Nanowire Resonators

If we consider a simple resonator cavity consisting of two parallel mirrors separated by a length L , basic optics tells us that a number of standing waves (modes) will be supported at wavelengths that satisfy the constraint $L = m\lambda/2$, where m is an integer. This is illustrated schematically in Figure 4.2, showing the modes at $\lambda = 2L$, $\lambda = L$, $\lambda = 2L/3$, and $\lambda = L/4$ illustrated here. Similarly, in a plasmonic cavity such as the core-shell nanowire resonator in the bottom of Figure 4.2, a number of longitudinal resonances are supported inside the Si core. However, plasmonic modes access larger k -vectors (shorter wavelengths).

Figure 4.3 shows LDOS calculations of the longitudinal resonances for four different Si-Ag core-shell nanowire resonators. The LDOS is calculated at a constant radial position of $r = 5$ nm from the center of the Si core, along the length of the wire, and reported with values normalized to the vacuum LDOS. The largest resonator (Figure 4.3a) has a core radius $a = 50$ nm and length $L = 500$ nm. A number of modes are supported, with the lowest-order $\lambda/2$ resonance occurring near $\lambda = 1000$ nm. Modes with higher-order azimuthal symmetry are supported at wavelengths below $\lambda = 750$ nm. Keeping the same Si core radius but decreasing the length to $L = 150$ nm, these higher order modes are cut off (Figure 4.3b). As expected, fewer longitudinal resonances are supported. The lowest-order $\lambda/2$ resonance, characterized by a high LDOS in the center of the resonator, has a resonant wavelength very close to the longer resonator in Figure 4.3a, but the second $\lambda/2$ resonance shifts from $\lambda = 980$ nm to $\lambda = 800$ nm. Also notable is that the lowest-order mode has higher LDOS in the smaller resonator.

Decreasing the resonator core radius a has a more marked effect on the wavelength

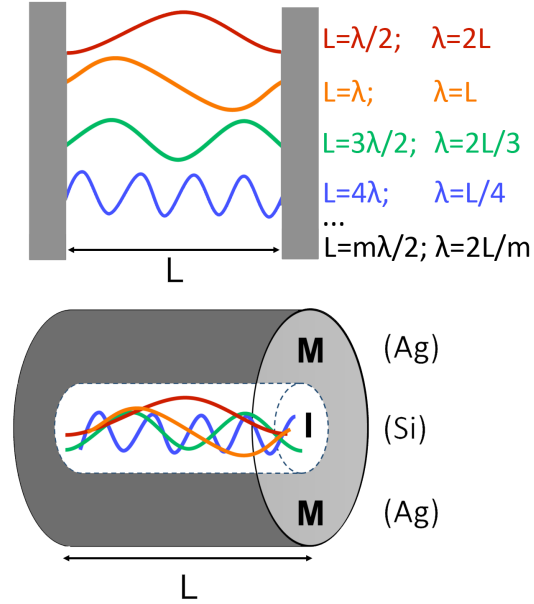


Figure 4.2. Top: Longitudinal modes of a resonator consisting of two parallel mirrors in vacuum separated by a distance L . Modes are supported at wavelengths that satisfy the constraint $L = m\lambda/2$, where m is an integer, with modes at $\lambda = 2L$, $\lambda = L$, $\lambda = 2L/3$, and $\lambda = L/4$ illustrated here. Bottom: Similar longitudinal mode profiles are found inside a Si-Ag core-shell nanowire resonator, at wavelengths much shorter than their free-space counterpart.

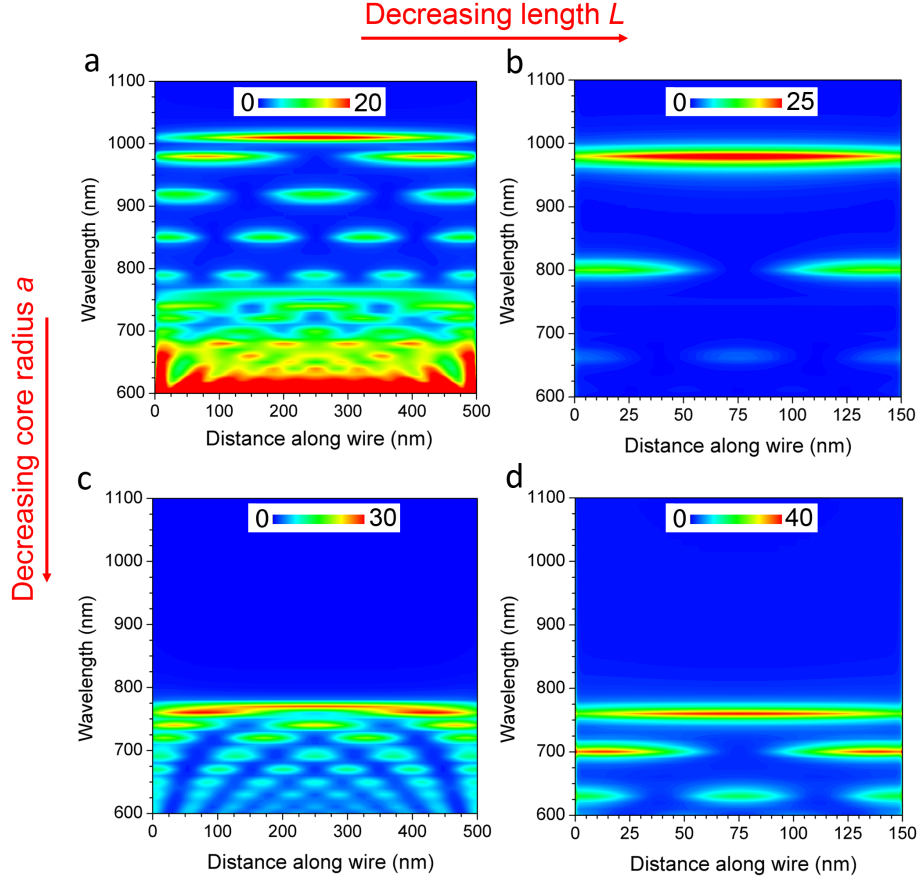


Figure 4.3. LDOS as a function of distance along the resonator length (z -axis) and wavelength for modes of Si-Ag core-shell nanowire resonators with dimensions (a) $a = 50$ nm, $L = 500$ nm, (b) $a = 50$ nm, $L = 150$ nm, (c) $a = 25$ nm, $L = 500$ nm, and (d) $a = 25$ nm, $L = 150$ nm. The LDOS is calculated at a constant radial position of $r = 5$ nm from the center of the Si core, along the length of the wire, and reported with values normalized to the vacuum LDOS. As length L decreases, fewer longitudinal modes are supported. As core radius decreases, modes shift to shorter wavelengths.

of the lowest-order longitudinal resonance. Comparing the modes of a resonator with $L = 500$ nm and $a = 50$ nm (Figure 4.3a) to a resonator of the same length but smaller radius $a = 25$ nm (Figure 4.3c), we can see that a similar number of longitudinal resonances are supported, but pushed to shorter wavelengths and spaced closer together spectrally. Furthermore, the higher-order azimuthal resonances in the larger resonator are not supported in the smaller structure. Again, this smaller resonator exhibits higher LDOS intensities than the larger structure.

Comparing the shorter resonators in Figs 4.3b ($L = 150$ nm, $a = 50$ nm) and 4.3d ($L = 150$ nm, $a = 25$ nm), similar trends are observed. The smaller resonator supports the same longitudinal resonances but at shorter wavelengths. Most importantly, the highest LDOS is seen in the smallest resonator. In Section 4.3, the modes of the resonators in Figures 4.3a and 4.3d are discussed in more depth.

4.3 A Case Study: 3 Resonators, 3 Size Regimes

Detailed results are presented for three resonators, each representing a different size regime: A ($a = 50$ nm, $L = 500$ nm, $T = 100$ nm), B ($a = 25$ nm, $L = 150$ nm, $T = 100$ nm), and C ($a = 5$ nm, $L = 25$ nm, $T = 100$ nm). Data for the largest resonator (A) are seen in Figure 4.4. The LDOS (Figure 4.4b) and NF $|\mathbf{E}|^2$ from plane wave excitation at $\theta = 0^\circ$ (Figure 4.4c) are calculated at a specific radial position ($r = 5$ nm from the center of the Si core) and plotted as a function of wavelength λ and distance along the wire. Many modes are supported, with the lowest-order $\lambda/2$ resonance occurring at $\lambda = 1010$ nm. Modes with similar longitudinal profiles but higher-order azimuthal dependence appear at shorter wavelengths in the LDOS plot, but symmetry prevents these modes from excitation with plane waves and they are not apparent in Figure 4.4c.

Two-dimensional NF $|\mathbf{E}|^2$ cross-sectional profiles of the first four lowest-order longitudinal resonances of resonator A are shown in Figure 4.5. The modes at $\lambda = 1010$ nm, $\lambda = 980$ nm, $\lambda = 920$ nm are excited with plane wave excitation at $\theta = 0^\circ$, and the $\lambda = 850$ nm resonance is excited at $\theta = 90^\circ$. For all wavelengths,

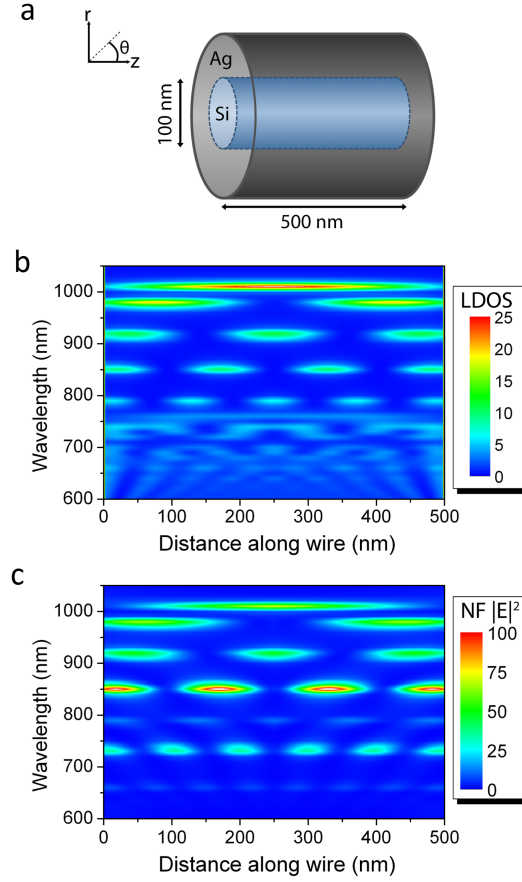


Figure 4.4. Resonant modes for a structure with Si core radius $a = 50$ nm, Ag coating thickness $T = 100$ nm, and length $L = 500$ nm (resonator A). (a) Schematic of this resonator. (b) LDOS as a function of wavelength calculated at a constant radial position of $r = 5$ nm from the center of the Si core, along the length of the wire (0 – 500 nm) with 2.5 nm resolution, and reported with values normalized to the vacuum LDOS. (c) Near field electric field intensity (NF $|\mathbf{E}|^2$) as a function of wavelength calculated from plane wave excitation at an angle of $\theta = 0^\circ$, also at a constant radial position of $r = 5$ nm from the center of the core and along the length of the wire.

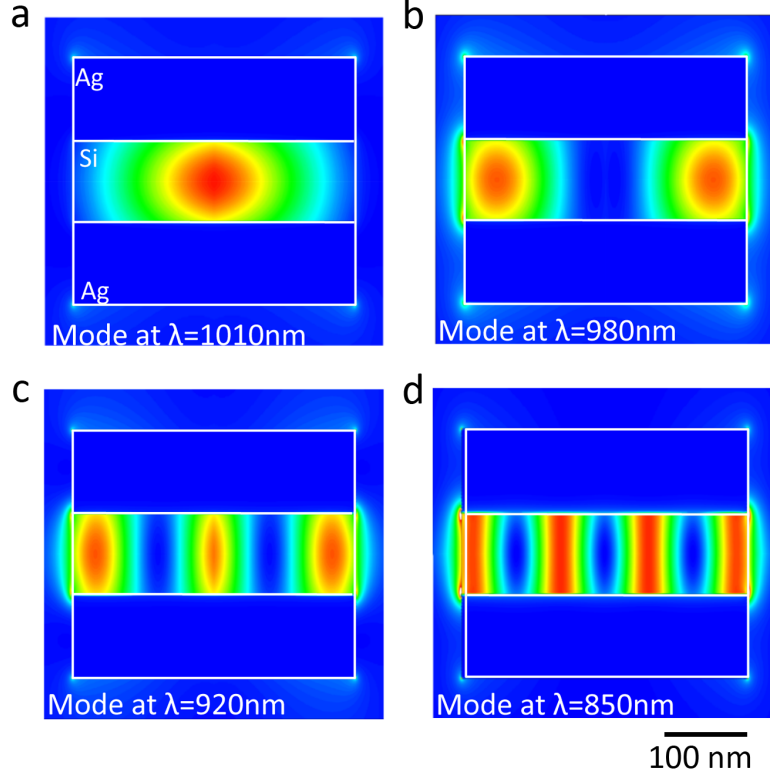


Figure 4.5. Two-dimensional NF $|\mathbf{E}|^2$ profiles for the first four lowest-order longitudinal modes for a structure with Si core radius $a = 50$ nm, Ag coating thickness $T = 100$ nm, and length $L = 500$ nm (resonator A) for excitation at (a) ($\theta = 0^\circ$) $\lambda = 1010$ nm ($\lambda/2$ resonance), (b) $\lambda = 980$ nm (second $\lambda/2$ resonance), (c) $\lambda = 920$ nm (λ mode), and (d) ($\theta = 90^\circ$) $\lambda = 850$ nm ($3\lambda/2$ resonance).

the modes are confined highly within the resonator core. The mode occurring at $\lambda = 850$ nm has the highest NF $|\mathbf{E}|^2$, and $Q = 79$ with a subwavelength mode volume of $V_{\text{eff}} = 0.32(\lambda/n)^3$. This results in a Q/V_{eff} of $247(\lambda/n)^{-3}$.

As expected, upon shrinking the resonator dimensions, modes shift to shorter wavelengths and modes with higher-order azimuthal symmetry are cut off. Figure 4.6 shows the LDOS and NF $|\mathbf{E}|^2$ mode profile for resonator B ($a = 25$ nm, $L = 150$ nm), calculated at a radial position of $r = 5$ nm from the center of the Si core and along the entire length of the resonator. Note the two-fold increase in LDOS as compared to resonator A for the two lowest-order $\lambda/2$ modes ($\lambda = 760$ nm and $\lambda = 700$ nm).

Plane wave excitation at $\theta = 0^\circ$ does excite the first three modes, but the mode at $\lambda = 700$ nm has the improper symmetry to be efficiently excited under these conditions. Excitation at $\theta = 90^\circ$ provides the proper symmetry for this second longitudinal resonance, characterized by high electric field intensity and LDOS at the resonator ends. Note also that the modes at $\lambda = 760$ nm and $\lambda = 700$ nm in this smaller resonator have higher intensity than the modes in the larger resonator A (Figure 4.4).

Figure 4.7 shows both LDOS and NF $|\mathbf{E}|^2$ cross-sectional profiles of the two lowest-order modes of resonator B. The LDOS profiles in Figure 4.7a are calculated only inside the Si core, with the rest of the resonator (Ag coating and surrounding air) shown for clarity. The mode at $\lambda = 760$ nm on the left is characterized by high LDOS in the center of the resonator core, whereas the mode at $\lambda = 700$ nm has high LDOS centered at the resonator ends and is a maximum radially at the Ag/Si interface. The two-dimensional NF $|\mathbf{E}|^2$ profiles for these modes are seen in Figure 4.7b. The mode at $\lambda = 760$ nm is excited with a plane wave at $\theta = 0^\circ$ polarized along an arbitrary radial direction. Strong fields are concentrated in the center of the Si core with high confinement within the resonator and very little penetration into the surrounding medium. Although this resonator is smaller than resonator B, we continue to see high confinement within the Si core. We calculate $Q = 58$ and V_{eff} equal to the physical volume of the Si core, $0.031(\lambda/n)^3$. This results in a Q/V_{eff} of $1870(\lambda/n)^{-3}$. For the second-order mode at $\lambda = 700$ nm, symmetry requires plane wave excitation at an angle of $\theta = 90^\circ$, polarized parallel to the longitudinal axis of the wire (z). The NF $|\mathbf{E}|^2$ profile in Figure 4.7b illustrates high electric fields at the resonator ends, and again little penetration into the metal cladding and surrounding vacuum. This mode has a Q of 53, $V_{\text{eff}} = 0.026(\lambda/n)^3$, and $Q/V_{\text{eff}} = 2040(\lambda/n)^{-3}$. Comparing these numbers to the larger resonator A, we see that smaller resonators continue to exhibit high mode confinement with effective mode volumes approximately equal to the physical volume of the Si core, and lower-order modes do not sustain much loss in quality factor with decreased dimensions. Thus, the figure of merit Q/V_{eff} increases significantly in this smaller resonator.

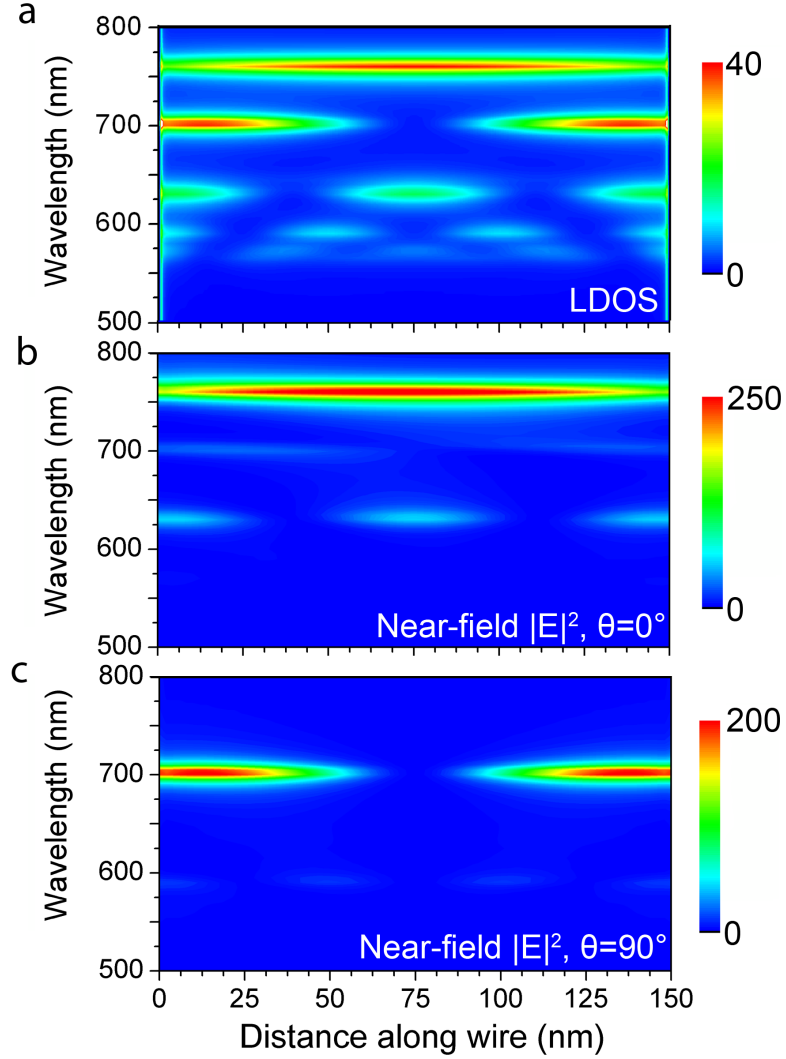


Figure 4.6. (a) LDOS and cross-sectional NF $|\mathbf{E}|^2$ profiles for plane wave excitation at (b) $\theta = 0^\circ$ and (c) $\theta = 90^\circ$ for a structure with $a = 25$ nm, $T = 100$ nm, and $L = 150$ nm. LDOS is calculated at a radial position of $r = 5$ nm from the center with 0.5 nm resolution along the length of the wire and normalized to LDOS in vacuum. NF $|\mathbf{E}|^2$ is also calculated at a radial position of $r = 5$ nm and normalized to the fields of the incident source.

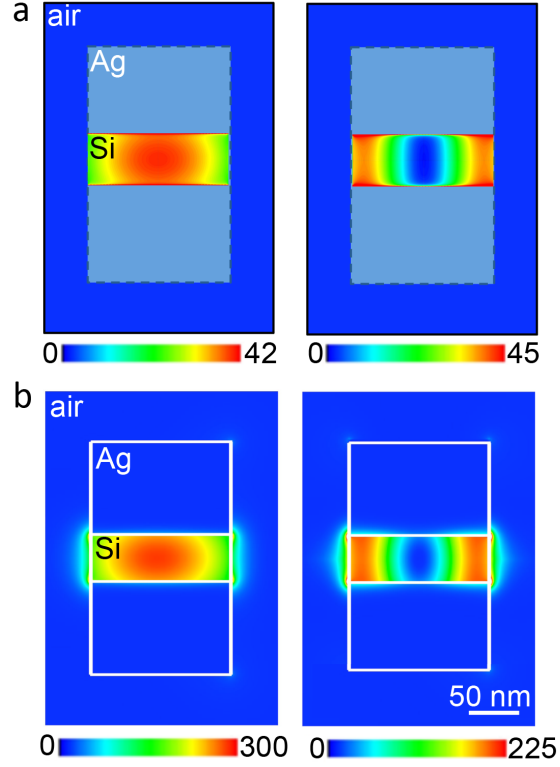


Figure 4.7. Cross sections of (a) LDOS and (b) NF $|\mathbf{E}|^2$ from plane wave excitation at (left) $\lambda = 760$ nm (plane wave excitation at $\theta = 0^\circ$) and (right) $\lambda = 700$ nm (plane wave excitation at $\theta = 90^\circ$).

Continuing to decrease resonator dimensions to the deeply subwavelength resonator C ($a = 5$ nm, $L = 25$ nm), only extremely evanescent modes are supported. As seen in Figure 4.8, the LDOS intensity increases dramatically, as does the NF $|\mathbf{E}|^2$ for plane-wave excitation at $\theta = 0^\circ$. We do not see the traditional longitudinal resonances in the plot of LDOS versus distance along the wire in Figure 4.8a because they are cut off. However, plane wave excitation at $\theta = 0^\circ$ shows a mode at $\lambda = 610$ nm for excitation at $\theta = 0^\circ$. From Figure 4.8c, we can see that the near-field intensity peaks at 4000 times larger than the incident field. This is by far the highest NF $|\mathbf{E}|^2$ of the three resonators studied in detail, and within the smallest resonator volume. Calculating $Q = 26$ and $V_{\text{eff}} = 4.7 \times 10^{-4}(\lambda/n)^3$, we find the highest Q/V_{eff} in this ultra-small resonator at $4.8 \times 10^4(\lambda/n)^{-3}$. Even for such small resonator dimensions, this mode volume is only 16% larger than the physical volume of the Si core with a quality factor that has decreased only slightly from the larger resonators. This demonstrates that upon transition from subwavelength resonators that support true eigenmodes to ultra-small resonators that support only evanescent modes, plasmonic core-shell nanowire resonators with dimensions on the order of $\lambda/50$ are able to confine modes within the physical volume of the resonator core without significant loss in the quality factor.

4.4 Enhancing Radiative Decay

We would also like to determine the light emission properties of the plasmonic core-shell nanowire resonators. An atom can emit or absorb photons by undergoing transitions between its energy levels through any of three specific processes: absorption, spontaneous emission, and stimulated emission [63]. If the atom, approximated as a two-level system with ground state energy E_1 and excited state energy E_2 , is initially in the lower energy level, an electron can be promoted from E_1 to E_2 by absorbing a photon with energy $> E_2 - E_1$. This process is called *absorption*, and can only occur when the radiation mode contains a photon.

An atom in the excited state with an electron in energy level E_2 can radiatively

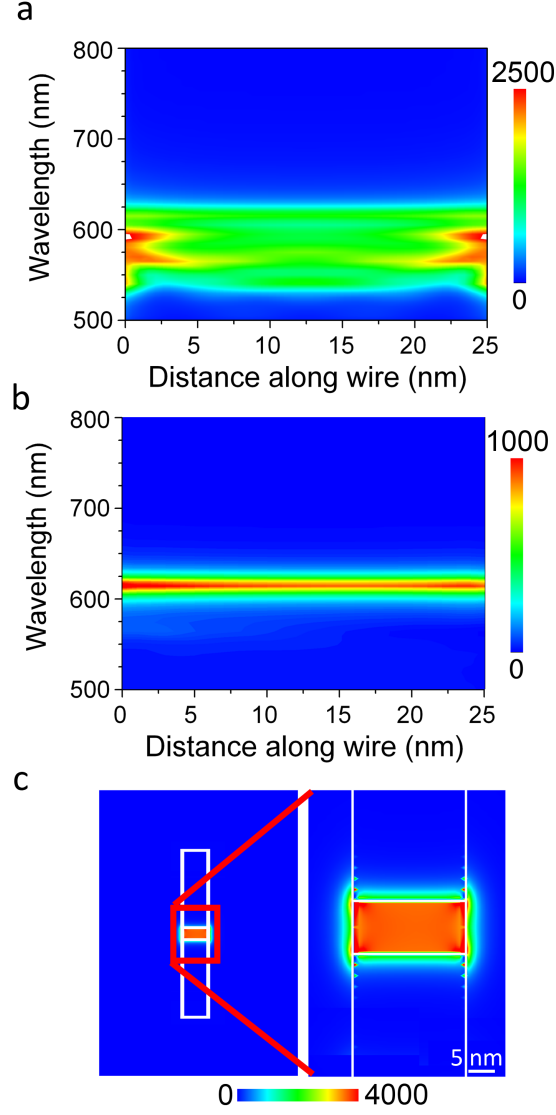


Figure 4.8. (a) LDOS and (b) NF $|\mathbf{E}|^2$ for plane wave excitation at $\theta = 0^\circ$ for a structure with $a = 5$ nm, $T = 100$ nm, and $L = 25$ nm. LDOS and NF $|\mathbf{E}|^2$ are calculated at a radial position of $r = 2.5$ nm with 0.2 nm resolution along the length of the wire. (c) NF $|\mathbf{E}|^2$ cross section for plane wave excitation at $\lambda = 610$ nm and $\theta = 0^\circ$.

decay to the ground state by undergoing either spontaneous or stimulated emission. In *spontaneous emission*, the atom decays to the lower energy state and releases energy in the form of a photon, with energy $E_2 - E_1$. This transition is independent of the number of photons occupying the mode. Alternatively, if the radiative mode already contains a photon, an atom in the excited state can be induced to emit an additional photon into the same mode. This process is *stimulated emission*, and is the inverse of absorption. Here, a preexisting photon with a specific energy, polarization, and orientation induces the emission of an identical photon. This process is the basis of laser operation. There are also nonradiative pathways for decay, such as the emission of phonons.

We are interested in opportunities for enhancing the rate of spontaneous emission. Fermi’s “golden rule” states that the rate of transition between two energy levels is directly proportional to the LDOS [65]. Therefore, by increasing or decreasing the LDOS, one can enhance or suppress the rate of spontaneous emission. This can be achieved in a number of geometries, particularly waveguides [66], antennas [67], and cavities [68].

Edward Purcell in 1946 discovered that the rate of spontaneous emission could be modified when the emitter is placed inside a resonant cavity [69]. This so-called Purcell effect states that the enhancement in the emission rate for maximum coupling is directly proportional to the quantity Q/V , as

$$F_P = \frac{3}{4\pi^2} \left(\frac{\lambda}{n} \right)^3 \left(\frac{Q}{V} \right), \quad (4.4)$$

where F_P , the Purcell factor, is equal to the enhancement of the spontaneous emission rate, λ is the free-space wavelength, n is the refractive index, Q is the quality factor, and V is the mode volume. The Purcell enhancement is illustrated in Figure 4.9. An emitter in free space has a continuum of states available to couple into. When the emitter is placed in a resonator cavity, which supports specific modes due to the boundaries, the rate of spontaneous emission can be modified by coupling into the cavity modes. This enhancement is most significant when the emission wavelength

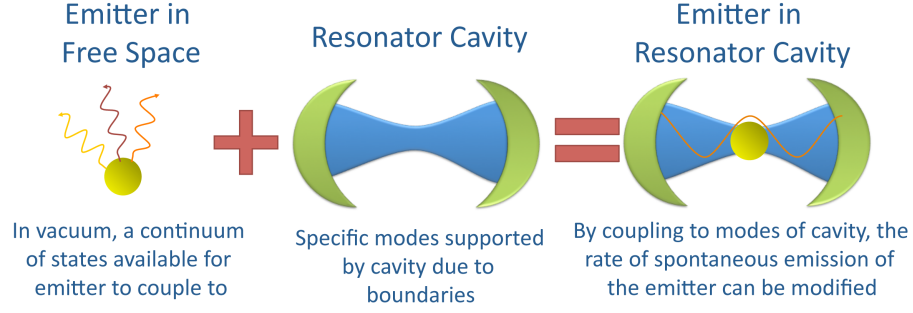


Figure 4.9. Illustration of Purcell enhancement of spontaneous emission in a cavity. A dipole emitter in free space can emit into a continuum of modes, but when placed inside a resonator cavity that supports specific modes, the rate of spontaneous emission of the emitter can be dramatically enhanced or suppressed.

corresponds to the wavelength of a cavity mode and when the emitter is positioned at the field maximum.

Considering (4.4), the maximum enhancement is obtained when Q/V is optimized. This is traditionally achieved by creating resonant cavities with ultra-high quality factors ($Q > 10^6$), but in volumes larger than $(\lambda/n)^3$. In plasmonic cavities such as the core-shell nanowire resonators described in this chapter, modes with low quality factors ($Q < 100$) are confined to subwavelength effective mode volumes V_{eff} and thus can achieve high figures of merit Q/V_{eff} . We have already reported the quality factors and mode volumes for the three resonators A, B, and C, reporting a maximum $Q/V = 4.8 \times 10^4 (\lambda/n)^{-3}$ in the smallest resonator (C).

We also determine what portion of the decay contributes to radiative emission versus absorption by calculating the enhancements in the total and radiative decay rates normalized to Γ_0 , the decay rate in vacuum, given by

$$\Gamma_0 = \frac{4}{3} \frac{|D|^2}{\hbar} \left(\frac{\omega}{c} \right)^3. \quad (4.5)$$

The total decay rate, Γ_{tot} , is related to the LDOS ρ as

$$\Gamma_{\text{tot}} = \frac{4\pi^2\omega|D|^2}{\hbar}\rho. \quad (4.6)$$

Finally, the radiative decay rate, Γ_{rad} , is calculated by integrating the far-field Poynting vector for a dipole source (polarized along r) located inside the Si core of the nanowire.

Results for resonators A, B, and C are shown in Figure 4.10. Peaks in the plot of $\Gamma_{\text{rad}}/\Gamma_0$ correspond to the resonant modes illustrated in Figures 4.4, 4.6, and 4.8. The largest enhancements are seen for the $\lambda = 610$ nm mode of the ultra-small resonator C, with $\Gamma_{\text{rad}}/\Gamma_0 > 13000$. Resonators A and B also see significant enhancements ($\Gamma_{\text{rad}}/\Gamma_0 > 100$ and $\Gamma_{\text{rad}}/\Gamma_0 > 400$, respectively), and both have quantum efficiencies $\Gamma_{\text{rad}}/\Gamma_{\text{tot}}$ of approximately 50%. Remarkably, the smallest resonator C maintains a reasonable quantum efficiency of 26%, again demonstrating the promise of ultra-small plasmonic core-shell nanowire resonators for enhancing the rate of spontaneous emission.

4.5 Core-Shell Nanowire Resonators as Sensors

Enhanced radiative decay suggests using plasmonic core-shell nanowires as molecular sensors. The simplest sensing experiments report a shift in the resonance wavelength when the surrounding medium is changed from air ($n = 1$) to a medium with a higher refractive index, such as water ($n = 1.33$) or sucrose ($n = 1.38$). The figure of merit for sensing is defined as

$$\text{FOM} = \frac{\Delta\lambda}{\Delta n}, \quad (4.7)$$

with units of nm/RIU (refractive index unit) where $\Delta\lambda$ is the shift in resonance wavelength and Δn is the refractive index change. The FOM can also be expressed in units of meV/RIU when

$$\text{FOM} = \frac{\Delta E}{\Delta n}, \quad (4.8)$$

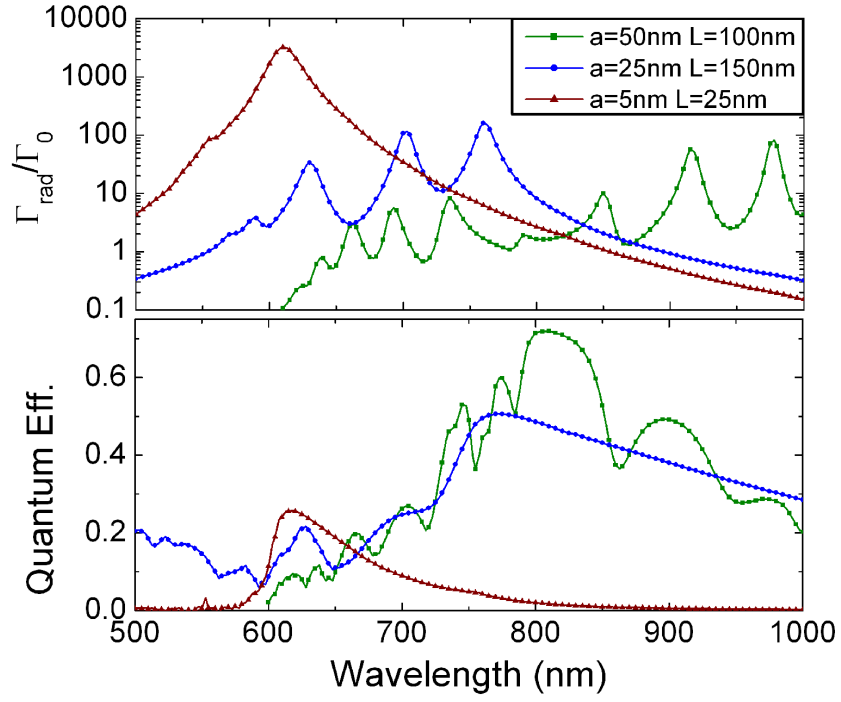


Figure 4.10. Radiative decay rate enhancements (top) and quantum efficiencies (bottom) as a function of wavelength for three different Si-Ag core-shell nanowire resonators. Quantum efficiency is calculated as $\Gamma_{\text{rad}}/\Gamma_{\text{tot}}$.

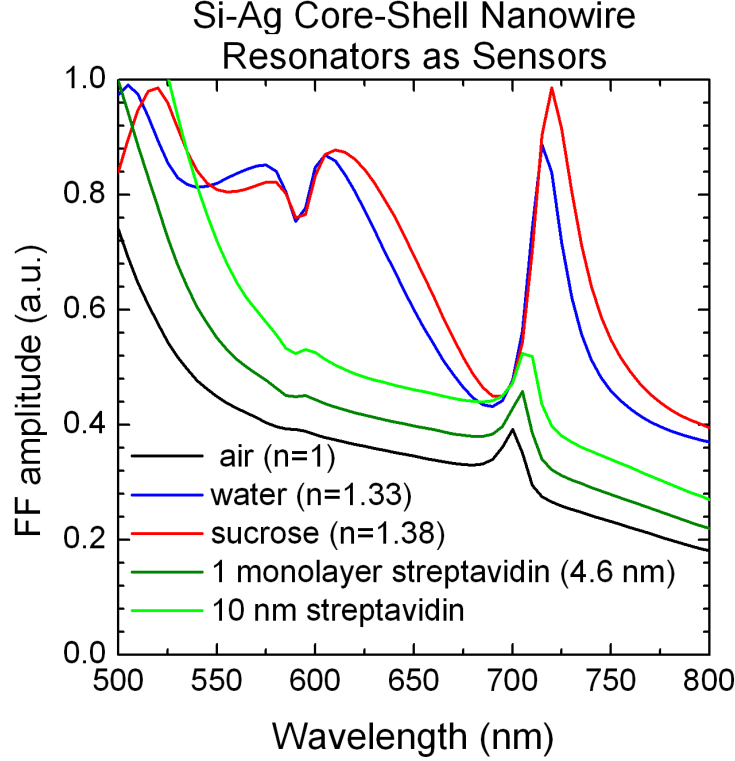


Figure 4.11. Far-field emission spectra for a Si-Ag core-shell nanowire resonator ($a = 25$ nm, $L = 150$ nm) in air ($n = 1$), water ($n = 1.33$), sucrose ($n = 1.38$), and with a single monolayer of streptavidin on one resonator end (4.6 nm) and a 10 nm layer of streptavidin, illustrating how these resonators can behave as sensors.

where ΔE is the shift in resonance energy. This FOM has been calculated for a number of small metal nanoparticles [70, 71, 72], and the metal nanostar demonstrate sensitivities higher than 1000 meV/RIU [73]. For resonator B ($a = 25$ nm, $L = 150$ nm), changes in far-field intensity for plane wave excitation at $\theta = 0^\circ$ for the resonator in air, water, and sucrose is shown in Figure 4.11. Significant spectral changes are observed, not only shifts in the resonance wavelength but also in intensity. When the resonator is situated in a higher index medium, more radiation to the far field is observed. We calculate a FOM for this resonator of 60 nm/RIU or 150 meV/RIU.

Significant effort has been devoted to developing sensors that are sensitive enough

to sense extremely small quantities of analyte, even to the single-molecule level. The biotin-streptavidin system is commonly used in sensing experiments. As a step toward designing single-molecule sensors, we have calculated the far-field emission spectrum for resonator B in air with a single monolayer of streptavidin coating one resonator end (thickness of 4.6 nm), as well as a 10 nm thick layer of streptavidin (Figure 4.11). This thin layer of streptavidin shifts the resonance wavelength and increases the intensity of emission.

4.6 Chapter Summary

In this chapter, we have introduced the Si-Ag core-shell nanowire resonator and performed a thorough investigation of its resonant modes using the boundary element method. A case study of three specific resonators, all with subwavelength dimensions, demonstrated that extremely high modal confinement is observed for all sizes. We calculated the radiative and total decay rates, and saw the most dramatic enhancements for the smallest resonator. A quantitative summary of these three resonators can be found in Table 4.1. Most importantly, we showed that resonators with dimensions on the order of $\lambda/50$ can still confine modes to deeply subwavelength mode volumes without significant loss in quality factor.

Table 4.1. Summary of Q/V and decay rate enhancements in Si-Ag core-shell nanowire resonators

radius a (nm)	50	25	5
length L (nm)	500	150	25
λ (nm)	850	700	610
V_{eff}	$0.32(\lambda/n)^3$	$0.026(\lambda/n)^3$	$4.7 \times 10^{-4}(\lambda/n)^3$
Q	79	53	26
Q/V_{eff}	$247(\lambda/n)^{-3}$	$2040(\lambda/n)^{-3}$	$55300(\lambda/n)^{-3}$
$\Gamma_{\text{rad}}/\Gamma_0$	115	445	13,520
$\Gamma_{\text{tot}}/\Gamma_0$	58	227	3,250
$\Gamma_{\text{rad}}/\Gamma_{\text{tot}}$	49%	50%	26%

Chapter 5

Fabrication and Characterization of Si-Ag Core-Shell Nanowire Resonators

5.1 Introduction

In Chapter 4, we discussed a theoretical investigation of Si-Ag core-shell nanowire resonators (Figure 5.1), and demonstrated that in this geometry, modes can be confined to ultra-small volumes. In this chapter, we address several routes to fabricating these resonators and methods of characterizing their optical properties. Both top-down and bottom-up fabrication are explored, and dark-field optical spectroscopy is used to investigate the properties of these resonators.

5.2 Fabrication of Si-Ag Core-Shell Nanowires

In this section, we describe the two methods employed for fabricating core-shell nanowires. The first is a bottom-up approach that begins with Si nanowires grown by chemical vapor deposition (CVD), and the second uses electron beam lithography (EBL) and reactive ion etching (RIE) to fabricate Si nanowires. In both cases, the Ag coating is deposited by RF-magnetron sputtering.

5.2.1 Bottom-Up Approach

The bottom-up fabrication method is shown schematically in Figure 5.2. The wires are grown using the vapor-liquid-solid (VLS) growth mechanism [74] with Au as a catalyst, following the method developed by Kayes et al. [75]. We begin with a

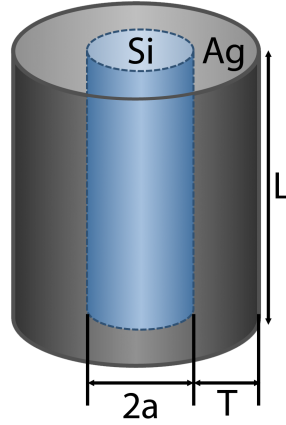


Figure 5.1. Si-Ag core-shell nanowire resonator, consisting of a Si core (radius a), Ag cladding (thickness T), and length L .

Si $\langle 111 \rangle$ substrate with 300 nm thermal oxide. The Au catalyst is patterned using photolithography and a mask consisting of 3 μm holes in a rectangular array with 7 μm center-to-center spacing. After pattern exposure, the SiO_2 in the exposed region is etched away with HF acid, leaving an oxide-free Si surface that will serve as the substrate for wire growth. Au catalyst (100 nm thick) is deposited using thermal evaporation. After liftoff, the Au dots are patterned only on top of the Si $\langle 111 \rangle$ surface and are separated from one another by SiO_2 . This prevents Au migration during the high-temperature CVD growth.

After Au patterning, nanowires were grown in a CVD reactor at 1000 $^\circ\text{C}$ with SiCl_4 and H_2 gas as the precursors. In the VLS method, Si from the SiCl_4 is absorbed by the liquid Au, forming a Au-Si alloy. The remaining Cl reacts with H_2 producing HCl gas. The Au-Si alloy at the wire tip passes through the binary eutectic point, upon which the Si solidifies and separates, forming the nanowire. The samples were first annealed in a tube furnace at 1000 $^\circ\text{C}$ for 20 min under 1 atm of H_2 at a flow rate of 1000 SCCM. Wires were then grown for 5 min at 1000 $^\circ\text{C}$ at 1 atm of H_2 and SiCl_4 , at flow rates of 1000 and 20 SCCM, respectively. For our purposes, short ($\approx 1 \mu\text{m}$) wires are grown. After growth, the Au catalyst tips are etched off using Transene Au etch TFA (KI-I₂ complex) for 3 min.

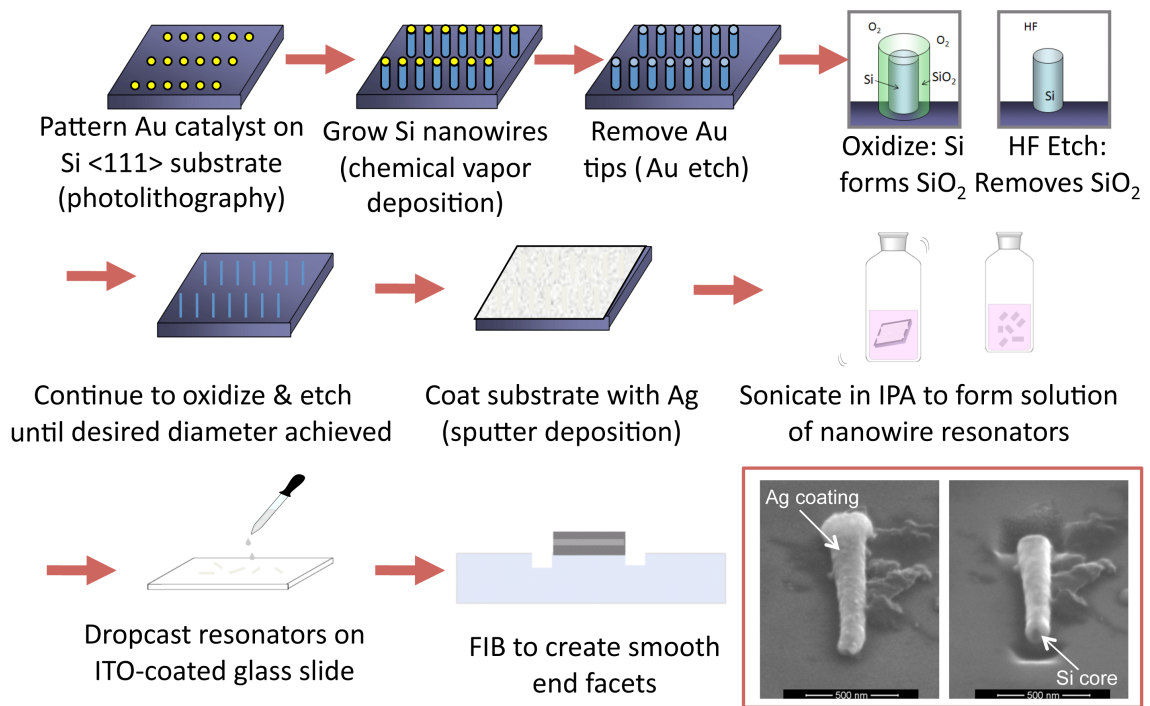


Figure 5.2. Bottom-up fabrication procedure for making Si-Ag core-shell nanowires. Si nanowires grown by Au-catalyzed CVD (VLS procedure) are oxidized and etched to reach a desired diameter of <100 nm, and coated with Ag by sputtering. After sonicating to disperse in IPA, wires are dropcast onto an ITO-coated glass slide and cut by FIB to the desired length and to attain smooth end facets.

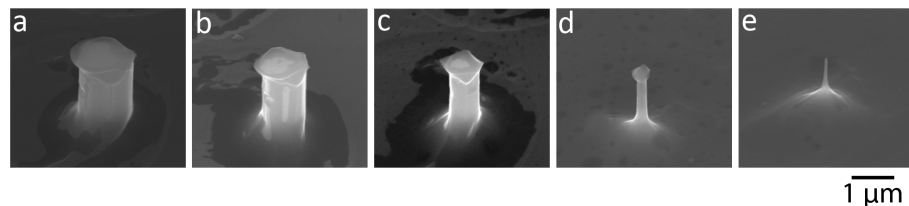


Figure 5.3. (a) A representative wire approximately $1.3\ \mu\text{m}$ in diameter after 3 hr of wet oxidation at $925\ ^\circ\text{C}$ and 5 min etching in BHF; (b) 900 nm diameter after 1.2 hr oxidation at $925\ ^\circ\text{C}$ and 2.75 min BHF; (c) 700 nm diameter after 3 hr oxidation at $950\ ^\circ\text{C}$ and 5 min BHF; (d) 200 nm diameter after 3 hr oxidation at $950\ ^\circ\text{C}$ and 5 min BHF; (e) 50 nm diameter after 45 min oxidation at $950\ ^\circ\text{C}$ and 5 min BHF.

The nanowire diameter and spacing are determined by the size and position of the Au catalyst on the growth substrate. Photolithography limits these dimensions to approximately $1\ \mu\text{m}$, which is much larger than the wire diameters explored in Chapter 4. To achieve smaller wire diameters, a series of wet oxidation and wet chemical etching was employed (Figure 5.3). The wires were oxidized in a tube furnace operating at $925\ ^\circ\text{C}$ and $950\ ^\circ\text{C}$ for times varying from 0.75 – 3 hr, creating a thick SiO_2 layer on the surface of the Si wire and growth substrate. This oxide layer was removed by submersion in buffered HF(aqueous) (BHF) acid for 5 min, after which the oxidation and etching procedure was repeated. Ultimately, the wire diameter was decreased from approximately $1.5\ \mu\text{m}$ to less than 70 nm.

A uniform Ag layer of 60 nm was deposited around the Si nanowire using RF-magnetron sputtering (Figure 5.4). The sample was placed in a cuvette with isopropyl alcohol (IPA) and sonicated for 30 s to form a solution of Ag-coated Si nanowires. Approximately $10\ \mu\text{L}$ of this solution was dropcast onto an indium tin oxide (ITO)-coated SiO_2 substrate in $1\ \mu\text{L}$ increments using a micropipette, and the IPA was allowed to evaporate between each droplet. Afterwards, a FIB with a Ga^+ source operating at 30 keV and 10 pA was used to cut the core-shell nanowires to desired lengths and to create smooth end facets.

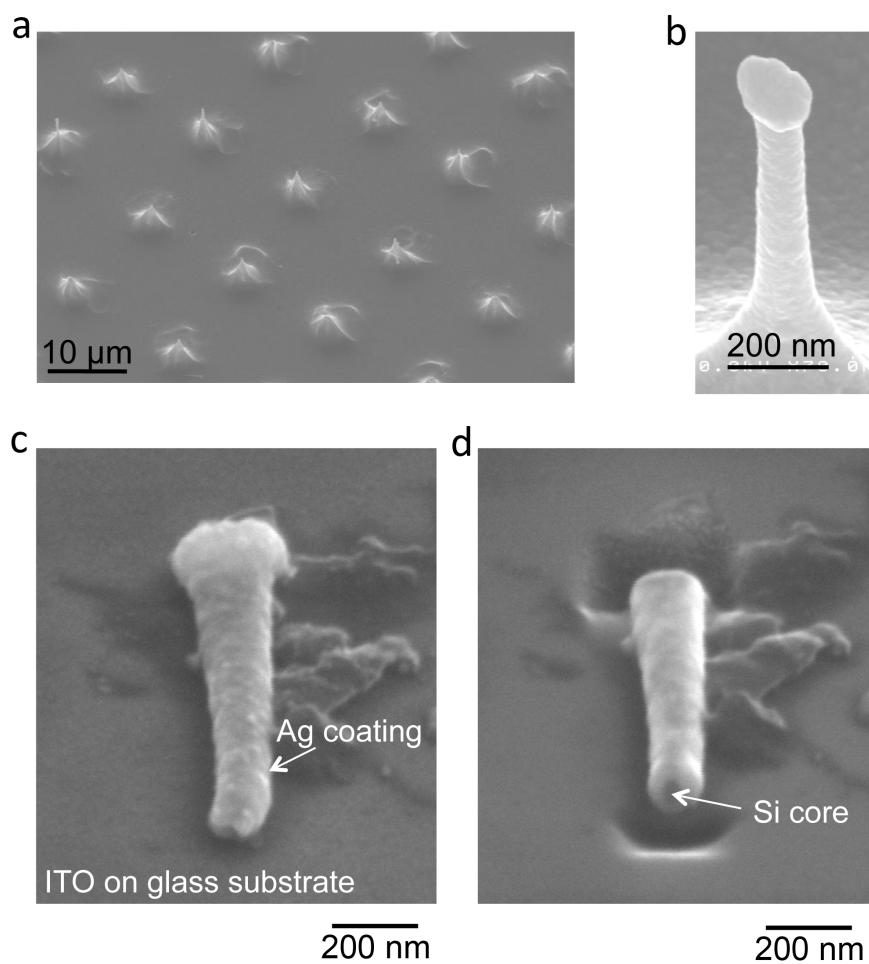


Figure 5.4. (a), (b) SEM images of Ag-coated NWs. (c) Ag-coated NW dropcast on ITO-coated glass substrate and (d) cut with FIB.

5.2.2 Top-Down Approach

We also investigate a top-down approach to fabricating Si-Ag core-shell nanowire resonators using EBL, RIE, and metal sputtering (Figure 5.5). Here, we start with a silicon-on-insulator (SOI) wafer with a 220 nm thick Si $\langle 100 \rangle$ device layer on 3 μm of SiO_2 on Si. On top of this, we spin a thin (75 nm) layer of poly(methyl methacrolate) (PMMA). Arrays of small holes 100 \times 100 μm^2 , 40–80 nm diameter with spacing from 1–20 μm are patterned in the PMMA using electron beam lithography and developed for 45 s in 1:3 MIBK:IPA. A 30 nm thick layer of Al_2O_3 is deposited by RF-magnetron sputtering. Although this technique results in conformal deposition, the swelling of the PMMA in acetone succeeds in fracturing the thin, brittle layer of the Al_2O_3 . Liftoff is performed by soaking the sample in acetone for 1 hr and then gently wiping the surface with a cloth-tipped swab. This results in small Al_2O_3 dots on the SOI that serve as a mask for RIE.

Arrays of Si nanowires 40–80 nm diameter are created by reactive ion etching through the top Si layer of the SOI wafer with Pseudo-Bosch ($\text{SF}_6/\text{C}_4\text{F}_8$) etch chemistry [76]. Afterwards, the Al_2O_3 mask is removed by etching the sample in a base-RCA clean with a solution of 5:1:1 $\text{H}_2\text{O}:\text{H}_2\text{O}_2:\text{NH}_4\text{OH}$ at 70 $^\circ\text{C}$ for 60 s. This procedure creates uniform Si nanowires 220 nm tall on the 3 μm oxide layer, as seen in Figure 5.6a before removal of the Al_2O_3 etch mask.

The metal cladding is formed by sputtering a 60 nm Ag layer over the sample, coating the Si nanowires. As shown in Figure 5.6b, this results in conformal coating of the sidewalls and substrate below, as well as creating a larger ball of Ag atop the nanowire. To perform experiments, we must obtain optical access to the Si core. The removal of excess Ag is achieved by sputtering in an Ar plasma. We find that after 3 separate sputtering steps of 5 min, 5 min, and 2 min, the excess Ag atop the nanowire, as well as the Ag on top of the SiO_2/Si substrate below, has been removed. Although primarily isotropic, the Ar plasma etch is just directional enough that the Ag removed from the sample is redeposited on the Si nanowire sidewalls to protect the cylindrical Ag coating during the etch. The resulting structure is shown in Figure 5.7.

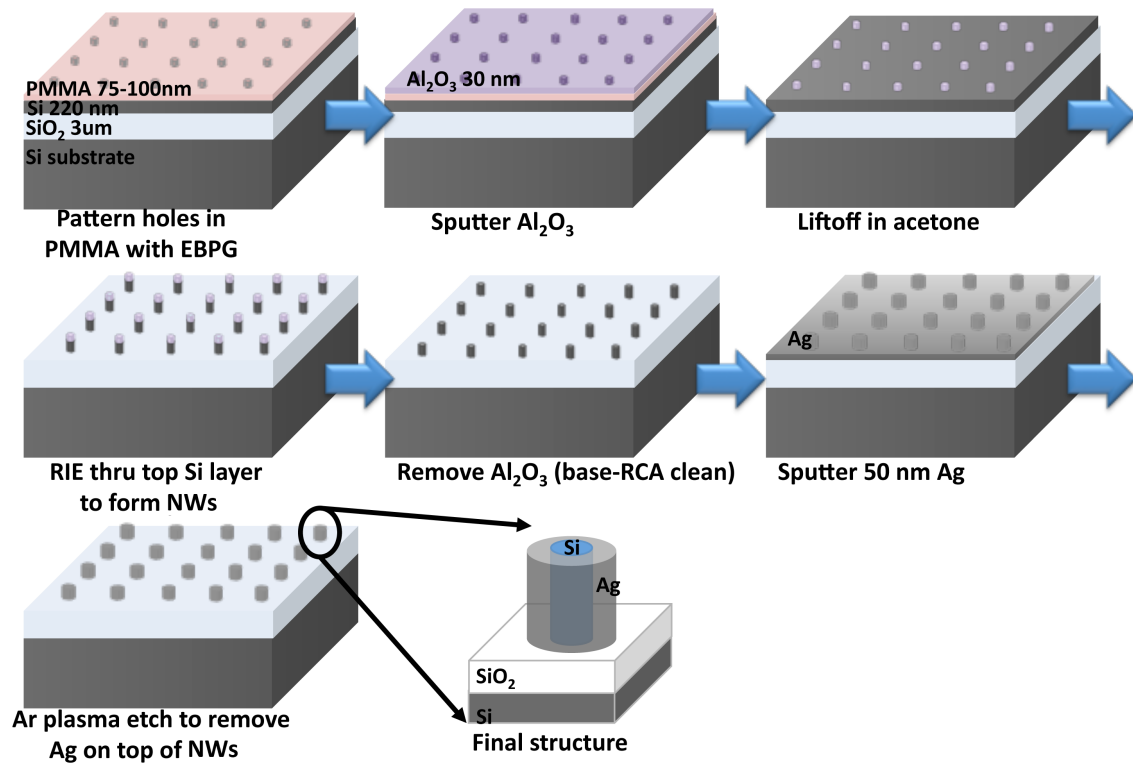


Figure 5.5. Top-down fabrication steps for Si-Ag core-shell nanowire resonators. Small dots of Al_2O_3 are patterned using electron beam lithography and liftoff, and used as an etch mask for RIE. Ag is deposited by sputtering and optical access to the nanoresonators is achieved by etching in Ar plasma.

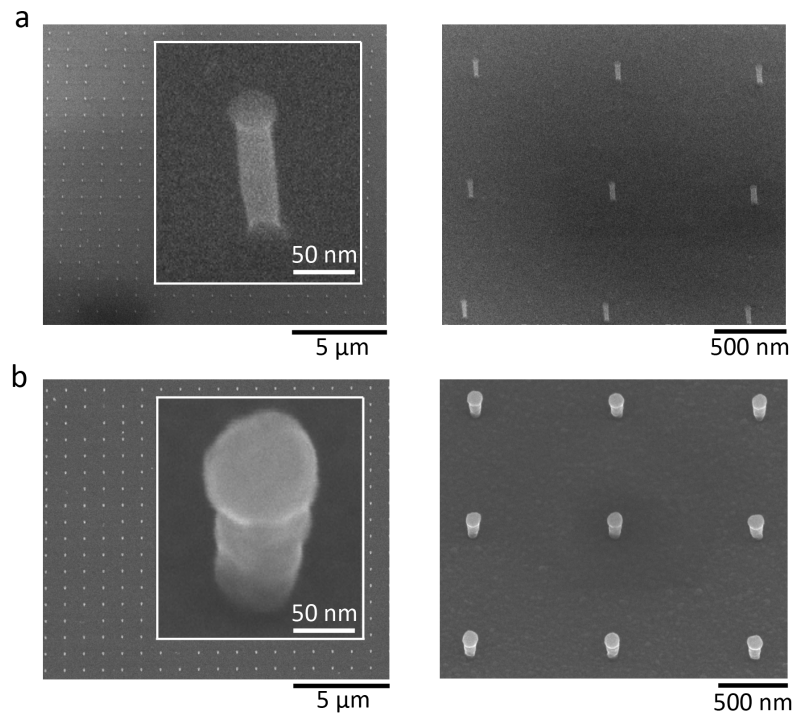


Figure 5.6. SEM micrographs taken at 30° tilt of (a) Si nanowires fabricated by electron beam lithography and reactive ion etching, and (b) Si nanowires coated with Ag by sputtering.

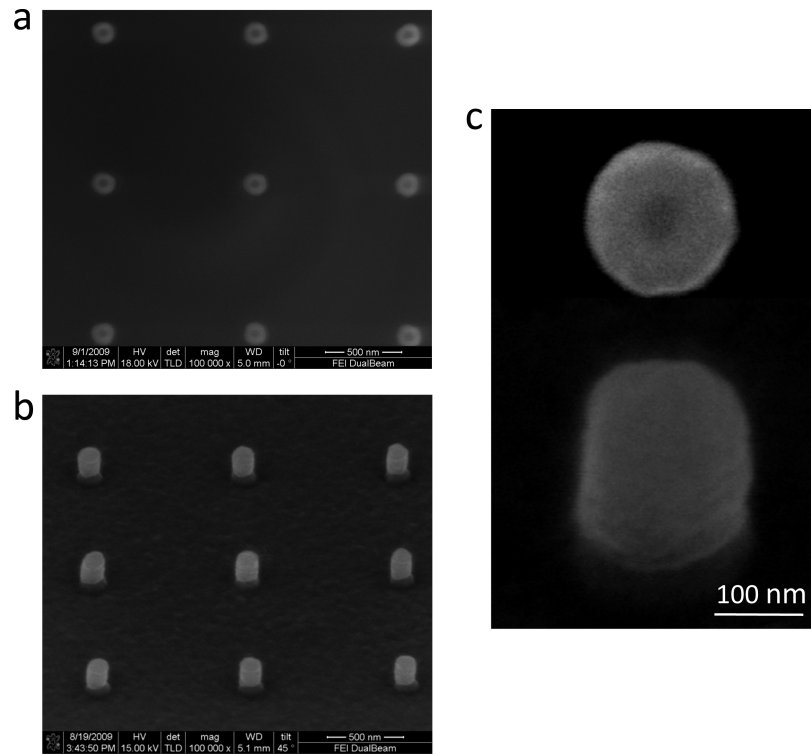


Figure 5.7. SEM images of fully-fabricated Si-Ag core-shell nanowire resonators after Ar sputtering to remove excess Ag taken at (a) 0° and (b) 45° tilt. Higher-magnification images are seen in (c).

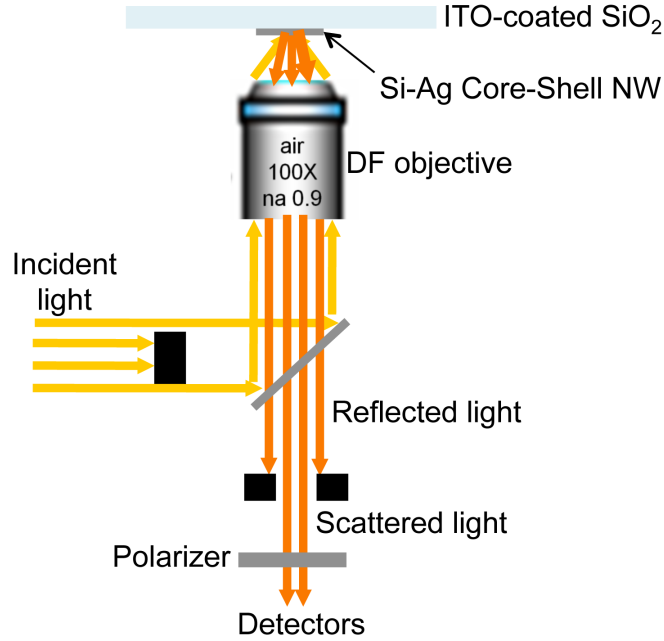


Figure 5.8. Schematic illustration of DF spectroscopy and imaging in an inverted optical microscope. This setup collects the scattered light from the sample, illustrated here as a Si-Ag core-shell nanowire on ITO-coated SiO_2 .

5.3 Optical Characterization

The Si-Ag nanowire resonators are characterized optically using a combination of bright- and dark-field spectroscopy. The experimental setup is seen in Figure 5.8. Incident light from an unpolarized halogen lamp is sent through a dark-field (DF) objective ($100\times$, 0.9 NA) that collects only scattered light from the sample. The light is focused into a monochromator and CCD spectrometer that allows spectroscopy to be performed on single nanowires, as well as arrays. A rotatable polarizer on a flip-mount in the detection path permits collection of polarization-resolved scattering spectra.

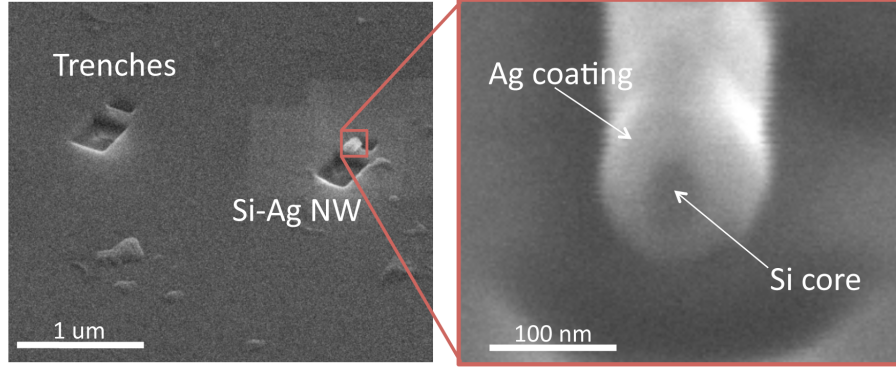


Figure 5.9. Left: SEM image of a FIB-cut Ag-coated Si NW and corresponding trenches used for normalization. Right: Close-up SEM image of Ag-coated Si NW.

5.3.1 Dark-Field Spectroscopy of Bottom-Up Fabricated Si-Ag Core-Shell Nanowires

We perform optical measurements on single nanowires fabricated by the bottom-up technique described in Section 5.2.1. As this technique measures scattered light, and the FIB-cut process creates subwavelength trenches that scatter the incident light, we also fabricated trenches near the core-shell nanowire as shown in Figure 5.9. Dark-field spectra are collected from both the wire and the corresponding trenches, and we ultimately report spectra corrected as

$$DF_{\text{corrected}} = \frac{DF_{\text{wire}}}{DF_{\text{trenches}}}. \quad (5.1)$$

As the close-up SEM in Figure 5.9 shows, this wire 250 nm in length has clean end facets, a Si core diameter of 50 nm, and Ag coating 50 nm thick.

Polarization-resolved dark-field scattering spectra of this core-shell nanowire are shown in Figure 5.10a. Here, the longitudinal axis of the nanowire is oriented along 0° – 180° . Several peaks are observed, the brightest at $\lambda = 450$ nm and $\lambda = 700$ nm. Maximum DF intensity is observed for 90° polarization, decreasing to a minimum at 0° and 180° . Calculations of the FF emission for plane wave excitation incident at $\theta = 45^\circ$ from the surface normal are also plotted in Figure 5.10a. We find good

agreement between the spectral peaks in the calculated emission spectrum and the experimental DF scattering spectrum at $\theta = 90^\circ$. Polar plots of the DF scattering intensity at several wavelengths are seen in Figure 5.10b. For all wavelengths, emission is oriented perpendicular to the longitudinal axis of the wire. Highest intensity is observed at $\lambda = 450$ nm.

5.3.2 Dark-Field Spectroscopy of Top-Down Fabricated Si-Ag Core-Shell Nanowires

We also performed dark-field spectroscopy measurements on the top-down fabricated Si-Ag core-shell nanowire resonators. These samples have arrays with varying Si core diameters and spacing between the resonators, allowing investigation of both individual resonators and collections of several resonators. A DF image is seen in Figure 5.11 for a $100 \times 100 \text{ } \mu\text{m}^2$ array with $5 \text{ } \mu\text{m}$ spacing between the wires, which shows significant response in the blue end of the spectrum.

Dark-field scattering spectra of approximately 15 resonators with $1 \text{ } \mu\text{m}$ spacing between the wires is shown in Figure 5.12a, for resonators with 60 nm, 50 nm, and 40 nm Si core diameters, 60 nm of Ag coating, and 220 nm tall. The spectra reported here are corrected to a background spectrum from another region of the sample by

$$DF_{\text{corrected}} = \frac{DF_{\text{wire}}}{DF_{\text{background}}}. \quad (5.2)$$

A number of peaks are observed in the DF spectra for the three different sizes, and the spectral positions of these peaks appear to be independent of the Si core diameter. However, the intensity of the peaks does depend on this dimension. If the spectral features were due to longitudinal modes of the resonator, one would expect the peak position to vary with the Si core diameter. Instead, these peaks originate from Fabry-Pérot oscillations in the SiO_2 film that couple to free space through the Si-Ag core-shell resonators. The DF spectrum in Figure 5.12b is from a single resonator with 50 nm Si core diameter, 60 nm Ag coating thickness, and 220 nm tall, and the same spectral features can be observed. Essentially, these resonators act as antennas that

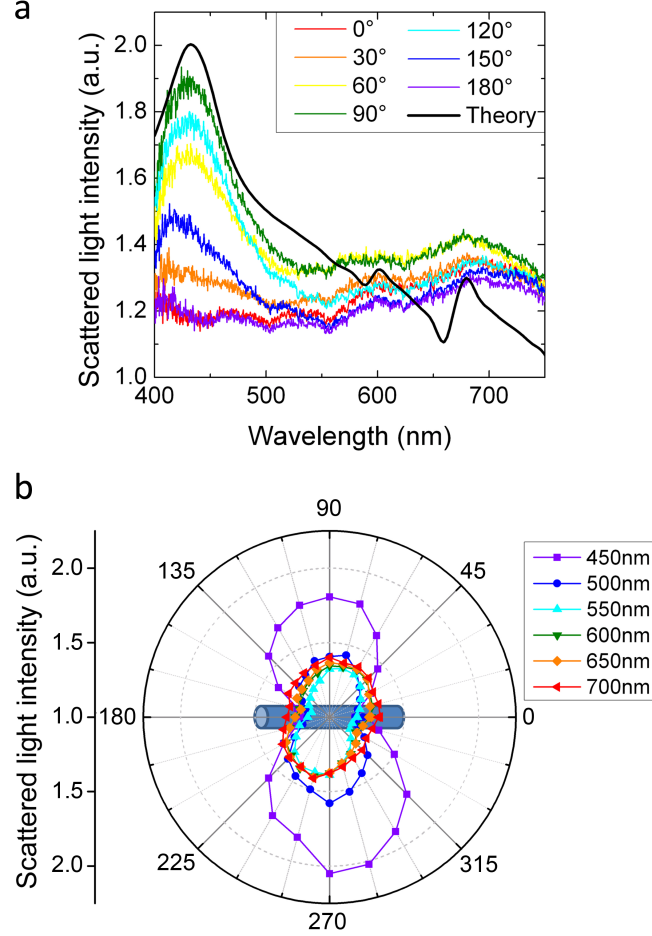


Figure 5.10. (a) Polarization-dependent DF scattering spectra from the NW in Figure 5.9. In black, theoretical results for BEM calculations of integrated FF intensity for plane-wave excitation at $\theta = 45^\circ$. (b) Polar plots of DF scattering intensity at wavelengths of $\lambda = 450, 500, 550, 600, 650$, and 700 nm. DF intensity is oriented along the transverse axis of the nanowire.

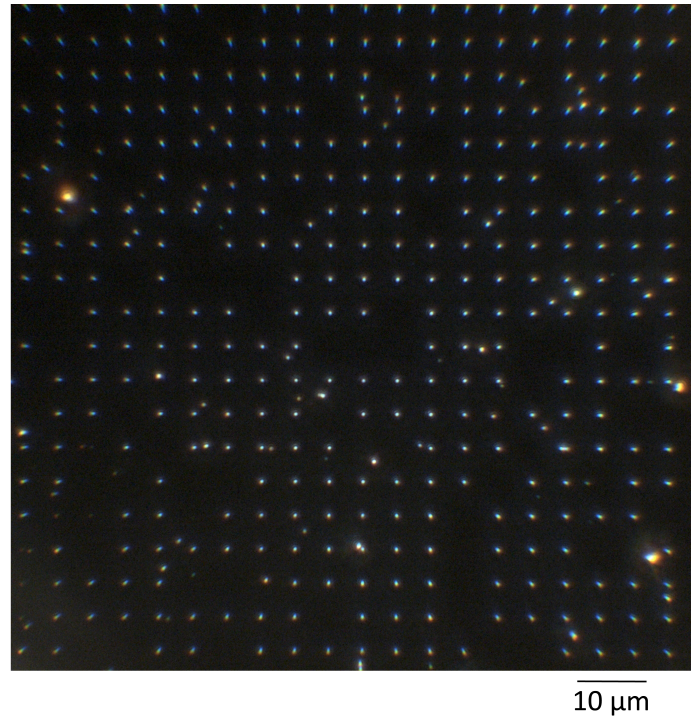


Figure 5.11. DF scattering image of Si-Ag core-shell NWs fabricated by EBL and RIE. By looking at arrays with different spacing, we can collect spectra from multiple and single nanowires.

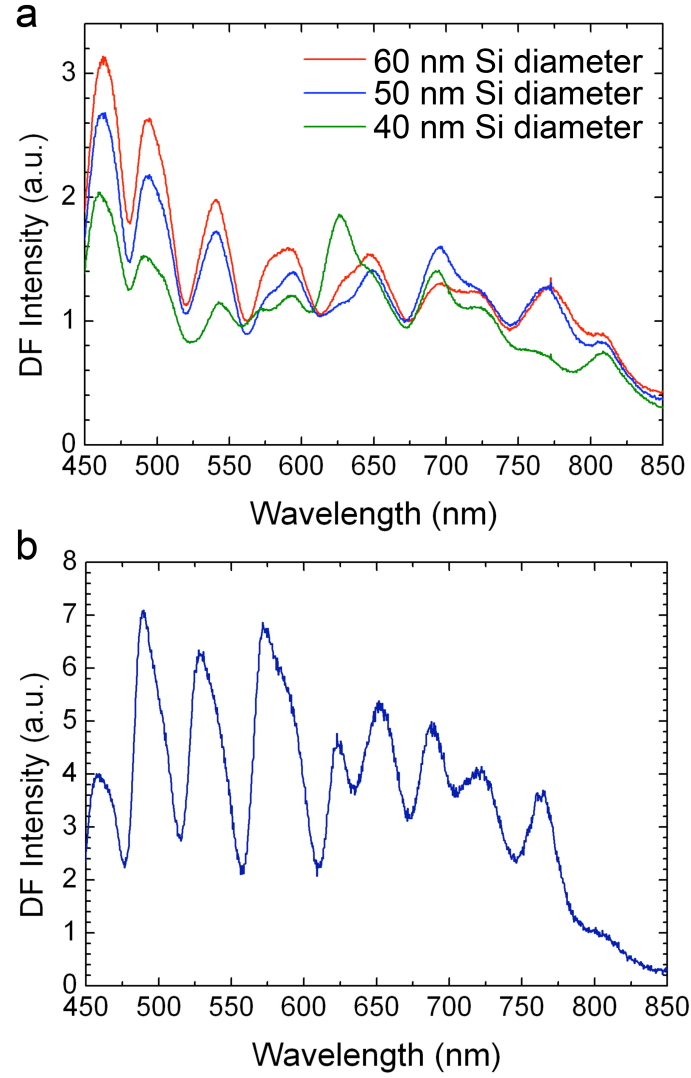


Figure 5.12. (a) DF scattering spectra of 15 nanowires in arrays with different core diameters, 60 nm, 50 nm, and 40 nm. (b) DF scattering spectrum of a single Si-Ag core-shell nanowire with 50 nm Si core diameter.

couple the Fabry-Pérot resonances to the far field. Determining the modes of the Si-Ag resonators uncoupled from the SiO₂ film on Si is not possible in this configuration, but will require removing the thick Si substrate.

5.4 Chapter Summary

In this chapter, we have described how to fabricate Si-Ag core-shell nanowire resonators by two methods. In the first, CVD is used to grow Si nanowires using the VLS process, and a series of oxidation and etching steps are used to create wires of the desired diameter. The Ag coating is deposited by sputtering. After sonication in IPA and dropcasting on ITO-coated SiO₂, the wires are cut to a desired length using FIB. We also used a series of EBL and RIE to fabricate Si nanowires in the top device layer of an SOI wafer, and fabricated the Ag coating by sputtering. Both approaches succeed in fabricating Si-Ag core-shell nanowires with <50 nm Si core diameter and <300 nm length. Optical characterization is performed in an inverted microscope in a dark-field configuration, and resonances are determined from the scattering spectra. As we showed in Chapter 4, these structures could be useful for sensing applications and, when incorporating light emitters into the Si core, for enhancing the rate of spontaneous emission.

Chapter 6

Enhancing the Rate of Spontaneous Emission in Active Core-Shell Nanowire Resonators

6.1 Introduction

Researchers have devoted considerable effort to enhancing light emission from semiconductors and molecules using optical geometries that exhibit high Purcell factors [69]. To effectively enhance the rate of spontaneous emission, one must maximize the quantity of Q/V . This is traditionally achieved by designing dielectric resonators with high quality factors, Q . Although plasmonic nanocavities generally support resonant modes with low quality factors ($Q < 50$), these modes are highly confined to subwavelength mode volumes ($V \ll (\lambda/n)^3$) and can also exhibit very large Purcell factors. It has long been recognized that metal films and nanostructures can enhance the fluorescence of molecules [77, 78] and semiconductors [79, 80], and since then a number of more complex plasmonic nanoparticle and nanoantenna geometries have been employed to modify the spontaneous emission rate [81, 82]. Recently, plasmon-enhanced stimulated emission was demonstrated in two new devices, the spaser (surface plasmon amplification by stimulated emission of radiation) nanolaser [83] and the plasmon laser [84]. Here, we demonstrate an equally dramatic effect on the spontaneous emission rate of inorganic semiconductors in ultra-small mode volume cavities.

In this chapter, we investigate plasmonic core-shell nanowire resonators consisting

of a III-V compound semiconductor heterostructure nanowire core surrounded by an optically thick Ag coating, shown schematically in Figure 6.1. Enhancing the spontaneous emission rate of III-V semiconductors is of particular interest because they have high internal quantum efficiency and an ability to form high-quality heterostructures. We will use a method similar to Chapter 4 to investigate these structures, but now incorporate active III-V semiconductor light emitters into the semiconductor core.

6.2 Theoretical Methods

The semiconductor heterostructure core has an active light emitting region (length L_A , radius a) clad on all sides with a larger band-gap material (length L_C and thin spacer layer thickness s), an Ag coating thickness T , and a total resonator length $L = L_A + 2L_C$ (Figure 6.1). This geometry allows for significant modification of the local density of optical states (LDOS), which describes the available optical eigenmodes for photons at a specific position, orientation, and frequency. The decay rate of excited atoms is proportional to the LDOS. Changing the material and dimensions of the semiconductor core directly modifies the LDOS, and thus controls the radiative emission rate. Furthermore, we take advantage of the modest quality factors in these plasmonic nanostructures ($Q < 50$) to achieve band-to-band spontaneous emission enhancement. We use the boundary element method (BEM) to investigate the LDOS in these structures [62, 85], choosing dimensions of the resonator such that the lowest-order longitudinal resonance overlaps with the emission wavelength of the active material. For this mode, we determine the LDOS, effective mode volume (V_{eff}), quality factor (Q), and enhancements in the total and radiative decay rates (Γ_{tot} and Γ_{rad} , respectively, normalized to decay in vacuum, Γ_0), and the corresponding quantum efficiency $\eta = \Gamma_{\text{rad}}/\Gamma_{\text{tot}}$.

In the BEM, calculations are performed in the frequency domain with the electromagnetic field in each homogeneous region expressed as a function of auxiliary boundary charges and currents. After applying boundary conditions, a set of linear integrals is obtained and solved by discretization. The axial symmetry of core-shell nanowire

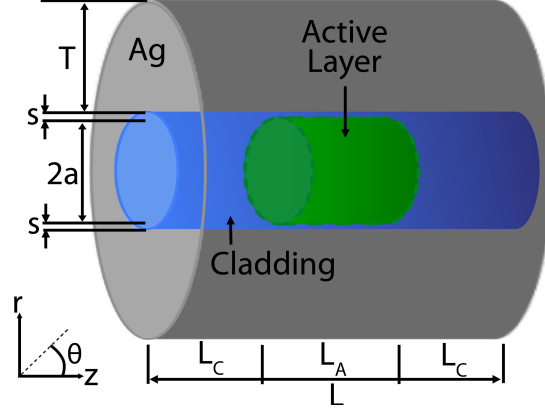


Figure 6.1. Schematic of a plasmonic core-shell nanoresonator. The nanowire core consists of a III-V semiconductor active layer (length L_A and radius a) clad with a wider band-gap III-V semiconductor (segment lengths L_C and spacer thickness s) and coated with Ag (thickness T and total length $L = 2L_C + L_A$).

resonators allows decomposition of the fields into uncoupled azimuthal components m with angular dependence $e^{im\phi}$. This results in an essentially one-dimensional field calculation that is solved with great accuracy. Converged results are found for $m_{\max} = 1$, using values of m defined by

$$m = -m_{\max}, -m_{\max} + 1, \dots, m_{\max} - 1, m_{\max}. \quad (6.1)$$

The dielectric functions of the core and cladding materials are input using tabulated data [34, 86, 87, 88, 89]. Resonant modes are determined by calculating the LDOS ρ for a dipole emitter oriented along a radial direction using the relation

$$\rho = \frac{\omega^2 n}{3\pi^2 c^3} + \frac{1}{2\pi^2 \omega} \text{Im}[E_{\text{ind}}/D], \quad (6.2)$$

where ω is the resonance frequency, c is the speed of light in vacuum, n is the refractive index of the active semiconductor, D is the dipole strength, and E_{ind} is the contribution to the electric field due to scattering at the interfaces and projected along the direction of polarization. The resonance quality factor, Q , is determined

by fitting a Lorentzian lineshape to a plot of ρ vs. ω , and

$$Q = \frac{\omega}{\Delta\omega}, \quad (6.3)$$

where $\Delta\omega$ is the full width at half maximum.

In addition to calculating the LDOS, we determine the spatial near-field electric field intensity (NF $|\mathbf{E}|^2$) profiles of each mode by using plane-wave excitation incident at $\theta = 0^\circ$, polarized along an arbitrary radial direction (see Figure 6.1). The effective mode volume, V_{eff} , is defined as a cylinder with length L_{eff} and radius a_{eff} given by the $1/e$ decay distance of the peak field intensity inside the semiconductor core as $V_{\text{eff}} = \pi a_{\text{eff}}^2 L_{\text{eff}}$. To determine what portion of the decay contributes to radiative emission and absorption, we assume that the compound semiconductor active material has unit internal quantum efficiency in homogeneous bulk materials [90] and calculate the enhancements in the total and radiative decay rates normalized to Γ_0 , the decay rate in vacuum, given by

$$\Gamma_0 = \frac{4}{3} \frac{|D|^2}{\hbar} \left(\frac{\omega}{c} \right)^3. \quad (6.4)$$

The total decay rate, Γ_{tot} , is related to the LDOS ρ as

$$\Gamma_{\text{tot}} = \frac{4\pi^2\omega|D|^2}{\hbar} \rho. \quad (6.5)$$

Finally, the radiative decay rate, Γ_{rad} , is calculated by integrating the far-field Poynting vector for a dipole source (polarized along r) located in the center of the resonator core.

6.3 Modes of Active Core-Shell Nanowire Resonators

Detailed results are presented for three resonators, each composed of a different III-V compound semiconductor active emitter (GaAs, $\text{Al}_{0.42}\text{Ga}_{0.58}\text{As}$, and $\text{In}_{0.15}\text{Ga}_{0.85}\text{N}$).

6.3.1 GaAs-In_{0.51}Ga_{0.49}P-Ag Resonator

We first consider GaAs as an active material with a band gap (emission wavelength) $E_g = 1.424$ eV ($\lambda = 870$ nm), clad with In_{0.51}Ga_{0.49}P, which is lattice matched to GaAs. A thin In_{0.51}Ga_{0.49}P spacer layer is located between the GaAs active region and Ag coating to prevent quenching of excitons located near the metal/semiconductor interface. The lowest-order longitudinal resonance occurs at the proper wavelength for a resonator with dimensions $a = 36$ nm, $s = 6$ nm, $L_A = 100$ nm, $L_C = 25$ nm, and $T = 100$ nm. Figure 6.2 shows contour plots of the LDOS and NF $|\mathbf{E}|^2$ for plane-wave excitation at $\theta = 0^\circ$ as a function of both wavelength and distance along the z -axis at a constant radial position of $r = 5$ nm. It is clear from Figure 6.2 that the mode at $\lambda = 870$ nm has LDOS peaked in the GaAs region of the core. Additional modes are supported at shorter wavelengths, but these do not overlap with the emission wavelength of the active material and do not have the proper symmetry to support large decay rate enhancements. Furthermore, we see from Figure 6.2 that plane-wave excitation at $\lambda = 870$ nm excites the same mode profile, with high fields localized inside the GaAs region. The modes at shorter wavelengths are not excited here because of symmetry.

We also calculate two-dimensional cross sections of the LDOS and NF $|\mathbf{E}|^2$ for the mode at $\lambda = 870$ nm. The LDOS in Figure 6.3b is calculated in the semiconductor core, and illustrates that indeed high LDOS is peaked inside the GaAs region. High intensity is also localized in the thin spacer layer. Plane wave excitation at $\lambda = 870$ nm allows investigation of the electric field localization, and high confinement of the fields in both the radial and longitudinal directions is demonstrated in the two-dimensional NF $|\mathbf{E}|^2$ cross section of Figure 6.3c. The regions of high field intensity in the core correlate to regions of high LDOS, and thus also to large enhancements in the total decay rate. This mode has a moderate quality factor of 45 and an effective mode volume $V_{\text{eff}} = 0.070(\lambda/n)^3$, for $Q/V_{\text{eff}} = 645(\lambda/n)^{-3}$. The radiative decay rate enhancement is calculated for a dipole located in the center of the resonator polarized along the r -direction, and we find $\Gamma_{\text{tot}}/\Gamma_0 = 223$, $\Gamma_{\text{rad}}/\Gamma_0 = 128$, and $\eta = 0.57$.

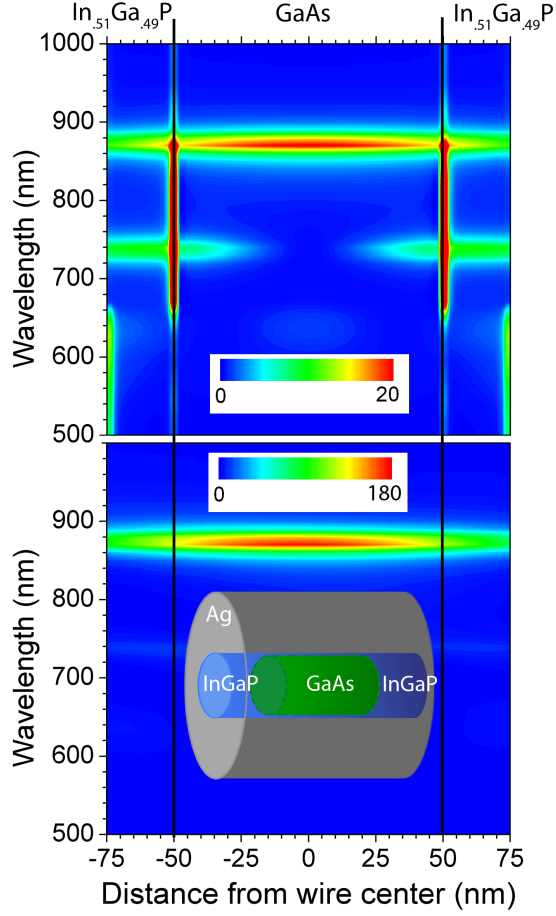


Figure 6.2. Resonant modes for a structure with GaAs active layer ($a = 36$ nm, $L_A = 100$ nm), $\text{In}_{0.51}\text{Ga}_{0.49}\text{P}$ cladding ($s = 5$ nm, $L_C = 25$ nm), and Ag coating thickness $T = 100$ nm. The LDOS (top) and NF $|\mathbf{E}|^2$ (bottom) are calculated at a constant radial position of $r = 5$ nm from the center of the resonator core and along the length of the wire, at wavelengths between $\lambda = 500$ and 1000 nm. The values of LDOS reported are normalized to the LDOS in vacuum. The structure is shown schematically in the inset.

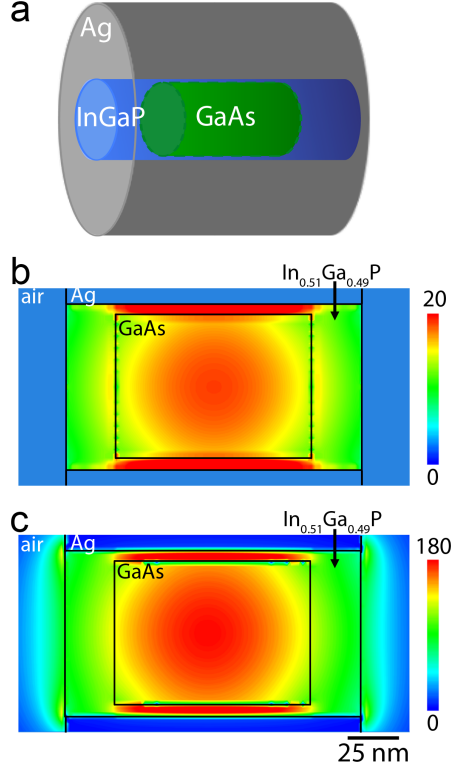


Figure 6.3. (a) Schematic of a GaAs-InGaP-Ag core-shell nanowire resonator with GaAs active layer ($a = 36$ nm, $L_A = 100$ nm), $\text{In}_{0.51}\text{Ga}_{0.49}\text{P}$ cladding ($s = 5$ nm, $L_C = 25$ nm), and Ag coating thickness $T = 100$ nm. Two-dimensional profiles of the (b) LDOS at $\lambda = 870$ nm and (c) NF $|\mathbf{E}|^2$ cross section for plane-wave excitation at $\lambda = 870$ nm ($\theta = 0^\circ$), the emission wavelength of GaAs, show that both high LDOS and high electric fields are concentrated inside the GaAs active region, in a mode that is highly confined within the semiconductor core.

6.3.2 $\text{Al}_{0.42}\text{Ga}_{0.58}\text{As}$ - $\text{Al}_{0.70}\text{Ga}_{0.30}\text{As}$ -Ag Resonator

To investigate a smaller structure with modes at shorter wavelengths, we choose $\text{Al}_{0.42}\text{Ga}_{0.58}\text{As}$ as the active material. This alloy has $E_g = 1.95$ eV, emitting at a wavelength of $\lambda = 637$ nm. A ternary alloy with higher Al content, $\text{Al}_{0.70}\text{Ga}_{0.30}\text{As}$, is chosen for the cladding and spacer material, which is an indirect band-gap semiconductor with $E_g = 2.07$ eV. A core-shell nanowire resonator composed of these materials with dimensions $a = 14$ nm, $s = 5$ nm, $L_A = 20$ nm, $L_C = 30$ nm, and $T = 100$ nm has the lowest order longitudinal resonance at $\lambda = 637$ nm. The LDOS and NF $|\mathbf{E}|^2$ mode profiles along the length of the resonator, calculated at a radial position of $r = 5$ nm from the center of the core, are shown in Figure 6.4. Note the twofold increase in LDOS of the lowest order mode as compared to the larger GaAs structure. A plane wave at $\lambda = 637$ nm also excites this mode with a longitudinal profile that matches the LDOS.

The two-dimensional LDOS and NF $|\mathbf{E}|^2$ profiles for the mode at $\lambda = 637$ nm are shown in Figure 6.5. The LDOS profile shows that high LDOS can be found throughout the core, suggesting that the total decay rate will be enhanced for dipole emitters located throughout the semiconductor. The NF $|\mathbf{E}|^2$ profile in demonstrates that even in this smaller structure, fields are highly confined in the semiconductor core with minimal field penetration into the surrounding medium. This mode has $Q = 30$, $V_{\text{eff}} = 0.021(\lambda/n)^3$, and $Q/V_{\text{eff}} = 1435(\lambda/n)^{-3}$, with decay rate enhancement $\Gamma_{\text{tot}}/\Gamma_0 = 460$, $\Gamma_{\text{rad}}/\Gamma_0 = 280$, and $\eta = 0.60$. Comparing these results to the GaAs resonator, we see that the smaller resonator continues to exhibit high modal confinement with an effective mode volume approximately equal to the physical volume of the semiconductor core, and that the lowest-order longitudinal resonance does not sustain much loss in quality factor with decreased dimensions. Thus, the figure of merit Q/V_{eff} more than doubles in this smaller resonator relative to the first example using GaAs, described above.

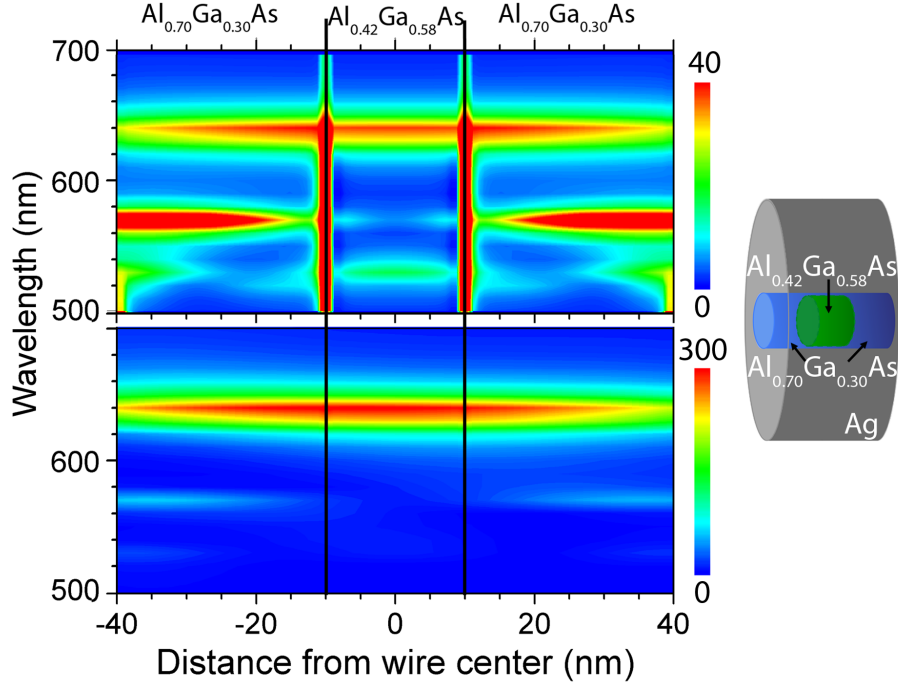


Figure 6.4. LDOS (top) and NF $|\mathbf{E}|^2$ (bottom) profiles showing the resonant modes for a structure with $\text{Al}_{0.42}\text{Ga}_{0.58}\text{As}$ active layer ($a = 15$ nm, $L_A = 20$ nm), $\text{Al}_{0.70}\text{Ga}_{0.30}\text{As}$ cladding ($s = 5$ nm, $L_C = 30$ nm), and Ag coating ($T = 100$ nm). The LDOS and NF $|\mathbf{E}|^2$ are calculated at a constant radial position of $r = 5$ nm from the center of the resonator core, and reported values of LDOS and NF $|\mathbf{E}|^2$ are normalized to the LDOS in vacuum and fields of the incident plane-wave source, respectively.

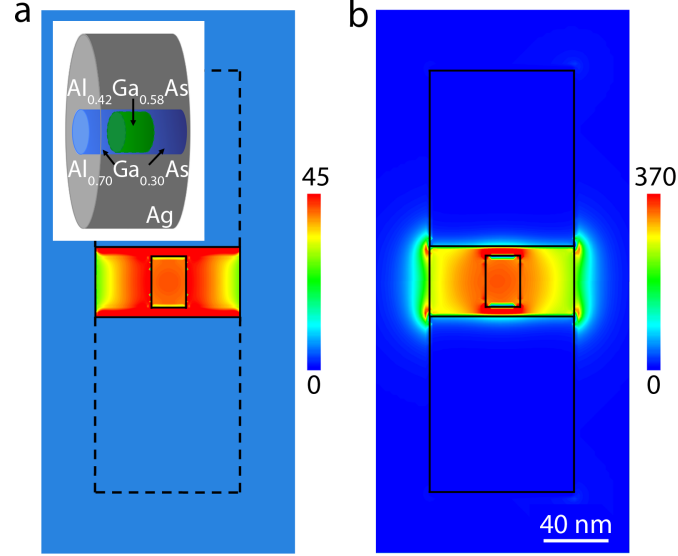


Figure 6.5. Two-dimensional (a) LDOS and (b) NF $|\mathbf{E}|^2$ cross sections of a core-shell nanowire resonator with $\text{Al}_{0.42}\text{Ga}_{0.58}\text{As}$ active layer ($a = 15$ nm, $L_A = 20$ nm), $\text{Al}_{0.70}\text{Ga}_{0.30}\text{As}$ cladding ($s = 5$ nm, $L_C = 30$ nm), and Ag coating ($T = 100$ nm). The LDOS is calculated at $\lambda = 637$ nm, the emission wavelength of the $\text{Al}_{0.42}\text{Ga}_{0.58}\text{As}$. The NF $|\mathbf{E}|^2$ cross section is calculated for plane-wave excitation at $\lambda = 637$ nm ($\theta = 0^\circ$).

6.3.3 $\text{In}_{0.15}\text{Ga}_{0.85}\text{N}$ -GaN-Ag Resonator

Next, we consider as our active layer a 2 nm $\text{In}_{0.15}\text{Ga}_{0.85}\text{N}$ single quantum well (SQW), with GaN as the cladding. Excitons in the $\text{In}_{0.15}\text{Ga}_{0.85}\text{N}$ are highly localized, and therefore an explicit spacer layer is not modeled in this structure. The $\text{In}_{0.15}\text{Ga}_{0.85}\text{N}$ quantum well emits at $\lambda = 440$ nm, and the resonator with the lowest-order longitudinal resonance at this wavelength has dimensions of $a = 5$ nm, $L_A = 2$ nm, $L_C = 10$ nm, and $T = 50$ nm. In this deeply subwavelength resonator, only extremely evanescent modes are supported. The LDOS and NF $|\mathbf{E}|^2$ for plane-wave excitation at $\theta = 0^\circ$ along the length of the wire are shown in Figure 6.6. At $\lambda = 440$ nm, the peak LDOS within the $\text{In}_{0.15}\text{Ga}_{0.85}\text{N}$ SQW has a peak value of 900, more than twenty times the peak LDOS of the GaAs and $\text{Al}_{0.42}\text{Ga}_{0.58}\text{As}$ resonators.

The two-dimensional LDOS and NF $|\mathbf{E}|^2$ cross sections in Figure 6.7 illustrate the high level of confinement within the core of this deeply subwavelength structure. Although the highest LDOS is seen at the semiconductor/metal interface, $\text{LDOS} > 1000$ is seen throughout the InGaN SQW. Furthermore, a peak electric field intensity of 3000 times larger than the incident plane wave is seen in Figure 6.7. This highest LDOS and NF $|\mathbf{E}|^2$ of the three resonators studied in detail here is achieved with the smallest resonator volume. We calculate $Q = 32$ and $V_{\text{eff}} = 4.3 \times 10^{-4}(\lambda/n)^3$, and find the highest Q/V_{eff} in this ultra-small resonator at $7.4 \times 10^4(\lambda/n)^{-3}$. Dramatic decay rate enhancements are found for this ultra-small structure, with $\Gamma_{\text{tot}}/\Gamma_0 = 8200$, $\Gamma_{\text{rad}}/\Gamma_0 = 3500$, and $\eta = 0.43$, which exceeds the radiative decay rate enhancements reported for metal nanoparticle structures [91]. This demonstrates that upon the transition from subwavelength resonators that support eigenmodes with sizable retardation effects to ultra-small resonators that support highly evanescent modes of a non-retarded nature, plasmonic core-shell nanowire resonators with dimensions on the order of $\lambda/50$ are able to strongly confine modes within the semiconductor core and to achieve dramatic enhancements in the radiative emission rate.

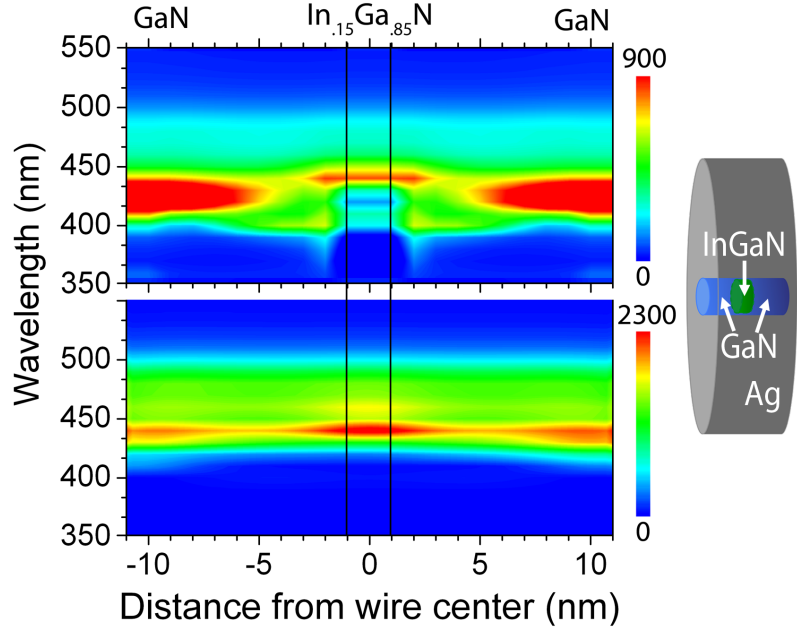


Figure 6.6. (top) LDOS (normalized to LDOS in vacuum) and (bottom) NF $|\mathbf{E}|^2$ for plane-wave excitation at $\lambda = 440$ nm, $\theta = 0^\circ$ (normalized to incident source) versus wavelength for a structure with $\text{In}_{0.15}\text{Ga}_{0.85}\text{N}$ active layer ($a = 5$ nm, $L_A = 2$ nm), GaN cladding ($L_C = 10$ nm and no spacer layer), and Ag coating ($T = 50$ nm). LDOS and NF $|\mathbf{E}|^2$ are calculated at a radial position of $r = 1$ nm from the center of the resonator core and along the longitudinal axis. Schematic of this structure is shown on the right.

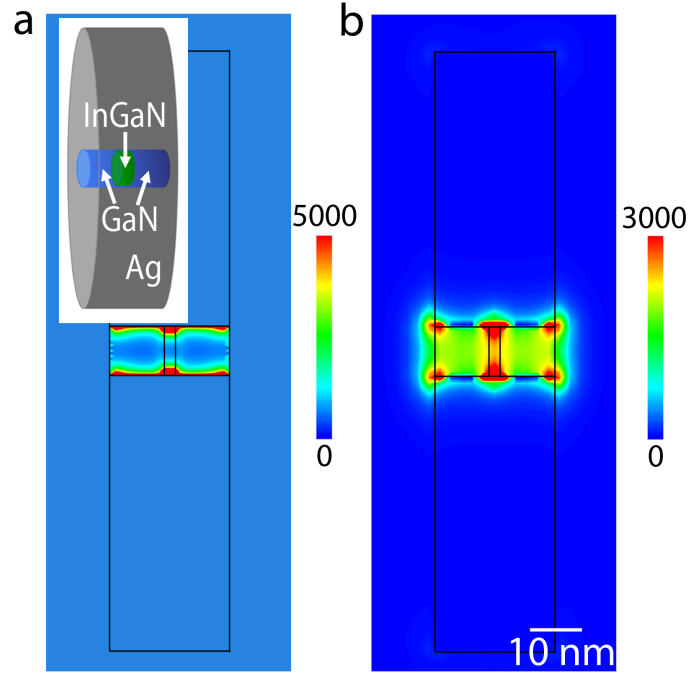


Figure 6.7. Cross-sectional (a) LDOS and (b) NF $|E|^2$ profile for a structure with $\text{In}_{0.15}\text{Ga}_{0.85}\text{N}$ active layer ($a = 5$ nm, $L_A = 2$ nm), GaN cladding ($L_C = 10$ nm and no spacer layer), and Ag coating ($T = 50$ nm). The LDOS is calculated at $\lambda = 440$ nm, the emission wavelength of the $\text{In}_{0.15}\text{Ga}_{0.85}\text{N}$ single quantum well. The NF $|E|^2$ is calculated for plane-wave excitation at $\lambda = 440$ nm ($\theta = 0^\circ$).

6.4 Enhanced Radiative Decay

The total decay rate enhancements and corresponding quantum efficiencies are plotted in Figure 6.8. Peaks in the plot of $\Gamma_{\text{tot}}/\Gamma_0$ versus wavelength correspond to the resonant modes illustrated in the LDOS plots of Figures 6.2, 6.4, and 6.6. The largest decay rate enhancements are seen for the $\lambda = 440$ nm mode of the ultra-small $\text{In}_{0.15}\text{Ga}_{0.85}\text{N}$ resonator, although significant enhancements are also observed for the GaAs and $\text{Al}_{0.42}\text{Ga}_{0.58}\text{As}$ resonators. Additionally, the quantum efficiencies η at the wavelengths of interest are $>50\%$ for these two resonators. Remarkably, even the smallest resonator ($\text{In}_{0.15}\text{Ga}_{0.85}\text{N}$ SQW) maintains a reasonable quantum efficiency of $>40\%$, suggesting that a large portion of the enhanced decay rate correlates to observable photons. The colored shaded regions on the graph correspond to a typical LED bandwidth centered at the emission wavelength of the active material, and because of the moderate quality factors in these plasmonic resonators, the rate of spontaneous emission is enhanced significantly throughout the entire band.

Finally, we also calculate the polarization dependence of the far-field (FF) radiation at the emission wavelength of each III-V semiconductor plasmonic core-shell nanowire resonators, and compare that to the emission polarization from an uncoated wire (GaAs active region with $a = 36$ nm, $L_A = 100$ nm, $\text{In}_{0.51}\text{Ga}_{0.49}\text{P}$ cladding and spacer with $s = 6$ nm and $L_C = 25$ nm, and no Ag coating). The polar plot is seen in Figure 6.9 for an observer looking down a radial axis. The FF radiation is determined for dipole excitation in the center of the resonator core, and the emission is isotropically averaged for all three dipole orientations (x , y , and z). The uncoated wire has a dipolar emission pattern oriented transverse to the longitudinal axis of the nanowire. Although not plotted here, the uncoated $\text{In}_{0.15}\text{Ga}_{0.85}\text{N}/\text{GaN}$ and $\text{Al}_{0.42}\text{Ga}_{0.58}\text{As}/\text{Al}_{0.70}\text{Ga}_{0.30}\text{As}$ wires show the same dipolar radiation pattern. With the Ag coating, all three of the resonators have a strongly modified emission polarization that is now oriented parallel to the longitudinal axis of the resonator. Dielectric materials tend to trap electromagnetic fields, so the z dipole in the uncoated GaAs nanowire is more efficient at polarizing the dielectric, and therefore emission is peaked

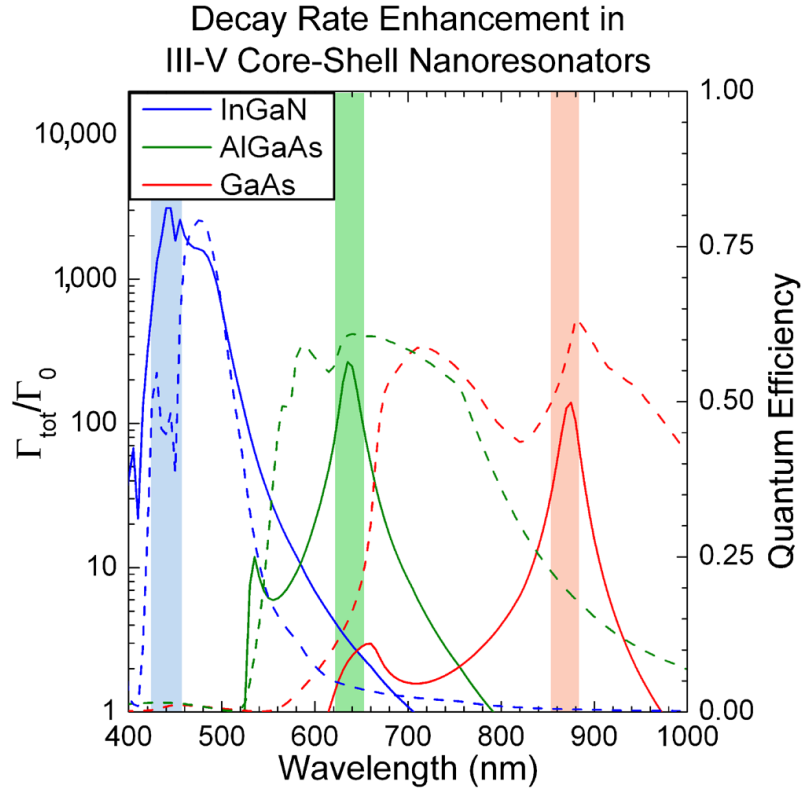


Figure 6.8. Total decay rate enhancement (solid) and quantum efficiencies (dashed) as a function of wavelength for the three different III-V core-shell nanoresonators. Colored shaded regions indicate typical spectral width of LED emission.

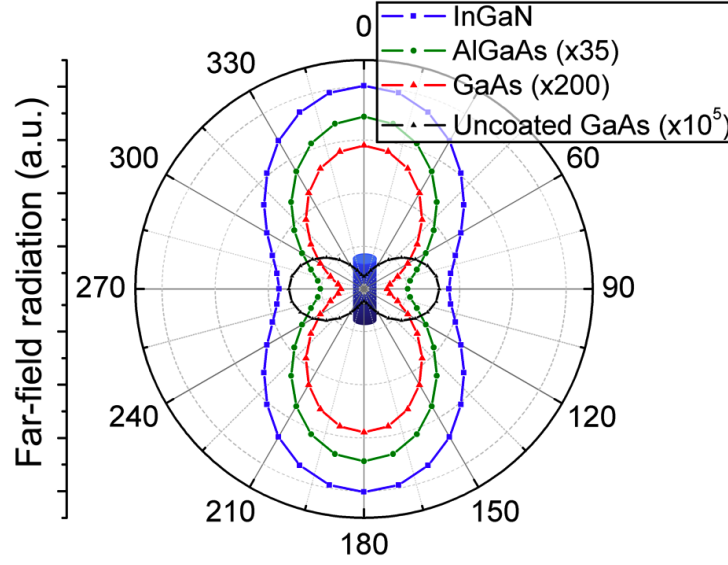


Figure 6.9. Polar plot of far-field radiation from dipole excitation of the same three core-shell nanoresonators (AlGaAs scaled $\times 35$, GaAs scaled $\times 200$) and in black a bare (uncoated, no Ag) GaAs/ $\text{In}_{0.51}\text{Ga}_{0.49}\text{P}$ nanowire (scaled $\times 10^5$). The Ag coating modifies both the intensity and direction of the far-field emission.

toward $\theta = 90^\circ$. In contrast, the metal coating quenches the z dipole, whereas radial dipoles couple naturally to modes of the metal-dielectric interface and dominate the resulting polar emission. Thus, the plasmonic coating modifies not only the rate of spontaneous emission but also the direction of far-field radiation.

6.5 Chapter Summary

In summary, we have introduced the III-V semiconductor plasmonic core-shell nanowire resonator geometry and shown that it is suitable for achieving dramatic enhancements in the rate of spontaneous decay of a variety of III-V materials, namely GaAs, $\text{Al}_{0.42}\text{Ga}_{0.58}\text{As}$, and $\text{In}_{0.15}\text{Ga}_{0.85}\text{N}$. In all three structures, the dimensions are chosen such that the lowest-order longitudinal resonance occurs at the band-edge emission wavelength of the active material, and the electric fields are highly confined within

Table 6.1. Summary of Q/V and decay rate enhancements in III-V semiconductor plasmonic core-shell nanowire resonators

active material	GaAs	Al _{0.42} Ga _{0.58} As	In _{0.15} Ga _{0.85} N
radius a (nm)	36	14	5
length L_A (nm)	100 (GaAs)	20 (Al _{0.42} Ga _{0.58} As)	2 (In _{0.15} Ga _{0.85} N)
length L_C (nm)	25 (In _{0.51} Ga _{0.49} P)	30 (Al _{0.70} Ga _{0.30} As)	10 (GaN)
spacer s (nm)	6 (In _{0.51} Ga _{0.49} P)	4 (Al _{0.70} Ga _{0.30} As)	0
Ag thickness T (nm)	100	100	50
λ (nm)	870	637	440
V_{eff}	$0.070(\lambda/n)^3$	$0.021(\lambda/n)^3$	$4.3 \times 10^{-4}(\lambda/n)^3$
Q	45	30	32
Q/V_{eff}	$645(\lambda/n)^{-3}$	$1435(\lambda/n)^{-3}$	$74000(\lambda/n)^{-3}$
$\Gamma_{\text{rad}}/\Gamma_0$	128	280	8,200
$\Gamma_{\text{tot}}/\Gamma_0$	223	460	3,500
η	57%	60%	43%

the resonator core. The increased LDOS due to the plasmonic coating contributes directly to enhanced spontaneous emission, and total decay rate enhancements of >8000 with quantum efficiency of $>40\%$ are observed for a structure with dimensions on the order of $\lambda/50$. Additionally, $Q/V > 10^4(\lambda/n)^{-3}$ was calculated, a value competitive with conventional high-Q dielectric microcavities. The numerical results are summarized in Table 6.1. We anticipate that as we continue to shrink resonator dimensions and incorporate new active materials that emit near the surface plasmon resonance, even higher LDOS and radiative decay rate enhancements will be achievable. This work demonstrates that III-V semiconductor plasmonic core-shell nanoresonators are a promising design for fast, bright, nanoscale, and perhaps even directional on-chip light sources.

Chapter 7

Summary and Outlook

The field of plasmonics has undergone significant growth in recent years, primarily due to advances in nanofabrication techniques and full-field electromagnetic simulation. We are now able to not only investigate optics at the nanoscale, but to precisely control and predict these phenomena in a wide array of architectures. This thesis has been devoted to the study of light emission in a variety of plasmonic geometries, illustrating new methods of exciting and manipulating light in complex nanocavities.

In the early chapters, we demonstrated that cathodoluminescence imaging spectroscopy is a powerful tool for investigating metallic films and nanostructures. The light emission resulting from electron beam excitation was used to determine the propagation distance of near-resonance surface plasmons, and distances as short as 400 nm were measured on Ag films. We also examined a metal-coated semiconductor nanowire with this technique, and were able to excite localized resonances in the metal coating, as well as bright emission from the semiconductor nanowire. Modes of a more complex geometry, the annular nanoresonator, were also investigated with spectrally resolved cathodoluminescence. We mapped out the spatial profiles of annular nanoresonator modes in both Ag and Au structures with extremely high spatial resolution. Supported by full-field simulation, our observations led to the conclusion that CL emission in a particular resonator mode is brightest for electron beam excitation in a position of high field intensity.

We then chose to study a specific plasmonic nanocavity, the core-shell nanowire resonator, with a number of different semiconductor core materials and an optically thick Ag coating. Theoretical calculations of the Si-Ag geometry proved that the LDOS could be carefully tuned by adjusting the dimensions of the resonator, and that

the highest LDOS is achieved in the smallest structures. Remarkably, a Si-Ag core-shell nanowire resonator with dimensions on the order of $\lambda/50$ still sustained modes with $Q > 25$, permitting dramatic enhancements in the total and radiative decay rates. Further, we presented two routes of fabricating the Si-Ag core-shell nanowire resonators, one relying on top-down lithography and RIE etching techniques, and the other based on CVD growth, oxidation, and wet chemical etching. In both cases, Si cores with diameters of <50 nm were achieved, and fully fabricated resonators were characterized with dark-field optical spectroscopy. Switching to III-V semiconductor core materials, we illustrated that active plasmonic core-shell nanowire resonators are a promising design for fast, bright, and directional on-chip light sources. Structures with GaAs, AlGaAs, and InGaN active emitters were chosen, and all exhibited extremely high field confinement for deeply subwavelength mode volumes. Again here, the smallest structure (InGaN) provided the most dramatic decay rate enhancements of more than 8000 times with quantum efficiency of $>40\%$.

One area of ongoing work involves designing metal nanostructures to enhance the rate of spontaneous emission from GaAs nanowires, inspired by the theoretical results of Chapter 6. Our preliminary experiments include dropcasting high quantum efficiency GaAs NWs grown by molecular beam epitaxy [92] on a variety of substrates (Si, Ag, and Ag coated with a thin Cr layer) and comparing the GaAs PL intensity and lifetime decay traces. Single nanowire spectroscopy is performed using the setup shown in Figure 7.1, with a picosecond supercontinuum laser source operating at 40 MHz passed through filters for excitation between 550 and 750 nm. The laser is sent through an inverted optical microscope with a $100\times$ objective (0.9 NA) and focused to a $15\text{ }\mu\text{m}$ spot on the nanowire. In the detection path, a CCD and a single photon avalanche diode (SPAD) permit collection of single nanowire PL spectra and PL lifetime decay traces, respectively. Figure 7.2a shows a TEM image of an individual GaAs NW approximately $15\text{ }\mu\text{m}$ long, and with a diameter that tapers from 150 to 80 nm. The NW is composed of a GaAs p-i-n radial junction and thin $\text{Al}_{0.4}\text{Ga}_{0.6}\text{As}$ /GaAs cap 10 nm thick. Once dropcast onto the various substrates, PL spectra (Figure 7.2c) and PL lifetime decays (Figure 7.2d) are measured for a

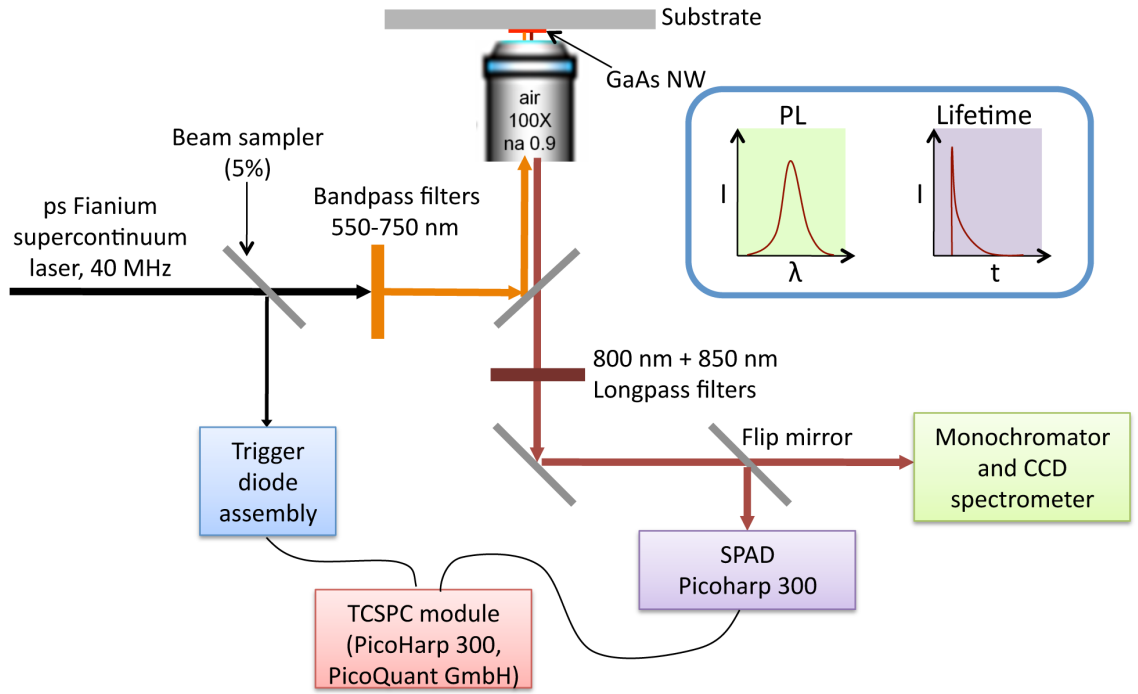


Figure 7.1. Schematic of single nanostructure PL and lifetime decay experimental setup. A picosecond supercontinuum laser source operating at a fixed repetition rate of 40 MHz is sent through bandpass filters at wavelengths of 550–750 nm, into an inverted optical microscope operating in reflection equipped with a 100 \times objective (NA 0.9), and focused onto a single nanostructure. The emitted PL is sent through a pair of longpass filters (800 and 850 nm) and then, via a flip mirror assembly, into either a monochromator and CCD spectrometer for collection of PL spectra, or into a single photon avalanche diode (SPAD) detector and time-correlated single photon counting (TCSPC) module for lifetime measurements. A beam sampler (5%) sends a portion of the incident laser light into a trigger diode to sync the source and detector pulses.

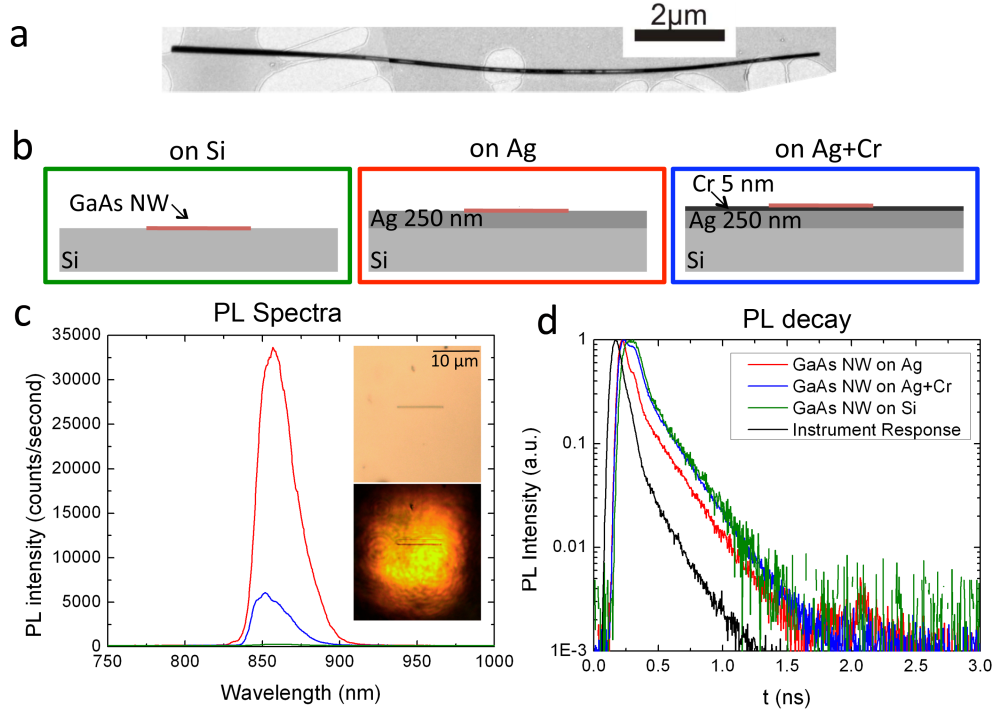


Figure 7.2. (a) TEM image of a single GaAs NW 15 μm long and tapered from 150 to 80 nm diameter. The nanowire core consists of a GaAs p-i-n radial junction clad with 8 nm $\text{Al}_{0.4}\text{Ga}_{0.6}\text{As}$ and a 2 nm GaAs cap. (b) Schematics of GaAs NWs dropcast on three different substrates: Si, Ag (250 nm) on Si, and Ag (250 nm) + Cr (5 nm) on Si. (c) PL intensity and (d) PL lifetime decay for single GaAs NWs on each substrate: Si (green), Ag (red), and Ag+Cr (blue), with the instrument response for decay measurements plotted in black. The PL spectra show a 5-fold enhancement in PL intensity for a NW on Ag when compared to a NW on Ag+Cr, and the PL decay shows a $3\times$ decay rate enhancement for a NW on Ag compared to NWs on bare Si and Ag+Cr films. Insets in (c): (top) Bright-field reflected light image, and (bottom) laser spot focused on a single nanowire.

number of NWs. Because of absorption in the Si at both the pump wavelengths and at the PL emission wavelength, the emission intensity for the GaAs NW on Si is too low to plot alongside the others in Figure 7.2c. The PL spectra for GaAs NWs on the other two substrates, however, show a $5\times$ enhancement in the emission intensity for a NW on Ag when compared to a NW on Ag+Cr. We expect the thin Cr layer to damp SPs while not significantly diminishing the reflectivity of the Ag, and therefore attribute the PL intensity enhancement to coupling into SPs. Furthermore, the PL decay traces in Figure 7.2d illustrate shorter PL lifetimes τ for a GaAs NW on Ag ($\tau = 43$ ps) compared to NWs on Si and Ag+Cr ($\tau = 125$ ps). These results encourage further experimental investigation of additional plasmonic nanostructures for enhancing spontaneous emission, a variety of which can be easily fabricated using FIB milling of metal films. We are currently pursuing this work with a goal of observing $>100\times$ enhancement in the emission rate of GaAs NWs.

Overall, this thesis has demonstrated that plasmonics enables truly nanophotonic technologies and provides a means of manipulating light at the nanoscale. The relatively young field of plasmonics has already seen rapid progression in the miniaturization of traditional optical components such as waveguides and resonators, achieved by judiciously designing metallodielectric structures that exhibit extremely high and localized field intensities and extremely short wavelengths. Though these early prototype devices are impressive in their own right, the true potential of plasmonics will be realized by exploiting the hybrid electronic/photonic characteristics of surface plasmons to create a new class of applications. From investigations of cathodoluminescence emission in plasmonic nanostructures, one can envision the development of an electrical surface plasmon source that could be integrated for chip-based nanophotonic networks or sensors. New plasmonic nanocavity designs that support dramatic spontaneous emission enhancements may enable nanoscale LEDs that are brighter and faster than chip-based laser sources. There are, of course, myriad opportunities, with the only limits being our imagination and determination to realize the promise of plasmonics.

Appendix A

Boundary Element Method Calculations of LDOS and Decay Rates

A.1 Decay Rates in Atomic Units

This appendix provides a brief tutorial for BEM calculations of the total and radiative decay rates, including a sample command file and material data file for BEMAX (program for structures with axial symmetry), and intended to supplement the internal help files that accompany the BEMAX program. As described in Chapters 4 and 6, the total decay rate is proportional to the LDOS, and the radiative decay rate is determined from the far-field radiation [85]. All calculations within the BEM program use atomic units with standard physical quantities defined as follows:

$$\hbar = m_e = e = 4\pi\epsilon_0 = 1 \quad (\text{A.1a})$$

$$c = 137.036 \quad (\text{A.1b})$$

$$\lambda = \frac{10 \cdot \lambda[\text{nm}]}{0.52918} \quad (\text{A.1c})$$

$$\omega = \frac{E[\text{eV}]}{27.211} = \frac{1240}{27.211 \cdot \lambda[\text{nm}]} \quad (\text{A.1d})$$

The BEM calculations of the local density of optical states ρ output a value for each orientation (x , y , and z) and a total LDOS, all normalized ρ_0 , the LDOS in a homogeneous region of refractive index n , given by

$$\rho_0 = \frac{\omega^2 n}{\pi^2 c^3} \quad (\text{A.2})$$

in atomic units. To distinguish, we define LDOS_x as the value output from the BEM program for the x orientation (command `calc LDOS`), and ρ_x the unnormalized value, such that

$$\text{LDOS}_x = \frac{\rho_x}{\rho_0}. \quad (\text{A.3})$$

Now, we are equipped to calculate decay rates from BEM output. This thesis reports total and radiative decay rates normalized to decay in vacuum, Γ_0 ,

$$\Gamma_0 = 4\pi^2 \frac{\omega}{\hbar} \frac{\rho_0}{3} |D|^2, \quad (\text{A.4})$$

which in atomic units becomes

$$\Gamma_0 = \frac{4}{3} \left(\frac{\omega}{c} \right)^3. \quad (\text{A.5})$$

Similarly, the total decay rate Γ_{tot} is given by

$$\Gamma_{\text{tot}} = \frac{4\pi^2 \omega}{\hbar} |D|^2 \rho_x, \quad (\text{A.6})$$

or in atomic units,

$$\Gamma_{\text{tot}} = 4 \left(\frac{\omega}{c} \right)^3 n \text{LDOS}_x. \quad (\text{A.7})$$

The radiative decay rate is calculated by integrating the far-field Poynting vector for a dipole source, given by

$$\Gamma_{\text{rad}} = \frac{c}{2\pi\omega} \int f^2. \quad (\text{A.8})$$

In this case, $\int f^2$ is the output from the BEM command `calc total-far-field`.

In summary, the quantities from BEM commands can be used directly to calculate decay rates using (A.7) and (A.8), and properly normalized by dividing by (A.5). The following pages provide a sample BEMAX input file for determining the decay rates in a Si-Ag core-shell nanowire resonator, as well as a sample material file for Ag with the dielectric constants of Johnson and Christy [34].

A.2 Example BEM Input File

CoreShell_SiAg_a25L150.bem

```
mmax 3
    // calculations performed for m=-3,-2,-1,0,1,2,3

epsilon 2 Ag // calls material file Ag.eps
epsilon 3 Si // calls material file Si.eps
            // material 1 is always air (n=1)
photon-wavelength 500 1000 101
    // defines range of wavelengths for calculations
    // (in nm) and number of wavelengths used
    // for calculation (101)

// Define structure
L=150 // wire length (nm)
a=25  // core radius
C=100 // coating thickness
n1=25 // number of parameterization points, radius
n2=50 // number of param. points, coating
n3=150 // number of param. points, length

// Structure made of straight line segments
// from (x1,z1) to (x2, z2) with material
// mu1 to left and mu2 to right
// add-segment command format:
    // mu1, mu2, x1, z1, x2, z2, # param. points
add-segment 3 1 0 0 a 0 n1
add-segment 1 3 0 L a L n1
add-segment 2 1 a 0 a+C 0 n2
add-segment 1 2 a L a+C L n2
add-segment 3 2 a 0 a L n3
add-segment 2 1 a+C 0 a+C L n3

begin-calculation // begins calculation loop

// Calculate NF intensity for plane-wave excitation
// at all wavelengths

grid 5 5 1 0 0 1 0 150 76
    // grid for NF E2 intensity along z-axis for x=5:
    // command format is grid x1 x2 nx y1 y2 ny z1 z2 nz
```

```

incident-plane-wave 0 0 0 0
// incident plane wave at theta=0

calc E2-near-field nf05th=0.dat
// output will appear in this file

grid 5 5 1 0 0 1 0 150 76

incident-plane-wave 90 0 0 0
// incident plane wave at theta=90

calc E2-near-field nf05th=90.dat
// output will appear in this file

// Components required to calculate decay rates

// First position
z=15 R=5
grid R R 1 0 0 1 z z 1
// single point at (R,z)
calc LDOS LDOS_r5z15.dat
// LDOS used to find total decay rate

electric-dipole R z 1 0 0 0 0 0
// dipole source oriented along x at position (R,z)
calc total-far-field totalff_r5z1_px.dat
// FF used to find radiative decay rate

// Second position
z=75 R=5
grid R R 1 0 0 1 z z 1
// single point at (R,z)
calc LDOS LDOS_r5z75.dat
// LDOS used to find total decay rate

electric-dipole R z 1 0 0 0 0 0
// dipole source oriented along x at position (R,z)
calc total-far-field totalff_r5z75_px.dat
// FF used to find radiative decay rate

end-calculation

end

```


A.3 Example BEM Material Data File

Ag.eps

63 E(eV) n

0.64	0.24	14.08
0.77	0.15	11.85
0.89	0.13	10.1
1.02	0.09	8.828
1.14	0.04	7.795
1.26	0.04	6.992
1.39	0.04	6.312
1.51	0.04	5.727
1.64	0.03	5.242
1.76	0.04	4.838
1.88	0.05	4.483
2.01	0.06	4.152
2.13	0.05	3.858
2.26	0.06	3.586
2.38	0.05	3.324
2.5	0.05	3.093
2.63	0.05	2.869
2.75	0.04	2.657
2.88	0.04	2.462
3	0.05	2.275
3.12	0.05	2.07
3.25	0.05	1.864
3.37	0.07	1.657
3.5	0.1	1.419
3.62	0.14	1.142
3.74	0.17	0.829
3.87	0.81	0.392
3.99	1.13	0.616
4.12	1.34	0.964
4.24	1.39	1.161
4.36	1.41	1.264
4.49	1.41	1.331
4.61	1.38	1.372
4.74	1.35	1.387
4.86	1.33	1.393
4.98	1.31	1.389
5.11	1.3	1.378
5.23	1.28	1.367

5.36	1.28	1.357
5.48	1.26	1.344
5.6	1.25	1.342
5.73	1.22	1.336
5.85	1.2	1.325
5.98	1.18	1.312
6.1	1.15	1.296
6.22	1.14	1.277
6.35	1.12	1.255
6.47	1.1	1.232
6.6	1.07	1.212
7.0	0.953	1.01
7.2	0.942	0.951
7.4	0.936	0.892
7.6	0.935	0.832
7.8	0.940	0.770
8.0	0.962	0.706
8.2	0.993	0.653
8.4	1.032	0.610
8.6	1.073	0.581
8.8	1.112	0.563
9.0	1.149	0.552
9.2	1.182	0.550
9.7	1.229	0.566
10.0	1.241	0.568

w(eV) n k

First line specifies: number of points (63),
 energy E(eV) or wavelength l(nm),
 and n & k (n) or eps1 & eps2 (e)

Ag dielectric function from Johnson and Christy (1972)
 0.64 eV < w < 6.6 eV ->
 187.9 nm < lambda < 1937 nm

Appendix B

Optical Characterization in the Nanoprobe

The Nanoprobe system (Omicron NanoTechnology, GmbH) integrates electron, electrical, surface, chemical, and optical characterization into a single instrument operating in ultra-high vacuum (UHV) conditions. This enables simultaneous investigation of electrical transport, chemical composition, and light-emission properties in a single nanostructure. The system at Caltech is equipped with a Zeiss Gemini SEM column, a NanoSAM Auger analyzer, and four independent scanning probes, two of which are capable of mounting optical fibers for light excitation and collection as well. A photograph of the typical nanoprobe stage is shown in Figure B.1a, and an SEM image of two etched W probes contacting a Si nanowire in Figure B.1b.

At Caltech, we have integrated detection optics to enable optical characterization inside the nanoprobe. In particular, optical fibers permit laser light to be coupled into the UHV chamber for excitation in photoconductivity measurements, or for emitted light from cathodoluminescence or electroluminescence experiments to be collected and sent to an exterior monochromator, PMT, and CCD detector similar to the CL setup of Chapters 2 and 3. Traditional CL configurations use a mirror to collect the emitted light that, if properly designed, collects a cone of $\pm 80^\circ$ from the surface normal. Inside the nanoprobe chamber, there is not sufficient space for a mirror-based detection system, and for this reason we chose to integrate fiber-based collection. Coupling multimode optical fibers with 50 μm (for excitation) and 200 μm (for collection) cores to two of the piezo-driven probes allows precise positioning in lateral dimensions and in height from the sample surface.

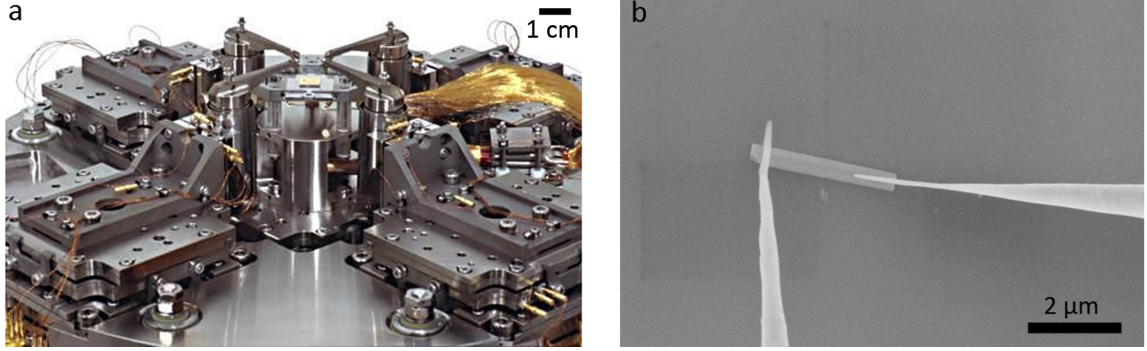


Figure B.1. (a) Photograph of the stage in the Omicron Nanoprobe system (image courtesy Omicron, GmbH). (b) SEM micrograph of two etched W probes in electrical contact with a Si nanowire.

We used a sample of Ce-doped YAG (YAG:Ce) particles on an In foil to calibrate the fiber-based collection as seen in Figure B.2. This material is known to exhibit extremely bright cathodoluminescence. The position of the fiber was optimized to obtain maximum CL emission intensity. Figure B.2a shows the optimal in-plane position of the fiber with respect to the electron beam position (center of the SEM micrograph). Here, we use the 200 μm core fiber for collection. The CL spectra and images in Figures B.2b and B.2c show that, indeed, bright CL is observed and that the YAG:Ce particles are the source of this emission. Furthermore, these CL spectra match those obtained from mirror-based CL that were taken for comparison.

Adding this capability to the nanoprobe system enables a number of novel experiments to be performed. Not only can the electron beam from the SEM be used to induce light emission, but when the probes operate as scanning tunneling microscopes (STM), one can pursue the investigation of STM-induced light emission in metallic nanostructures. This provides even higher spatial resolution than the focused electron beam in an SEM. The nanoprobe allows precise positioning of the STM probes over a specific nanostructure for extremely localized excitation. Additionally, a variety of optical fibers could be coupled to the scanning probes, such as tapered or lensed fibers for near-field collection or excitation. Such schemes that decouple regions of excitation and collection are valuable for determining the mechanisms of light emission.

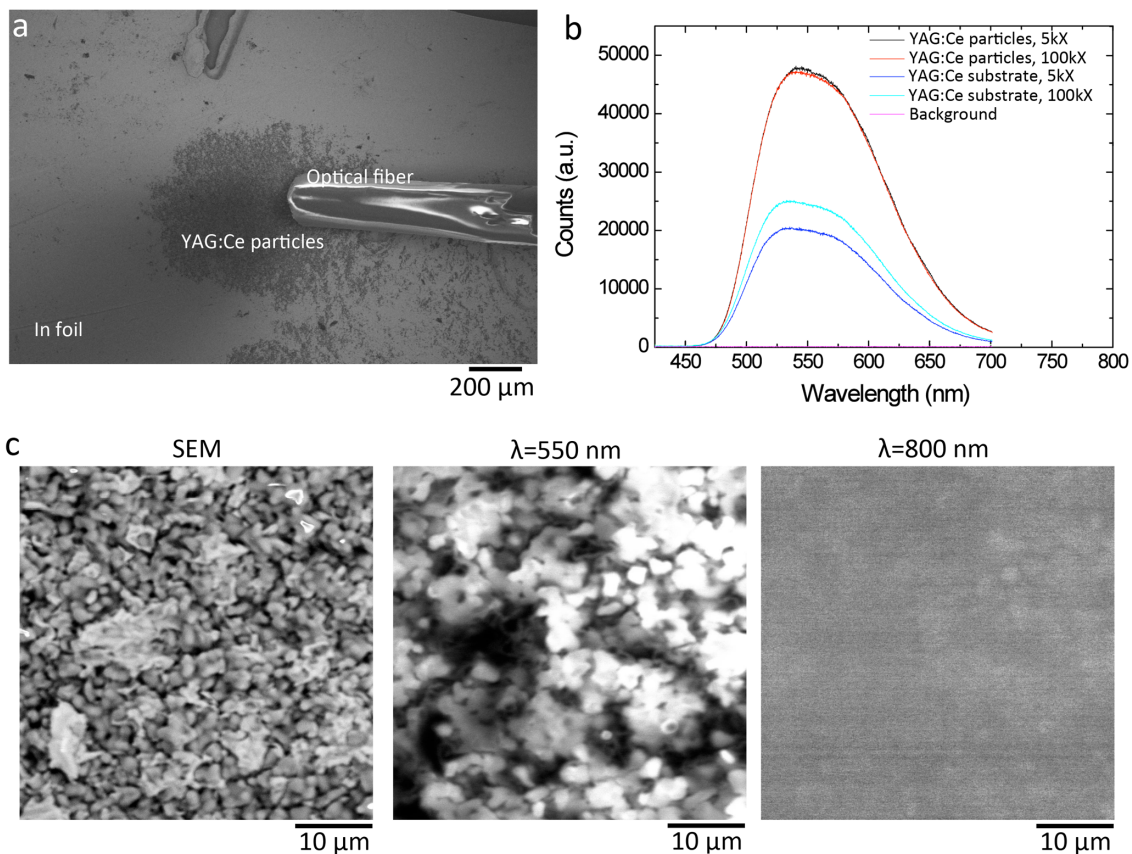


Figure B.2. (a) SEM micrograph of fiber-based CL collection in the nanoprobe. (b) CL spectra of YAG:Ce particles on an In foil and of a YAG:Ce substrate at low magnification (5 kX) and high magnification (100 kX). (c) SEM and monochromatic CL images of YAG:Ce particles. The CL image at $\lambda = 550 \text{ nm}$ shows that the particles emit at this wavelength, and not at $\lambda = 800 \text{ nm}$.

Bibliography

- [1] H. A. Bethe. Theory of diffraction by small holes. *Phys. Rev.*, 66:163–182, 1944. 1
- [2] U. Leonhardt. Optical metamaterials: Invisibility cup. *Nat. Phot.*, 1:207–208, 2007. 2
- [3] H. Raether. *Surface Plasmons on Smooth and Rough Surfaces and on Gratings*. Springer, Berlin, 1988. 2, 23, 32
- [4] K. L. Kelly, E. Coronado, L. L. Zhao, and G. C. Schatz. The optical properties of metal nanoparticles: The influence of size, shape, and dielectric environment. *J. Phys. Chem. B*, 107:668–677, 2003. 3
- [5] K. Kneipp, Y. Wang, H. Kneipp, L. T. Perelman, I. Itzkan, R. Dasari, and M. S. Feld. Single molecule detection using surface-enhanced Raman scattering (SERS). *Phys. Rev. Lett.*, 78:1667–1670, 1997. 3
- [6] A. Otto, I. Mrozek, H. Grabhorn, and W. J. Akemann. Surface-enhanced Raman scattering. *J. Phys.: Cond. Matter*, 4:1143–1212, 1992. 3, 32
- [7] K. A. Willets and R. P. Van Duyne. Localized surface plasmon resonance spectroscopy and sensing. *Ann. Rev. Phys. Chem.*, 58:267–297, 2007. 3
- [8] D. P. O’Neal, L. R. Hirsch, N. J. Halas, J. D. Payne, and J. L. West. Photothermal tumor ablation in mice using near infrared-absorbing nanoparticles. *Cancer Lett.*, 209:171–176, 2004. 3

- [9] H. A. Atwater and A. Polman. Plasmonics for improved photovoltaic devices. *Nat. Mater.*, 9:205–213, 2010. 3
- [10] S. A. Maier. *Plasmonics: Fundamentals and Applications*. Springer, New York, 2007. 4, 9
- [11] J. A. Dionne, L. A. Sweatlock, H. A. Atwater, and A. Polman. Planar metal plasmon waveguides: Frequency-dependent dispersion, propagation, localization, and loss beyond the free electron model. *Phys. Rev. B*, 72:075405, 2005. 8, 16, 19, 34, 40
- [12] J. A. Dionne, L. A. Sweatlock, H. A. Atwater, and A. Polman. Plasmon slot waveguides: Towards chip-scale propagation with subwavelength-scale localization. *Phys. Rev. B*, 73:035407, 2006. 8
- [13] H. T. Miyazaki and Y. Kurokawa. Squeezing visible light waves into a 3-nm-thick and 55-nm-long plasmon cavity. *Phys. Rev. Lett.*, 96:097401, 2006. 8, 51
- [14] A. Otto. Excitation of nonradiative surface plasma waves in silver by method of frustrated total reflection. *Z. Physik*, 216:398–410, 1968. 11
- [15] E. Kretschmann and H. Raether. Radiative decay of non-radiative surface plasmons excited by light. *Z. Naturforschung, A* 23:2135, 1968. 11
- [16] B. Hecht, H. Bielefeldt, L. Novotny, Y. Inouye, and D. W. Pohl. Local excitation, scattering, and interference of surface plasmons. *Phys. Rev. Lett*, 77:1889–1892, 1996. 11
- [17] F. J. García de Abajo. Optical excitations in electron microscopy. *Rev. Mod. Phys.*, 82:209–275, 2010. 11
- [18] D. Heitmann. Radiative decay of surface plasmons excited by fast electrons on periodically modulated silver surfaces. *J. Phys. C*, 10:397–405, 1977. 14

- [19] N. Yamamoto, K. Araya, and H. Sugiyama. Light emission from surfaces, thin films, and particles by high-energy electron beam. *Surf. Interface Anal.*, 31: 79–86, 2001. 14
- [20] R. Vincent and J. Silcox. Dispersion of radiative surface plasmons in aluminum films by electron scattering. *Phys. Rev. Lett*, 31:1487–1490, 1973. 15
- [21] R. B. Pettit, J. Silcox, and R. Vincent. Measurement of surface-plasmon dispersion in oxidized aluminum films. *Phys. Rev. B*, 11:3116–3123, 1975. 15
- [22] P. E. Batson. Damping of bulk plasmons in small aluminum spheres. *Solid State Commun.*, 34:477–480, 1980. 15
- [23] J. Nelayah, M. Kociak, O. Stephan, F. J. Garcia de Abajo, M. Tence, L. Henrard, D. Taverna, I. Pastoriza-Santos, L. M. Liz-Marzan, and C. Colliex. Mapping surface plasmons on a single metallic nanoparticle. *Nat. Phys.*, 3:348–353, 2007. 15, 33
- [24] W. J. Sigle, J. Nelayah, C. T. Koch, and P. A. van Aken. Electron energy losses in Ag nanoholes from localized surface plasmon resonances to rings of fire. *Opt. Lett.*, 34:2150–2152, 2009. 15
- [25] B. G. Yacobi and D. B. Holt. Cathodoluminescence scanning electron-microscopy of semiconductors. *J. Appl. Phys.*, 59:R1–R24, 1986. 15
- [26] S. A. Galloway, P. Miller, P. Thomas, and R. Harmon. Advances in cathodoluminescence characterisation of compound semiconductors with spectrum imaging. *Phys. Status Solidi C*, 0:1028–1032, 2003. 15, 24, 32, 34
- [27] N. Yamamoto, K. Araya, and F. J. Garcia de Abajo. Photon emission from silver particles induced by a high-energy electron beam. *Phys. Rev. B*, 64:205419, 2001. 15, 33
- [28] A. Degiron, H. J. Lezec, N. Yamamoto, and T. W. Ebbesen. Optical transmission properties of a single subwavelength aperture in a real metal. *Opt. Commun.*, 239: 61–66, 2004. 15

- [29] E. J. R. Vesseur, R. de Waele, M. Kuttge, and A. Polman. Direct observation of plasmonic modes in Au nanowires using high-resolution cathodoluminescence spectroscopy. *Nano Lett.*, 7:2843–2846, 2007. 15, 33
- [30] C. E. Hofmann, E. J. R. Vesseur, L. A. Sweatlock, H. J. Lezec, F. J. García de Abajo, A. Polman, and H. A. Atwater. Plasmonic modes of annular nanoresonators imaged by spectrally resolved cathodoluminescence. *Nano Lett.*, 7:3612–3617, 2007. 15
- [31] E. J. R. Vesseur, F. J. García de Abajo, and A. Polman. Modal decomposition of surface-plasmon whispering gallery resonators. *Nano Lett.*, 9:3147–3150, 2009. 15
- [32] M. Kuttge, E. J. R. Vesseur, and A. Polman. Fabry-perot resonators for surface plasmon polaritons probed by cathodoluminescence. *Appl. Phys. Lett.*, 94:183104, 2009. 15
- [33] B. Lamprecht, J. R. Krenn, G. Schider, H. Ditlbacher, M. Salerno, N. Felidj, A. Leitner, F. R. Aussenegg, and J. C. Weeber. Surface plasmon propagation in microscale metal stripes. *Applied Physics Letters*, 79:51–53, 2001. 16
- [34] P. B. Johnson and R. W. Christy. Optical constants of the noble metals. *Phys. Rev. B*, 6:4370–4379, 1972. 19, 39, 90, 111
- [35] E. Palik, editor. *Handbook of Optical Constants of Solids*. Academic Press, New York, 1985. 19
- [36] E. Palik and G. Ghosh. *Handbook of Optical Constants of Solids*, volume II. Academic Press, New York, 1991. 19
- [37] J. J. Burke, G. I. Stegeman, and T. Tamir. Surface-polariton-like waves guided by thin, lossy metal films. *Phys. Rev. B*, 33:5186–5201, 1986. 23
- [38] A. Hoffmann, Z. Lenkefi, and Z. Szentirmay. Effect of roughness on surface plasmon scattering in gold films. *J. Phys.: Cond. Matter*, 10:5503–5513, 1998. 24

- [39] D. L. Mills. Attenuation of surface polaritons by surface roughness. *Phys. Rev. B*, 12:4036–4046, 1975. 24
- [40] P. D. Yang, H. Q. Yan, S. Mao, R. Russo, J. Johnson, R. Saykally, N. Morris, J. Pham, R. R. He, and H. J. Choi. Controlled growth of ZnO nanowires and their optical properties. *Adv. Funct. Mater.*, 12:323–331, 2002. 24
- [41] D. J. Sirbully, M. Law, H. Yan, and P. D. Yang. Semiconductor nanowires for subwavelength photonics integration. *J. Phys. Chem. B*, 109:15190–15213, 2005. 24
- [42] D. Drouin, A. R. Coutire, R. Gauvin, P. Hovington, P. Horny, and H. Demers. *Monte Carlo Simulation of Electron Trajectory in Solids (Casino), Version 2.42*. Universite de Sherbrooke, Sherbrooke, Quebec, Canada, 2001. 26, 30, 34, 35
- [43] W. L. Barnes, A. Dereux, and T. W. Ebbesen. Surface plasmon subwavelength optics. *Nature*, 424:824–830, 2003. 32
- [44] D. J. Bergman and M. I. Stockman. Surface plasmon amplification by stimulated emission of radiation: Quantum generation of coherent surface plasmons in nanosystems. *Phys. Rev. Lett.*, 90:027402, 2003. 32
- [45] S. I. Bozhevolnyi, V. S. Volkov, E. Devaux, J.-Y. Laluet, and T. W. Ebbesen. Channel plasmon subwavelength waveguide components including interferometers and ring resonators. *Nature*, 440:508–511, 2006. 32
- [46] H. J. Lezec, A. Degiron, E. Devaux, R. A. Linke, L. Martin-Moreno, F. J. Garcia-Vidal, and T. W. Ebbesen. Beaming light from a subwavelength aperture. *Science*, 297:820–822, 2002. 32
- [47] F. Lopez-Tejeira, S. G. Rodrigo, L. Martin-Moreno, F. J. Garcia-Vidal, E. Devaux, T. W. Ebbesen, J. R. Krenn, I. P. Radko, S. I. Bozhevolnyi, M. U. Gonzalez, J. C. Weeber, and A. Dereux. Efficient unidirectional nanoslit couplers for surface plasmons. *Nat. Phys.*, 3:324–328, 2007. 32

- [48] Z. Liu, J. M. Steele, W. Srituravanich, Y. Pikus, C. Sun, and X. Zhang. Focusing surface plasmons with a plasmonic lens. *Nano Lett.*, 5:1726–1729, 2005. 32
- [49] J. M. Steele, Z. Liu, Y. Wang, and X. Zhang. Resonant and non-resonant generation and focusing of surface plasmons with circular gratings. *Opt. Express*, 14:5664–5670, 2006. 32
- [50] C.-K. Chang, D.-Z. Lin, C.-S. Yeh, C.-K. Lee, Y.-C. Chang, M.-W. Lin, J.-T. Yeh, and J.-M. Liu. Experimental analysis of surface plasmon behavior in metallic circular slits. *Appl. Phys. Lett.*, 90:061113, 2007. 32
- [51] J. Homola, S. S. Yee, and G. Gauglitz. Surface plasmon resonance sensors: review. *Sens. Actuators B*, 54:3–15, 1999. 32
- [52] S. Nie and S. R. Emory. Probing single molecules and single nanoparticles by surface-enhanced Raman scattering. *Science*, 275:1102–1106, 1997. 32
- [53] N. Yamamoto, M. Nakano, and T. Suzuki. Light emission by surface plasmons on nanostructures of metal surfaces induced by high-energy electron beams. *Surf. Interface Anal.*, 38:1725–1730, 2006. 33
- [54] M. Bosman, V. J. Keast, M. Watanabe, A. I. Maarroof, and M. B. Cortie. Mapping surface plasmons at the nanometre scale with an electron beam. *Nanotechnology*, 18:165505, 2007. 33
- [55] J. T. van Wijngaarden, E. Verhagen, A. Polman, C. E. Ross, H. J. Lezec, and H. A. Atwater. Direct imaging of propagation and damping of near-resonance surface plasmon polaritons using cathodoluminescence spectroscopy. *Appl. Phys. Lett.*, 88:22111, 2006. 33
- [56] M. V. Bashevoy, F. Jonsson, A. V. Krasavin, N. I. Kheludev, Y. Chen, and M. I. Stockman. Generation of traveling surface plasmon waves by free-electron impact. *Nano Lett.*, 6:1113–1115, 2006. 33

- [57] E. A. Taft and H. R. Phillip. Optical constants of silver. *Phys. Rev.*, 121:1100, 1961. 35
- [58] G. Fuster, J. M. Tyler, N. E. Brener, and J. Calloway. Electronic structure and related properties of silver. *Phys. Rev. B*, 42:7322–7328, 1990. 35
- [59] *Maxwell’s Equations by Finite Integration Algorithm (MaFIA)*, 4th ed. Gesellschaft für Computer-Simulationstechnik (CST), Darmstadt, Germany, 2000. 36
- [60] L. A. Sweatlock, S. A. Maier, H. A. Atwater, J. J. Penninkhof, and A. Polman. Highly confined electromagnetic fields in arrays of strongly coupled Ag nanoparticles. *Phys. Rev. B*, 71:235408, 2005. 37
- [61] F. J. García de Abajo and A. Howie. Relativistic electron energy loss and electron-induced photon emission in inhomogeneous dielectrics. *Phys. Rev. Lett.*, 80:5180–5183, 1998. 39
- [62] F. J. García de Abajo and A. Howie. Retarded field calculation of electron energy loss in inhomogeneous dielectrics. *Phys. Rev. B*, 65:115418, 2002. 39, 89
- [63] B. E. A. Saleh and M. C. Teich. *Fundamentals of Photonics*. John Wiley and Sons, Hoboken, NJ, 2007. 40, 63
- [64] T. J. Kippenberg, S. M. Spillane, and K. J. Vahala. Demonstration of ultra-high-Q small mode volume toroid microcavities on a chip. *Appl. Phys. Lett.*, 85: 6113, 2004. 50
- [65] M. O. Scully and M. S. Zubairy. *Quantum Optics*. Cambridge University Press, Cambridge, United Kingdom, 2002. 65
- [66] Y. C. Jun, R. D. Kekatpure, J. S. White, and M. L. Brongersma. Nonresonant enhancement of spontaneous emission in metal-dielectric-metal plasmon waveguide structures. *Phys. Rev. B*, 78:153111, 2008. 65
- [67] J. J. Greffet. Nanoantennas for light emission. *Science*, 308:1561–1563, 2005. 65

- [68] K. J. Vahala. Optical microcavities. *Nature*, 424:839–846, 2003. 65
- [69] E. M. Purcell. Spontaneous emission probabilities at radio frequencies. *Phys. Rev.*, 69:681, 1946. 65, 88
- [70] A. D. McFarland and R. P. Van Duyne. Single silver nanoparticles as real-time optical sensors with zeptomole sensitivity. *Nano Lett.*, 3:1057–1062, 2003. 69
- [71] S. Underwood and P. Mulvaney. Effect of the solution refractive-index on the color of gold colloids. *Langmuir*, 10:3427–3430, 1994. 69
- [72] F. Tam, C. Moran, and N. Halas. Geometrical parameters controlling sensitivity of nanoshell plasmon resonances to changes in dielectric environment. *J. Phys. Chem. B*, 108:17290–17294, 2004. 69
- [73] C. L. Nehl, H. W. Liao, and J. H. Hafner. Optical properties of star-shaped gold nanoparticles. *Nano Lett.*, 6:683–688, 2006. 69
- [74] R. S. Wagner and W. C. Ellis. Vapor-liquid-solid mechanism of single crystal growth. *Appl. Phys. Lett.*, 4:89–90, 1964. 72
- [75] B. M. Kayes, M. A. Filler, M. C. Putnam, M. D. Kelzenberg, N. S. Lewis, and H. A. Atwater. Growth of vertically aligned Si wire arrays over large areas ($> 1 \text{ cm}^2$) with Au and Cu catalysts. *Appl. Phys. Lett.*, 91:103110, 2007. 72
- [76] M. D. Henry, S. Walavalkar, A. Homyk, and A. Scherer. Alumina etch masks for fabrication of high-aspect-ratio silicon micropillars and nanopillars. *Nanotechnology*, 20:255305, 2009. 77
- [77] K. H. Drexhage. Interaction of light with monomolecular dye layers. *Prog. Optics*, 12:163, 1974. 88
- [78] J. I. Gersten and A. Nitzan. Photophysics and photochemistry near surfaces and small particles. *Surf. Sci.*, 158:165, 1985. 88
- [79] J. Vuckovic, M. Loncar, and A. Scherer. Surface plasmon light-emitting diode. *IEEE J. Quantum Electron.*, 36:1131, 2000. 88

- [80] K. Okamoto, I. Niki, A. Shvarster, Y. Narukawa, T. Mukai, and A. Scherer. Surface-plasmon enhanced light emitters based on InGaN quantum wells. *Nat. Mat.*, 3:601, 2004. 88
- [81] F. Tam, G. P. Goodrich, B. R. Johnson, and N. J. Halas. Plasmonic enhancement of molecular fluorescence. *Nano Lett.*, 7:496, 2007. 88
- [82] S. Kuhn, U. Halanson, L. Rogobete, and V. Sandoghdar. Enhancement of single-molecule fluorescence using a gold nanoparticle as an optical nanoantenna. *Phys. Rev. Lett.*, 97:017402, 2006. 88
- [83] M. A. Noginov, G. Zhu, A. M. Belgrave, R. Bakker, V. M. Shalaev, E. E. Narimanov, S. Stout, E. Herz, T. Suteewong, and U. Wiesner. Demonstration of a spaser-based nanolaser. *Nature*, 460:1110, 2009. 88
- [84] R. F. Oulton, V. J. Sorger, T. Zentgraf, R.-M. Ma, C. Gladden, L. Dai, G. Bartal, and X. Zhang. Plasmon lasers at deep subwavelength scale. *Nature*, 461:629, 2009. 88
- [85] L. A. Blanco and F. J. García de Abajo. Spontaneous light emission in complex nanostructures. *Phys. Rev. B*, 69:205414, 2004. 89, 110
- [86] D. E. Aspnes and A. A. Studna. Dielectric functions and optical parameters of Si, Ge, GaP, GaAs, GaSb, InP, InAs, and InSb from 1.5 to 6.0 eV. *Phys. Rev. B*, 27:985, 1983. 90
- [87] M. M. Y. Leung, A. B. Djuricic, and E. H. Lia. Refractive index of InGaN/GaN quantum well. *J. Appl. Phys.*, 84:6312, 1998. 90
- [88] C. Tanguy. Optical dispersion by Wannier excitons. *Phys. Rev. Lett.*, 75:4090, 1995. 90
- [89] C. Tanguy. Refractive index of direct bandgap semiconductors near the absorption threshold: Influence of excitonic effects. *IEEE J. Quantum Electron.*, 32:1746, 1996. 90

- [90] P. Anger, P. Bhadrwaj, and L. Novotny. Enhancement and quenching of single molecule fluorescence. *Phys. Rev. Lett.*, 96:113002, 2006. 91
- [91] A. Neogi, C.-W. Lee, H. O. Everitt, T. Kuroda, A. Tackeuchi, and E. Yablonovitch. Enhancement of spontaneous recombination rate in a quantum well by resonant surface plasmon coupling. *Phys. Rev. B*, 66:153305, 2002. 98
- [92] C. Colombo, M. Heiss, M. Graetzel, and A. Fontcuberta i Morral. Gallium arsenide p-i-n radial structures for photovoltaic applications. *Appl. Phys. Lett.*, 94:173108, 2009. 106